Fabry-Perot interferometer based on end-of-fiber polymer microtip for chemical sensing

Thi Nhung Pham

THÈSE PRÉSENTÉE

POUR OBTENIR LE GRADE DE

DOCTEUR DE

L'UNIVERSITÉ DE BORDEAUX

ÉCOLE DOCTORALE DES SCIENCES PHYSIQUES ET DE L'INGENIEUR

SPÉCIALITÉ: ELECTRONIQUE

Par **Thi-Nhung PHAM**

Fabry-Perot interferometer based on end-of-fiber polymer microtip for chemical sensing

Sous la direction de: Dr. Cédric AYELA

Soutenue le 15/01/2024

Membres du jury:

M. FAVERO, Ivan	Directeur de recherche, Université Paris Cité, MPQ, UMR 7162	Président du Jury
M. SOPPERA, Olivier	Directeur de recherche, Université de Haute-Alsace, IS2M, UMR 7361	Rapporteur
M. AGACHE, Vincent	Directeur de recherche, Université Grenoble Alpes, CEA, LETI	Rapporteur
Mme. DUFOUR, Isabelle	Professeur, Université de Bordeaux, IMS, UMR 5218	Examinatrice
M. HAUPT, Karsten	Professeur, Université de Technologie de Compiègne, GEC, UMR 7025	Examinateur
M. LAI, Ngoc-Diep	Maître de conferences, ENS Paris-Saclay, LuMIn, UMR 9024	Examinateur
M. AYELA, Cédric	Chargé de recherche, Université de Bordeaux, IMS, UMR 5218	Directeur de thèse

Membres invités:

M. GUERRAULT, Sébastien	Ingénieur, SensWay	Invité

Interféromètre Fabry-Perot basé sur des pointes polymères microstructurées en bout de fibre optique pour la détection chimique

Résumé

Les interféromètres Fabry-Perot (FPI) ont reçu un grand intérêt pour leur utilisation en tant que capteurs. Les FPI sont constitués d'une cavité optique avec des surfaces parallèles qui réfléchissent la lumière incidente, produisant un signal interférométrique optique. Ce signal dépend de la distance entre les surfaces réfléchissantes et de l'indice de réfraction de la cavité, qui sont sensibles aux variations d'humidité, de température, de pression et du matériau. Les FPI peuvent être attachés à des fibres optiques, qui fonctionnent comme un guide d'ondes pour le signal incident et le signal réfléchi, et former ainsi des capteurs compacts. Cette thèse présente des capteurs chimiques à base de FPI incorporant une micropointe en polymère structurée à l'extrémité d'une fibre optique, étudiés pour la détection d'humidité, d'eau et de cibles chimiques.

Tout d'abord, nous développons une pointe de poly triacrylate de pentaérythritol (p(PETA)) sur la facette d'une fibre optique par photopolymérisation autoguidée. Une extrémité de la fibre est placée dans une goutte de PETA et la photopolymérisation est activée par un laser de 375 nm injecté à l'autre extrémité de la fibre. Les conditions optimales pour former une pointe p(PETA) mécaniquement stable sont 1µW de puissance laser × 1s de temps d'exposition. Cependant, les chaînes PETA ne sont pas complètement polymérisées lors de cette étape, ce qui entraîne une fréquence de résonance instable de la pointe. La pointe doit donc être post-polymérisée sous une lampe UV de 365nm pour obtenir une caractéristique dynamique stable, avant leur application en tant que capteur.

Deuxièmement, nous démontrons que la pointe p(PETA) est un capteur efficace pour détecter l'humidité. Elle fonctionne comme une cavité optique formée entre le cœur de la fibre/p(PETA) et l'interface p(PETA)/environnement, ce qui permet d'obtenir un signal interférométrique clair. Le signal FPI de la pointe est très sensible à l'humidité de l'air grâce aux groupes hydroxyles du PETA, qui absorbent les molécules d'eau dans l'air humide, induisant un gonflement de la pointe. La longueur et/ou l'indice de réfraction sont donc modifiés, ce qui entraîne une variation du signal interférométrique. La pointe présente une sensibilité constante de 90 pm/%RH, équivalent à une sensibilité relative de 104 ppm/%RH pour une plage d'humidité de 30 à 80 %. La détection est hautement reproductible et stable. En outre, l'effet de la température est négligeable, favorisant leur potentiel d'application.

Ensuite, nous appliquons les pointes p(PETA) basées sur le FPI pour déterminer la teneur en eau de solutions de glycérol et d'éthylène glycol. Le signal FPI de la pointe p(PETA) varie de manière non linéaire lorsque la teneur en eau passe de 0 à 100% en poids. La variation du signal FPI est due à la contraction de la pointe, qui est liée à la perte d'eau à l'intérieur de la structure PETA. Lorsque la contamination par l'eau est inférieure à 10%, la pointe présente une sensibilité linéaire de 394 pm/wt.% et 226 pm/wt.% pour les solutions de glycérol et d'éthylène glycol, respectivement. Ainsi, la pointe p(PETA) basée sur le FPI présente un grand potentiel pour la détermination de la teneur en eau de solutions aqueuses, y compris les hydrocarbures.

Enfin, une pointe constituée d'un cœur p(PETA) et d'une enveloppe de polymères à empreintes moléculaires (MIP) a été mise au point pour détecter la Dansyl-L-phénylalanine. La pointe p(PETA) est initialement fabriquée en utilisant la polymérisation autoguidée et les MIP sont ensuite copolymérisés pour former une fine couche d'enveloppe autour de la pointe p(PETA). Lors de la détection sélective de la Dansyl-L-phénylalanine, l'indice de réfraction de la couche de MIP change, ce qui entraîne une modification du signal FPI de l'ensemble de la pointe p(PETA)/MIP. Cette méthode simple offre de nouvelles possibilités pour créer des capteurs à fibre optique MIP à base de FPI applicables à une large gamme d'analytes, qu'ils soient fluorescents ou non.

Mots-clés : Interféromètre Fabry-Perot, capteur fibré, point polymère, hygroscopie, polymère à empreinte moléculaire

Fabry-Perot interferometer based on end-of-fiber polymer microtip for chemical sensing

Abstract

Fabry−Perot interferometers (FPIs) have received a significant attention for their use in sensor applications. FPIs consist of an optical cavity with separate parallel reflecting surfaces which reflect incident light, resulting in an optical interferometric signal. The FPI signal depends on the distance between the reflecting surfaces and the refractive index of the cavity medium, which are sensitive to variation of environment humidity, temperature, pressure, and material. FPIs can be attached to optical fibers to form compact fiber optic FPI-based sensors in which the optical fiber works as a waveguide for both incident and reflected signal. This thesis presents FPI-based chemical sensors incorporating a polymer microtip located at the end of an optical fiber and characterizes their sensing capabilities for humidity, water, and chemical targets.

Firstly, we develop a poly pentaerythritol triacrylate (p(PETA)) tip on the facet of an optical fiber by a self-guiding photopolymerization. One end of the optical fiber is placed inside a PETA droplet and the self-guiding photopolymerization of PETA is actuated by a 375 nm laser injected to the other end of the fiber. The optimal conditions to form a straight and mechanically stable p(PETA) tip are 1.0 μW of laser power × 1.0 second of exposure time. However, the PETA chains do not completely polymerize during this self-polymerization, leading to an unstable dynamic resonant frequency of the tip. Thus, the tip needs a post-polymerization under a UV 365 nm lamp to achieve a stable dynamic characteristic, which is applicable for further sensing applications.

Secondly, we demonstrate the p(PETA) tip as an effective sensor to detect humidity. The PETA tip acts as an optical cavity formed between the fiber-core/p(PETA) and the

p(PETA)/environment interface, resulting in a clear interferometric signal. The FPI signal of the tip is highly sensitive to humidity in the air. This is due to hydroxyl groups within the PETA structure, which strongly absorb water molecules in the humid air and significantly swell the tip. The length and/or the refractive index of the tip are therefore changed, resulting in a FPI shift. The tip exhibits a consistent sensitivity of 90pm/%RH, equivalent to a relative sensitivity of 104 ppm/%RH in the humidity range from 30 to 80%. The sensing performance is highly reproducible and stable. Furthermore, the cross effect of the temperature is negligible, indicating a great practical potential for the devices.

Next, we apply the FPI-based p(PETA) tips to determine the water content in glycerol and ethylene glycol solutions. The FPI signal of the p(PETA) tip shifts nonlinearly towards longer wavelengths as the water content increases from 0 to 100 wt.%. The shift in the FPI signal occurs due to the contraction in the tip length, which is linked to the loss of water inside the PETA structure caused by the hygroscopic solutions. When the water contamination is below 10 wt.%, the tip shows a linear sensitivity of 394 pm/wt.% and 226 pm/wt.% for glycerol and ethylene glycol solutions, respectively. Therefore, the FPI-based p(PETA) tip shows a great potential in determining water content in hydrophilic aqueous solutions, including hydrocarbons.

Finally, a tip consisting of a p(PETA) core and a shell of molecularly imprinted polymers (MIPs) is developed for detecting Dansyl-L-phenylalanine. The p(PETA) tip is initially fabricated using the self-guiding polymerization and MIPs are then copolymerized to form a thin shell layer around the p(PETA) tip. Upon the selective binding of Dansyl-L-phenylalanine, the refractive index of the MIP layer changes, leading to the change in the FPI signal of the whole p(PETA)/MIP tip. This straightforward and affordable method offers new innovative possibilities for creating FPI-based MIP fiber optic sensors, which can be applied for a wide range of analytes, including both non-fluorescent and fluorescent targets.

Keywords: Fabry-Perot interferometer, optical fiber sensor, polymer tip, water content, molecularly imprinted polymer

La thèse a été préparée dans le Laboratoire de l'Intégration du Matériau au Système – UMR 5218

16 Avenue Pey Berland

33600 Pessac

Acknowledgement

These past three years have been both challenging and memorable for me. I would like to express my sincere gratitude to those who have supported and helped me throughout this period.

Firstly, I am extremely grateful to Dr. Cédric Ayela for being my great supervisor. I really appreciate his scientific guidance, continuous support and encouragement throughout my PhD study. I am thankful not only for his insightful comments and suggestion, but also for his kind words after each meeting, which helped me to figure out difficulties.

I would like to express my deep appreciation to the jury members: Dr. Olivier Soppera, Dr. Vincent Agache, Prof. Isabelle Dufour, Prof. Karsten Haupt, Dr. Ivan Favero and Assoc. Prof. Ngoc Diep Lai. Thank you for spending time and effort to provide valuable feedback on my manuscript and evaluate my work.

I would like to express my gratitude to Prof. Karsten Haupt for kindly hosting me at Université de Technologie de Compiègne (UTC) – GEC for two weeks. I will always remember his warm hospitability and immense knowledge. I am deeply grateful for his continuous support and prompt responsiveness to my questions and emails, which significantly aided me in resolving my issues related to MIP-based sensors. I also would like to express my special thanks to Dr. Ernesto Paruli at UTC for his thoughtful guidance in the fabrication a core of PETA and a shell of MIP for the chemical sensing.

I am also thankful to Dr. Laurent Bouffier and Dr. Bertrand Goudeau at Institut des Sciences Moléculaires of Bordeaux (ISM/NSYSA) for training me and allowing me to use the fluorescence microscope.

I specially thank Sébastien Guerrault for being an invited member in my thesis defense and for helping me to build FPI measurement setup during the initial stages of my PhD study.

I had the pleasure of working with the members of the Organic team at IMS: Prof. Isabelle Dufour, Assoc.Prof. Damien Thuau, Assoc. Prof. Hélène Debeda, Dr. Mamatimin Abbas, Dr. Lionel Hirsch, Dr. Sylvain Chambon, Dr. Marie Gueunier-Farret, Prof. Laurence

Vignau, Prof. Guillaume Wantz, Dr. Gilles Roche, Dr. Chloé Dindault, Dr. Zuzanna Molenda, Dr. Rumi Levi, Dr. Getnet Kassahun, Cindy Mauriac, Martial Leyney, Francis Feaugas, Ewen Raoul, Hugo Laval, Quan Sun, Reem El-Attar. I thank all of them for their kindness and support. I especially want to thank Gilles for helping me become familiar with the lab at the beginning of my journey, and Zuzanna for being a great "office-mate" – attentively listening and openly sharing.

I warmly thank my Vietnamese friends. Em cảm ơn anh Thanh, chị Minh, chị Ngân vì những lần gặp gỡ vui vẻ và những chia sẻ thân tình. Cảm ơn Oanh, Mai, Trần Đức, mặc dù ở xa nhưng vẫn luôn động viên mình. I also would like to thank my friends at Paul Pascal Research Center, Long Fei and Zi, for enjoyable and relaxing badminton matches at the weekends.

I would like to extend my sincere appreciation to Assoc. Prof. Ngoc Diep Lai for his kindness, constant support and valuable advice since the first day I arrived in France. Em luôn trân trọng và cảm ơn những sự giúp đỡ, chia sẻ tận tâm của thầy!

I must express my profound gratitude to my parents, sister, parents-in-law and younger brother-in-law for their unfailing support and continuous encouragement. Cảm ơn gia đình mình rất nhiều!

Last but not least, great love and special thanks to my dear husband. This endeavor would not have been possible without you. Nothing can express how hard you have worked to encourage me, to support me to overcome this toughest time in my life. I am reminded of a quote from Albus Dumbledore in the Harry Potter series: "Happiness can be found, even in the darkest of times, if one only remembers to turn on the light". And you are undoubtedly my guiding light. As the lyrics go, *"You raise me up, so I can stand on mountains*

You raise me up, to walk on stormy seas

I am strong, when I am on your shoulders

You raise me up to more than I can be…"

Cảm ơn tình yêu của cuộc đời em. Gửi đến anh thật nhiều yêu thương!

I dedicate this thesis to my beloved husband, Minh Thanh, and my forthcoming baby.

List of publications

1. T.N. Pham, S. Guerrault, and C. Ayela, “Polymer Microtip-Based Fabry–Perot Interferometer for Water Content Determination in the Gas and Liquid Phase”, ACS Applied Materials & Interfaces 2023 15 (39), 46368-46378 (Chapter 3 and 4).
2. T.N. Pham, E. Paruli, K. Haupt, and C. Ayela, “Selective detection of desired analyte by incorporating Fabry-Perot interferometer fiber optic sensor and molecularly imprinted polymer”, in preparation (Chapter 5).

Contents

Chapter 1

Introduction

Abstract. This chapter begins with an introductory description of the Fabry-Perot interferometer (FPI) which can be potentially used as sensor device. It then describes common designs of fiber optic based FPI sensors including extrinsic and intrinsic configurations. Next, possible applications of fiber optic based FPI sensors for detecting various physical and chemical parameters including temperature, strain, pressure, humidity, refractive index, and chemical targets are reviewed. Finally, the chapter closes with a description of the motivation and an outline of the thesis.

1.1. Fabry-Perot interferometer

A Fabry-Perot interferometer (FPI) is an optical device that consists of two parallel optical reflectors with reflection coefficients R_1 and R_2. These reflectors are separated by a cavity with the refractive index n, and the length L (as shown in Figure 1.1(a)). When an incident light with an electric field E_0 propagates through the FPI, a portion of the light is reflected at the first reflector, denoted as E_{r1}. The other part of the light propagates through the cavity and then reflects at the second reflector, denoted as E'_{r2}. The reflected light E'_{r2} propagates through the cavity. A portion of it transmits through the first reflector, denoted as E_{r2}. The E_{r2} interferes with the first reflected light E_{r1}. The remaining portion of E'_{r2} reflects at the first reflector and continues to propagate towards the second reflector. This process is repeated continuously, resulting in a multiple-beam interference signal of E_{r1}, E_{r2}, E_{r3},…, as demonstrated in Figure 1.1(a) [1]. If the reflectors have low reflection coefficients, for example in the case of two interfaces between media with a small refractive index mismatch, the reflected beams E_{r3}, E_{r4}, etc., are insignificant as compared to E_{r2} [1]. One can therefore ignore the multiple reflections and only consider a model of two-beam interference, as shown in Figure 1.1(b).

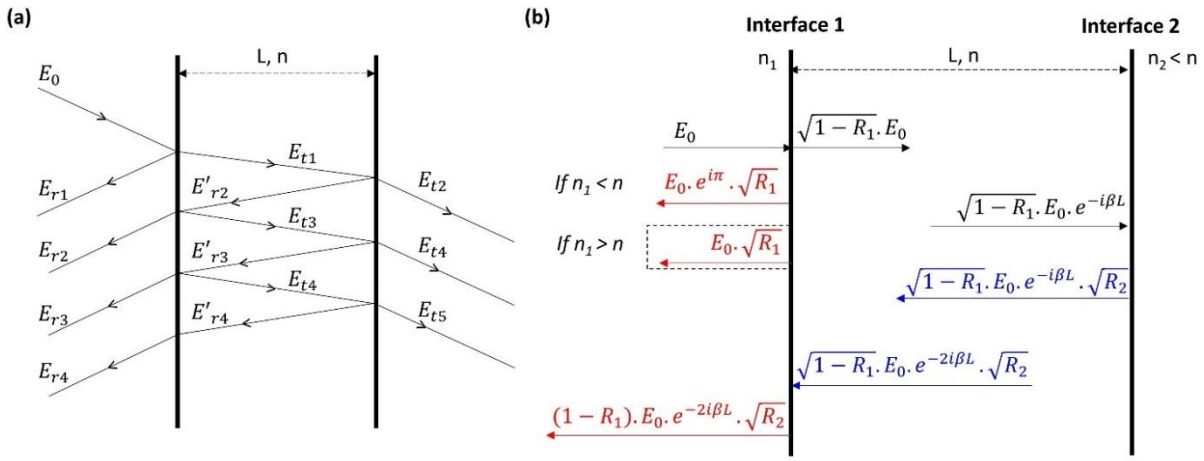

Figure 1. 1. (a) A general schematic demonstration of a Fabry-Perot cavity. (b) Electric field amplitudes of the incident, transmitted, and reflected light of two-beam interference FPI formed between two parallel interfaces.

We consider the simplest case when the incident light E_0 is perpendicular to the interfaces and the cavity between the interfaces is a lossless medium. The reflection coefficients at these two interfaces R_1 and R_2 can be determined as follows:

$$R_1 = \frac{(n_1 - n)^2}{(n_1 + n)^2} \tag{1.1}$$

$$R_2 = \frac{(n_2 - n)^2}{(n_2 + n)^2} \tag{1.2}$$

where n_1, n and n_2 are the refractive indices of the medium 1, the cavity and the medium 2, respectively. The first and second reflected electric field E_{r1}, E_{r2} [2]–[4] are determined as:

$$E_{r1} = \pm E_0.\sqrt{R_1} \tag{1.3}$$

$$E_{r2} = (1 - R_1).E_0.e^{-2i\beta L}.\sqrt{R_2} \tag{1.4}$$

where $\beta = \frac{2\pi n}{\lambda}$ is the propagation constant within the cavity. The expression (1.3) has the positive sign if $n_1 > n$ and the negative sign (-) if $n_1 < n$. These two beams interfere with each other and result in an interference signal as follows:

$$E_r = \pm E_0.\sqrt{R_1} + (1 - R_1).E_0.e^{-2i\beta L}.\sqrt{R_2} \tag{1.5}$$

The normalized intensity R_{FP} of the interferometric pattern is then determined as follows:

$$R_{FP} = \left|\frac{E_r}{E_0}\right|^2 = R_1 + (1-R_1)^2 \cdot R_2 \pm 2\sqrt{R_1 R_2}(1-R_1)\cos(\frac{4\pi nL}{\lambda}) \quad (1.6)$$

It is seen that the FPI signal depends on the phase difference ($\frac{4\pi nL}{\lambda}$) between the two reflected beams which is determined by the length and the refractive index of the cavity medium. These characteristics of the cavity may be sensitive to variations of environmental conditions such as humidity, temperature, pressure, and material structure. As a result, the interferometric signal of a FPI is also sensitive to the external environmental conditions, making the FPI applicable as sensor devices [1].

1.2. Configuration of fiber optic FPI-based sensor

FPIs are commonly attached to optical fibers to form compact fiber optic FPI-based sensors in which the optical fiber works as a waveguide for both incident and reflected signal. These sensors have a small size, exhibit high efficiency and electromagnetic immunity, which make them highly practical for detecting various physical, chemical and biological parameters. FPI-based fiber sensors can be classified into two main types: intrinsic and extrinsic (Figure 1.2). If the optical cavity is located inside the fiber, it is identified as an intrinsic FPI sensor. Alternatively, if the cavity is situated externally to the fiber, it is an extrinsic FPI sensor [1], [5].

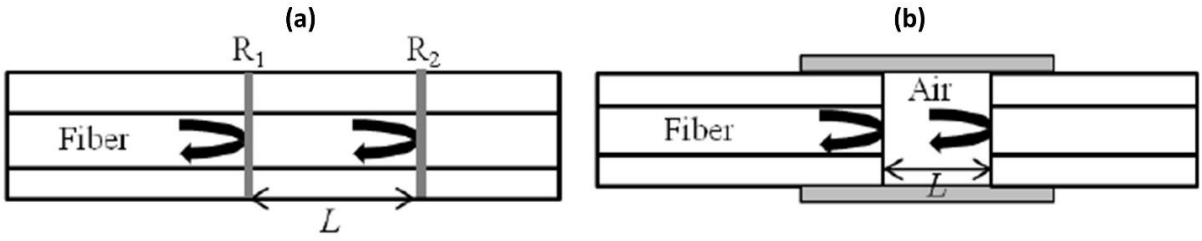

Figure 1. 2. (a) Schematic demonstration of an intrinsic FPI sensor formed by two reflecting components (R1 and R2) within an optical fiber. (b) Schematic demonstration of an extrinsic FPI sensor made by an air cavity located outside the optical fiber. This figure is adapted from Ref [5].

1.2.1. Intrinsic fiber optic FPI-based sensors

Many techniques for creating the local cavity of the intrinsic FPI sensor have been reported in the literature. One such method involves the splicing of different optical fibers with a core refractive-index mismatch [6], [7]. In this method, one fiber is considered as a cavity with the reflected surfaces being the interfaces between the two fibers. Another technique entails forming a micro-notch in a fiber by using femtosecond lasers [8]–[10] (Figure 1.3). In addition, chemical etching can also be used to create an air hole in the fiber before the splicing of the two etched fibers to create an intrinsic FPI sensor [11], [12]. While these sensors have been demonstrated to sensitively detect various parameters including temperature, refractive index and strain, they have drawbacks including the requirement for expensive equipment, specialized skills and dangerous chemical reagents.

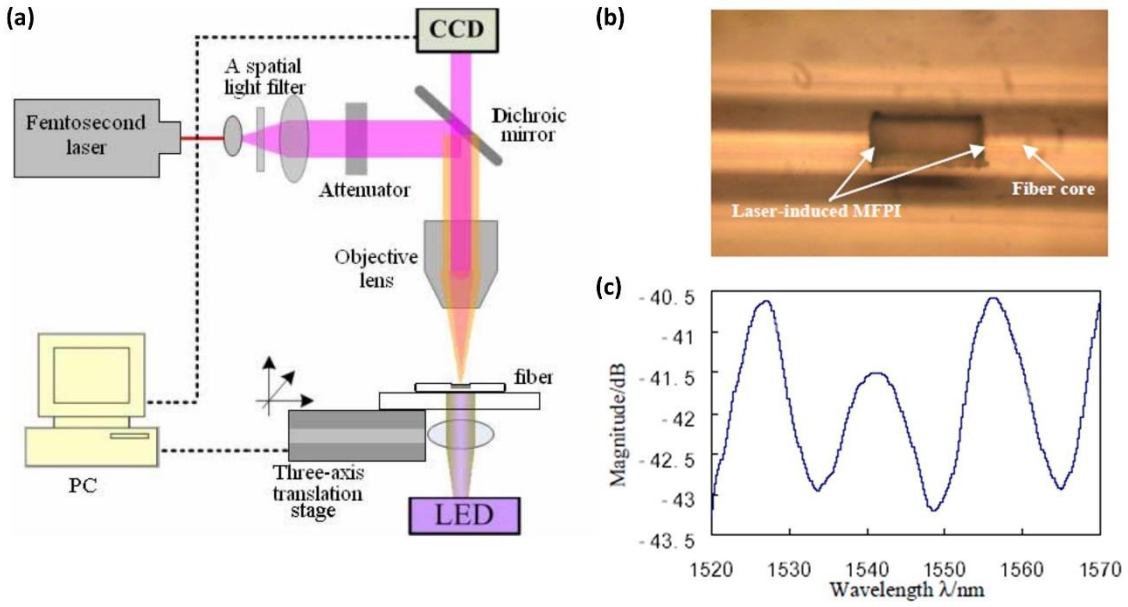

Figure 1. 3. (a) Schematic diagram of the femtosecond laser system to create a micro-notch in an optical fiber. (b) Optical photograph and (c) reflective spectrum of the FPI based on an 80-μm long micro notch in a single mode fiber. This figure is adapted from Ref [8].

1.2.2. Extrinsic fiber optic FPI-based sensors

An alternative to intrinsic FPI-based optical sensors are extrinsic FPI sensors, consisting of an air or polymer cavity formed externally of the fiber. For instance, Kim et al. [13] used a silica

capillary tube to bond two fibers that are separated by an air gap with epoxy. Meanwhile, Duan et al. [14] created an air cavity by splicing a short section of a SMF between two other sections of SMFs (referred to as input and reflection fibers) with a large lateral offset (Figure 1.4). The gap between the input fiber and reflection fiber forms an open cavity which allows gas or liquid to enter or exit easily, making it suitable for sensing the refractive index of the surrounding medium. Another approach involves the coating of a thin layer of an environmentally sensitive material, typically polymers, on the facet of an optical fiber [4], [15], [16]. This produced a FPI signal between the fiber-facet/polymer interface and the polymer/ambient interface. In this design, the thickness of the deposited polymer layer is controlled manually and roughly by either using different aliquot solutions [15], or adjusting the concentration of the precursor solutions [17], or by using fibers with different diameters [16]. Although the aforementioned extrinsic FPI devices have been identified as useful candidates for different applications such as temperature, humidity, and refractive index sensing, they exhibit lower coupling efficiency as compared to the intrinsic FPI sensors. Additionally, their fabrication requires expensive equipment and specialized skills for fiber splicing, and exhibit a limit of reproducibility due to hard-control of processing steps.

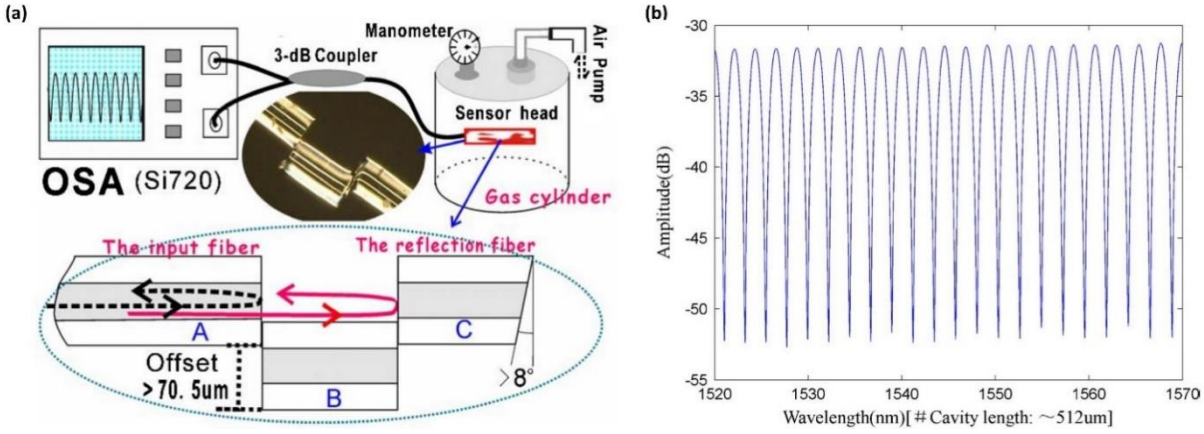

Figure 1. 4. (a) Schematic draw of the sensor system (top) and the detailed structure of the FPI sensor head (bottom) formed by splicing different optical fibers. (b) FPI signal of the sensor with a cavity geometry length of ~512 um. This figure is adapted from Ref [14].

An interesting, cost-effective, straightforward method to form extrinsic FPI is the self-guiding photo-polymerization process, which enables a polymer micro-tip to form at the end of an optical fiber [18], [19] (Figure 1.5). This method enables the rapid fabrication of a micro-

tip of well-defined and well controlled geometry at the micro-scale. The polymer tip itself forms an optical cavity that can function directly as a FPI with higher coupling efficiency as compared to the other extrinsic FPI sensors. Moreover, the cavity length can be freely changed as the environmental parameters change. The polymer tip at the end of the fiber is thus promising for practical sensing applications.

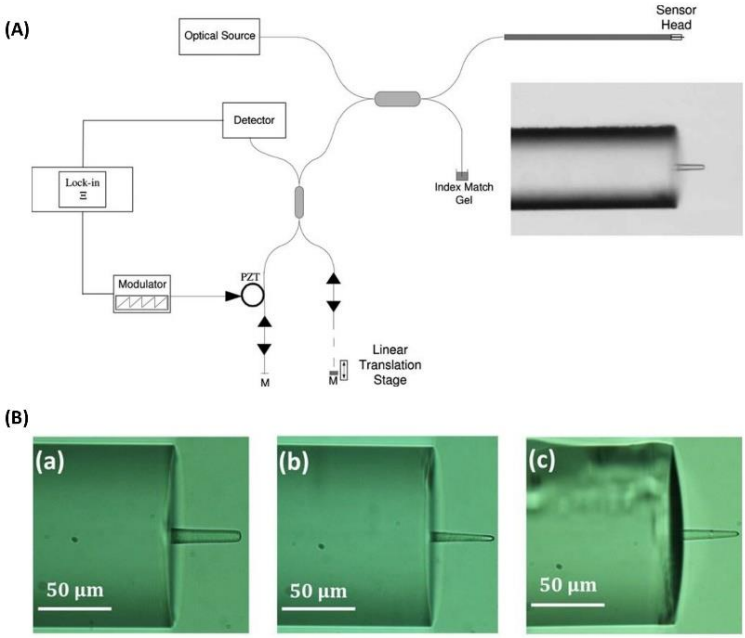

Figure 1. 5. (a) Experimental setup and photo of a FPI sensor based on a polymer tip at the end of an optical fiber for RI sensing, adapted from Ref [18]. (b) Different microtips at the end of optical fibers for humidity sensing, adapted from Ref [19].

1.3. Application of fiber optic FPI-based sensors for physical parameters

Most of the current research in fiber optic FPI sensing has focused on measuring physical parameters, such as temperature, strain and pressure.

1.3.1. Temperature measurement

Temperature detection is essential in both daily life and industrial applications. FPI-based temperature sensors typical consist of a cavity which incorporates materials with a high thermo-optic and/or thermal expansion coefficient. As a consequence, the length and/or refractive index of the cavity is highly sensitive to temperature, resulting in a significant alteration of the FPI signal when the temperature changes. The FPI signals of the reported

sensors are commonly operated within the wavelength range of telecommunication. Rong et al. [4] demonstrated a FPI temperature sensor that relies on a polyvinyl alcohol thin film coated at the fiber end. The sensor possesses a temperature sensitivity of 173.5 pm/°C. Li et al. [20] reported a FPI sensor fabricated via two-photon polymerization. The sensor comprises a SU8 cavity containing liquid SU-8 and shows a sensitivity of up to 877 pm/°C in the range of temperature 25 to 60 °C. One significant benefit of temperature sensors based on FPI is their capacity to operate over a wide temperature range while exhibiting ultra-high sensitivity. For instance, Li et al. [21] reported an interferometer comprising an air gap between the end-face of a SMF and an ultrathin graphene film for temperature measurement up to 1008 °C with a high sensitivity of 1.87 nm/°C. Zhu et al. [22] reported an in-fiber FPI sensor where the cavity is formed by splicing a special photonic crystal fiber to a single mode fiber (Figure 1.6). This sensor exhibits a high sensitivity of 17 nm/°C over the range from -20 to 1200 °C.

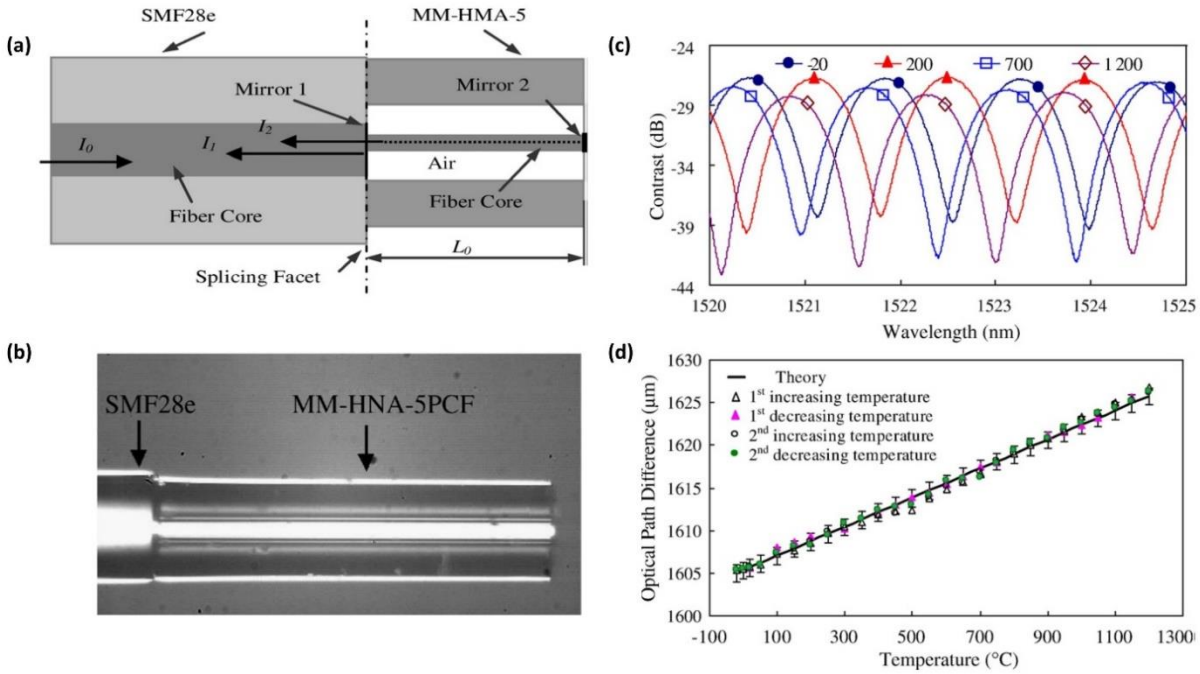

Figure 1. 6. (a) Schematic draw of an in-fiber Fabry–Perot sensor made of splicing different fibers. (b) Photograph of the fabricated sensor. (c) Change of the output spectrum and (d) Temperature dependence of the optical path difference of a Fabry–Perot sensor with a cavity length of 575 μm. This figure is adapted from [22].

1.3.2. Strain measurement

A wide range of FPI sensors have been developed for strain measurement. In general, when the optical cavity of a FPI sensor is subjected to strain, the length of cavity changes, resulting in a shift of FPI signal. By monitoring this shift, one can evaluate the strain applied to the device. This principle makes fiber optic FPI strain sensors potential for Structural Health Monitoring (SHM) applications. However, strain measurements are often affected by variation of temperature due to the thermal expansion of the materials. To develop FPI strain sensors which are insensitive to temperature variation, one usually employs air-cavity configurations because of the small thermal expansion coefficient of the air [23].

Many techniques have been proposed to form FPI strain sensors comprising an air cavity. Rao et al. [8] used a femtosecond laser to machine an air hole inside a fiber. The obtained FPI sensor achieves a strain sensitivity of 6 pm/με and exhibits low sensitive to temperature variation. Another method involves the use of special fibers such as hollow-core fiber photonic crystal fiber [24], hollow-core ring photonic crystal fiber (HCR PCF) [25]. For example, Ferreira et al. [25] spliced a HCR PCR between two sections of SMF to constitute the FPI sensor which exhibits a strain sensitivity of 15.4 pm/με and low temperature sensitivity.

Liu et al. [23] proposed to splice two SMFs that had been previously coated with a matching liquid from Cargille Labs. When arc discharge is applied to splice the SMFs, an air bubble is created inside the splicing junction due to the evaporation of the coated liquid, see Figure 1.7. The resulting sensor shows high strain sensitivity of 43.0 pm/με and low temperature sensitivity.

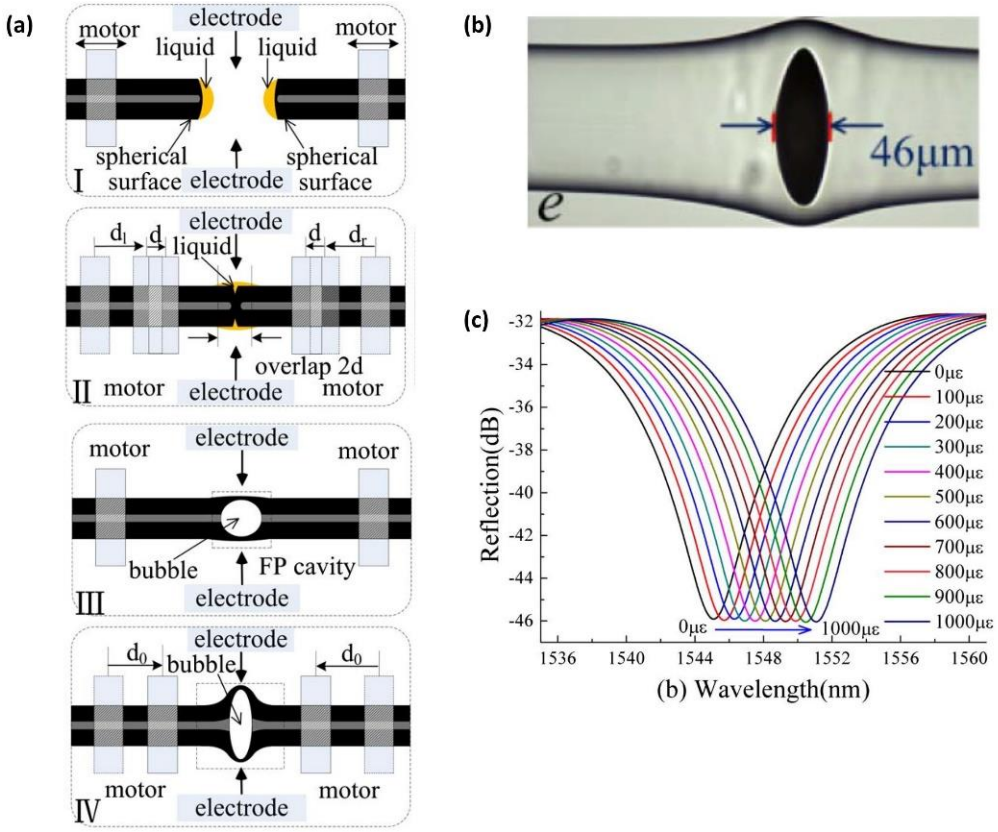

Figure 1. 7. (a) Schematic diagrams of the fabrication process of an in-fiber FPI based on an air bubble. (b) Microscope image of the created air bubble with a cavity length of 46 μm and (c) FPI signal of the sensor as a function of the applied strain. This figure is adapted from Ref [23].

An alternative technique for creating an in-fiber air cavity involves splicing a fiber treated to contain an air hole with an untreated fiber. Yin et al. [26] used hydrofluoric acid to etch a piece of multimode fiber (MMF), producing a hole in the MMF. Subsequently, the etched MMF is spliced to SMF. During the splicing, the etched MMF moves to the SMF, compressing the air in the hole. Consequently, the melted walls of the hole extend outward, forming the bubble-expanded air-cavity. The sensor exhibits a strain sensitivity of 30.66 pm/με. Recently, Zhou et al. [27] used a CO_2 laser dot machining technique to fabricate an air bubble inside a fiber. The machined fiber is then spliced to unmachined fiber to create an all-fiber pillar-in-bubble FPI, that shows a sensitivity of 56.69 pm/με, which is the highest sensitivity among reported FPI strain sensors, to the best of our knowledge.

1.3.3. Pressure measurement

Pressure is a crucial physical parameter in industries such as aerospace, biomedicine, environmental monitoring. Fiber optic FPI sensors have been also developed for measuring pressure. The most common configuration of FPI pressure sensors involve a diaphragm positioned close to a cleaved optical fiber to create a sealed cavity. The diaphragm may consist of materials such as graphene, polyvinyl chloride, UV glue film, or air [28]–[31]. These cavities can be easily deformed under an application of external pressure, leading to a significant change in the interference signal. For instance, Zhang et al. [28] used a femtosecond laser to drill a micro hole in a SMF and then spliced this fiber with another SMF to form a sealed air cavity. This sensor displays a sensitivity of 2.8×10^{-4} nm/Pa and can operate at temperatures up to 700 °C. Ma et al. [29] reported another fiber optic FPI sensor using an ultrathin graphene film. These authors firstly spliced a SMF to a pure silica capillary with an identical outer diameter to make an open cavity. They then sealed the open cavity by a thin film of graphene. The cavity was found to decrease its length with the increase of the external pressure, causing a shift in the FPI signal with a sensitivity of up to 39.4 nm/kPa. In another study, Zhang et al. [30] reported a straightforward-fabricated FPI pressure sensor by welding multilayer polyvinyl chloride diaphragm to the end of well-cut SMF, see Figure 1.8. This sensor exhibits a sensitivity of 65.5 nm/MPa and is insensitive to temperature variation. Recently, Pan et al. [31] designed a FPI pressure sensor based on a UV glue diaphragm. The authors coated a silica tube with a thin layer of UV glue and then spliced it to a SMF to form an optical cavity. When the pressure changes, the cavity length changes as a result of the deformation of the UV glue film, thus leading to a pressure sensor with a sensitivity of 38.3 nm/MPa.

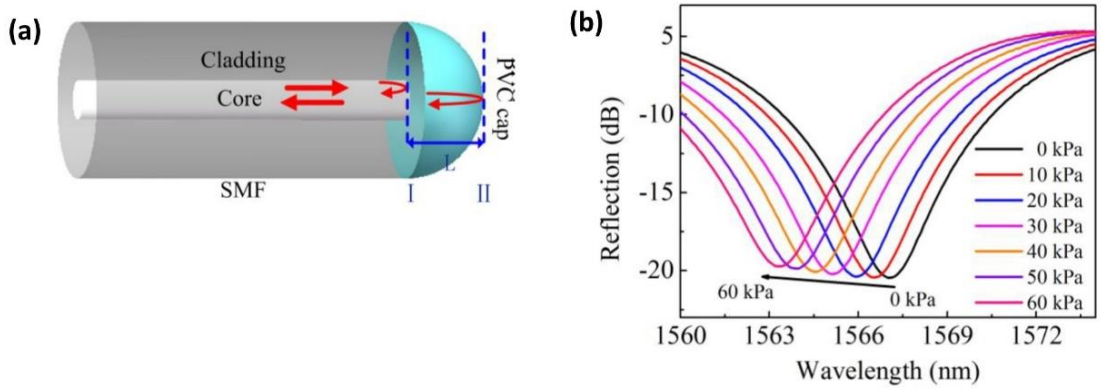

Figure 1. 8. (a) Schematic visualization of an FPI sensor made of a polyvinyl chloride diaphragm welded to the end of a fiber. (b) FPI signal of the proposed sensor with increasing gas pressure from 0 to 60 kPa. This figure is adapted from Ref [30].

Aside from the main sensing principle based on the change in the cavity length, FPI pressure sensors can also function based on the change in the cavity refractive index. Chen at al. [32] designed a FPI sensor consisting of an input SMF and two hollow-core fiber sections with different core diameters (HCF1 and HCF2), see Figure 1.9. The SMF is coaxially spliced to the HCF1 to form the air cavity within the HCF1. The HCF2, with an end coated with Au layer, is spliced off-center to the HCF1. The hollow core of the HCF2 now works as an inlet for introducing gas into the cavity within the HCF1. When the gas pressure changes, the refractive index of the gas in the cavity also changes, causing a change in the FPI signal. The sensor exhibits a pressure sensitivity of 4.314 nm/MPa.

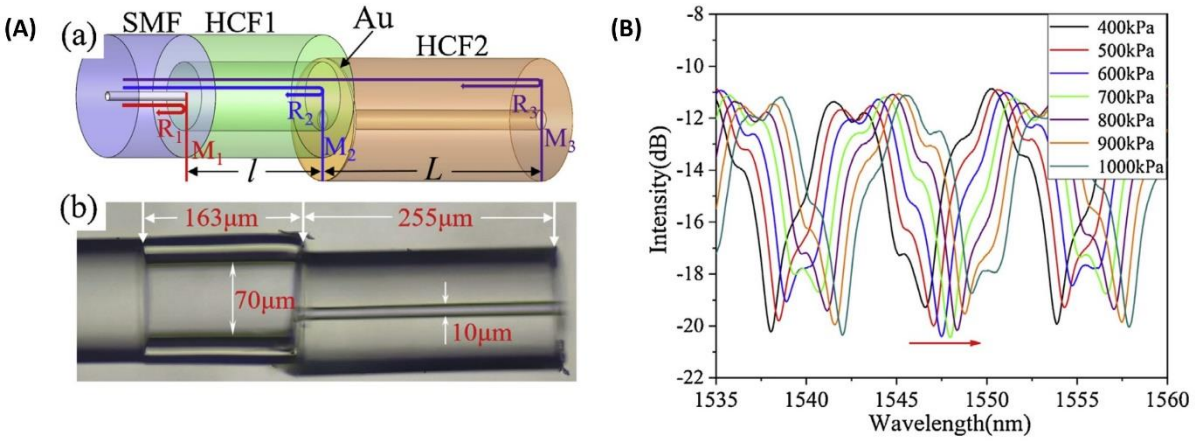

Figure 1. 9. (A) Schematic configuration and optical photograph of a FPI-HCF gas pressure sensor and (B) its FPI signal at different gas pressures within 400 and 1000 kPa. This figure is adapted from Ref [32].

1.4. Application of fiber optic FPI-based sensors for chemical parameters

In addition to detect physical parameters, FPI-based sensors have demonstrated the capability to detect a wide range of chemical parameters, such as relative humidity, refractive index of solutions, and specific target analytes.

1.4.1. Humidity measurement

Humidity refers to the presence of water in gaseous form. In practice, one most frequently uses the relative humidity (RH), which indicates the proportion of the actual vapor pressure of air at a specific temperature to the saturation vapor pressure at the same temperature, given as follows:

$$RH = \frac{P_w}{P_{ws}} \times 100\%$$

where P_w is the partial pressure of water vapor, and P_{ws} is the saturated water vapor pressure at a given temperature.

Humidity measurement is crucially important for human comfort and technical fields such as structural health monitoring applications, chemical processing, food storage, and agriculture [33], [34]. Significant advancements have been made in fiber optic FPI-based sensors for humidity detection and monitoring [15], [35]–[39]. FPI-based sensor for humidity often requires an optical cavity being functionalized by a hygroscopic material. The main working principle of FPI humidity sensors is that the material within the cavity absorbs water molecules from a humid environment and subsequently becomes swelled. The size of the cavity increases, resulting in a shift of the FPI fringes along the wavelength position. Santos et al. [15] reported FPI humidity sensors with a Nafion film deposited on a facet of an optical fiber. Lang et al. [39] presented a polymethyl methacrylate micro-rod grown on the facet of an optical fiber. Chen et al. [35] reported the fabrication of a FPI humidity sensor by splicing a hollow-core fiber (HCF) with a single mode fiber, then coating a chitosan film at the end of the HCF, see Figure 1.10. This sensor exhibits a sensitivity of 0.13 nm/%RH for relative humidity ranging from 20 to 95 %RH and a fast response time of 380 ms.

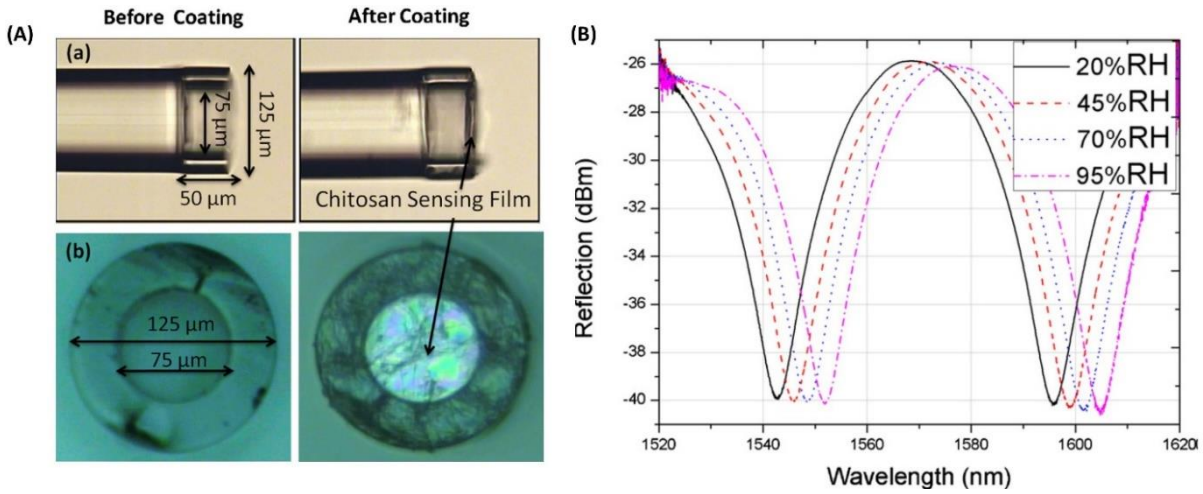

Figure 1. 10. (A) Side view and cross-section view of a FPI sensor made of chitosan coated on the facet of an optical fiber. (B) FPI wavelength shift of the sensor upon exposure to an environment of various humidity. This figure is adapted from Ref [35].

1.4.2. Refractive index measurement

Refractive index is a critical parameter for optical waveguiding and photonic devices. It is also important parameter in bio-chemical field because it directly relates to the concentration of substances. Fiber optic FPIs have been commonly used as refractive index sensors because their FPI signal is highly sensitive to the refractive index of the optical cavity.

Fiber optic FPI sensors for refractive index are typically constructed with an open air-hole cavity in which liquids of different refractive indices can be introduced. The variation of the refractive index of the cavity results in a change in the intensity and wavelength position of the interferometric signal. Wei et al. [10] fabricated a FPI-based sensor with an open micro-notch cavity in a single-mode fiber by using femtosecond laser micromachining. This sensor can measure the dependence of refractive index of water on temperature in the temperature range from 3 to 90 °C with a sensitivity up to 1163 nm/RIU. In another study, Rao et al. [7] utilized air holes in endlessly photonic crystal fiber (EPCF) to measure refractive index. The authors spliced one end of the EPCF to a section of SMF, while capping the other end with another section of SMF. Liquids with varied refractive indices can then penetrate into the air holes of the EPCF, resulting in a change in fringe visibility of the FPI signal. More recently, Zhang et al. [40] machined a micro-hole in a single-mode fiber by laser, see Figure 1.11. When

the micro-hole cavity is filled with various sucrose solutions of different refractive indices, the FPI signal changes with a sensitivity of 1143.0 nm/RIU.

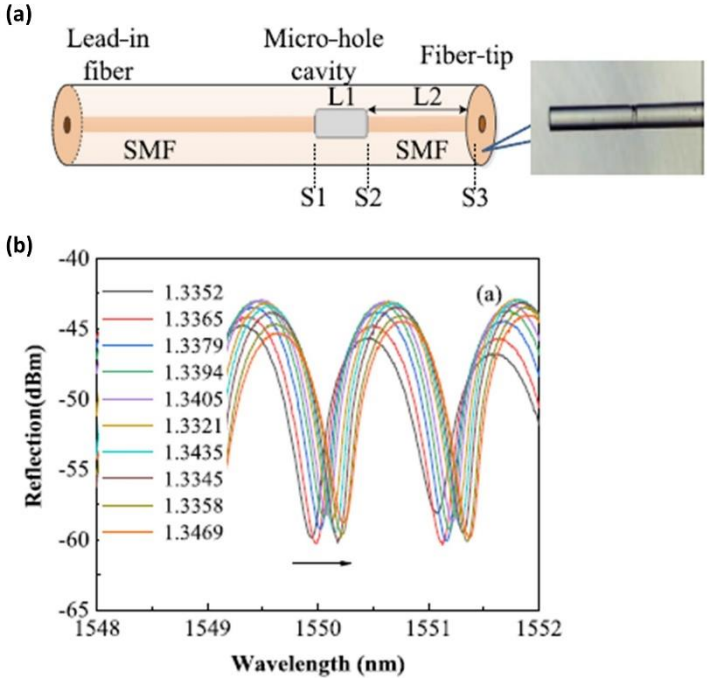

Figure 1. 11. (a) Schematic diagram of a machined micro-hole in single-mode fiber and (b) its FPI signal versus the refractive index of the liquid within the cavity. This figure is adapted from [40].

1.4.3. Desired target detection

Fiber optic FPI-based sensors are capable of detecting certain types of analytes by measuring their refractive index. However, this approach is inappropriate for chemical and biological sensing applications due to its low selectivity. Consequently, functional materials are normally incorporated within the fiber optic FPI to address this issue [41]. To detect a desired target, it is essential to select and synthesize suitable functional materials which can effectively and selectively bind to the target molecules. This binding makes the FPI cavity to change in length or refractive index, resulting in an FPI signal change. The detection of the target can be therefore observed from the spectra signal of the FPI-based sensor.

Fiber optic FPI sensors have been widely used for the detection of glucose. The optical cavity of the FPI sensor is incorporated with responsive materials which can form covalent bonds with glucose. These materials can be phenylboronic acid derivatives [42], [43], concanavalin A [44], and glucose oxidase [45]. Zhang et al. [43] developed a multilayer film

consisting of poly(vinylalcohol) (PVA) and poly-(acrylamide-co-3(acrylamido)phenylboronic acid) (P(AAm-AAPBA) on the facet of SMF, forming an FPI sensor (Figure 1.12). When the sensor is immersed in glucose solutions, the glucose binds to the free phenylboronic acid (PBA) groups, converting them from hydrophobic to hydrophilic; or compete with PVA for the PBA binding site. In both ways, the binding of glucose to the PBA groups makes the film swelled significantly, resulting in a variation of the FPI signal. In another study, Li et al. [44] constructed a FPI cavity using a hydrogel film composed of concanavalin A (Con A) and dextran (Dex). The initial hydrogen film is actually a crosslinked 3D network of Con A binding with glucosyl residue on Dex chains. Once this film is submerged in glucose solutions, glucose molecules compete with glycosyl residues on Dex chains for binding to Con A, making the film swelled. Thus, based on the FPI signal shift of the swelled film, the authors can detect glucose in the range of 0 to 70 mM. Wang et al. [45] reported a FPI sensor using a pH-sensitive hydrogel film comprising of oxidized dextran (PO-Dex), chitosan, and glucose oxidase (GOD). In the presence of glucose, GOD catalyzes the oxidation conversion of glucose to gluconic acid, which then lowers the local pH of the film. The reduced pH further triggers the film to swell, leading to a shift in the FPI signal. The sensor shows good selectivity and can detect glucose within the range of 0-20 mM.

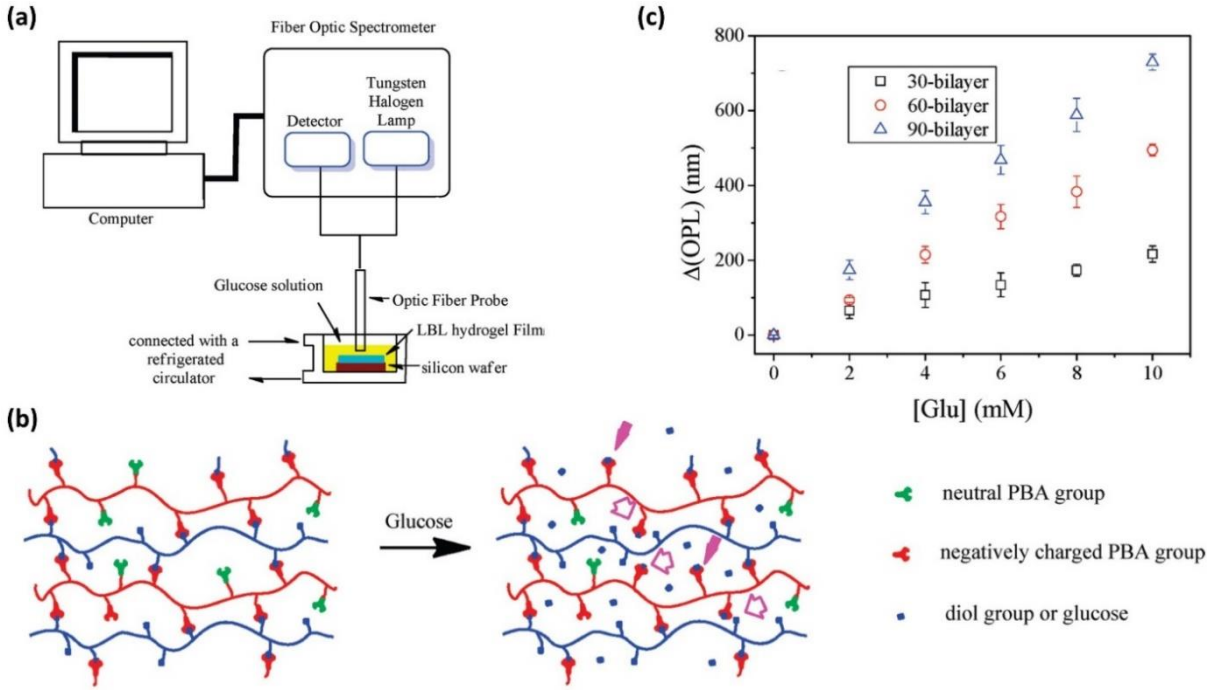

Figure 1. 12. (a) Experimental setup for the detection of glucose. (b) Schematic draw showing the binding between glucose and PBA groups in the film. (c) Glucose-induced changes in optical path length of the multilayer films. This figure is adapted from [43].

Fiber optic FPIs are also used for detecting antigens if the optical cavity is functionalized with antibodies. The affinity binding between antigen and antibody triggers a change in the length and/or refractive index of the FPI cavity, resulting in a change in the FPI signal. Chen et al. [46] developed a FPI sensor to detect anti-immunoglobulin (anti-IgG), see Figure 1.13. The authors first spliced a single mode fiber (SMF) with a hollow core fiber (HCF). They then dip-coated a layer of chitosan onto the end-face of the HCF and subsequently functionalized the chitosan surface with antibody bovine immunoglobulin-g IgG. The binding between immobilized IgG and anti-IgG makes the FPI cavity changes in length, allowing the sensor to detect anti-IgG with a sensitivity of 0.033 μm/(pg/mm^2) and a limit of detection of 0.005 nM. In another study, Liu et al. [47] also reported a FPI sensor to detect a specific rabbit IgG. They spliced a short section of hollow-core photonic crystal fiber in between two single mode fibers (SMF) before immobilizing the SMF end surface with antibody molecules (goat anti-rabbit IgG). Upon immersing the sensor in a rabbit IgG solution, the rabbit IgG specifically binds to the immobilized anti-rabbit IgG, increasing the sensing layer thickness and consequently resulting in the FPI signal change.

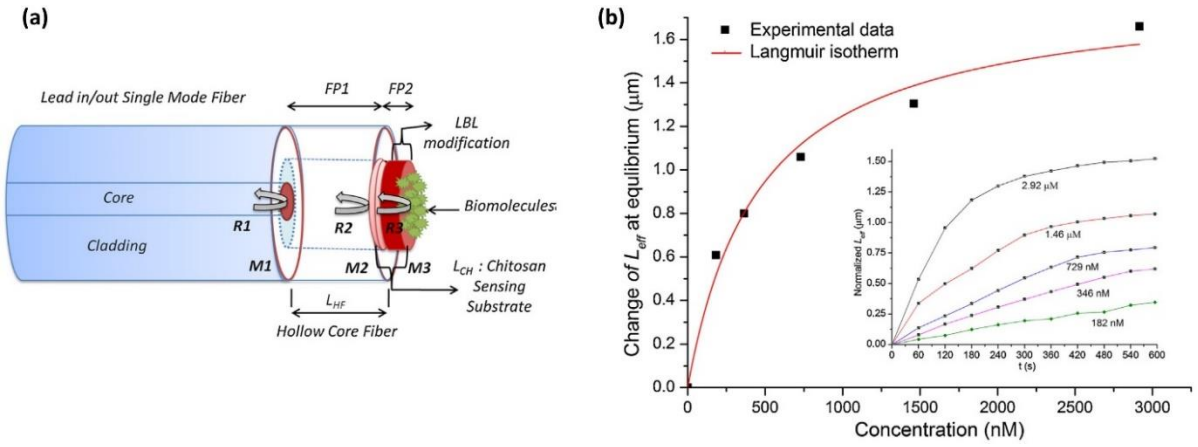

Figure 1. 13. Schematic diagram of the chitosan substrate based FPI for detecting anti-IgG. (b) Change in cavity length as a function of anti-IgG concentration, inset shows normalized length response during binding of anti-IgG at various concentration. This figure is adapted from [46].

In another example, fiber optic FPIs combined with molecularly imprinted polymers (MIP) have the ability to detect a desired chemical target. Molecularly imprinted polymers are artificial polymeric receptors that can be synthesized by polymerizing functional and cross-linking monomers in the presence of a molecular target or its derivative as a template [48]. The molecular template is then removed from the MIP structure, resulting in available empty binding sites, see Figure 1.14 [48]. These sites can recognize and bind chemicals that are complementary in shape, size, and functional groups to the previously removed template. MIPs are chemically stable and easily integrated into industrial manufacturing. Moreover, they can also be tailored to specific molecules of interest, making them comparable to natural receptors. Thanks to these advantages, MIPs have found applications across various fields, including drug delivery, cosmetics and catalysis. They are especially suitable for (bio)chemical sensors with a high affinity and selectivity.

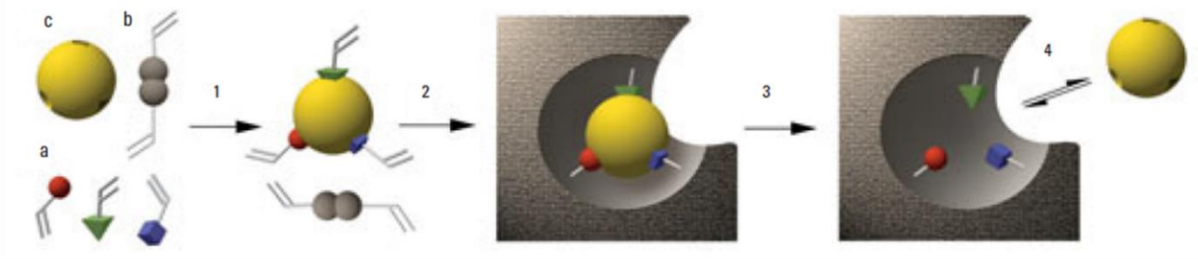

Figure 1. 14. General principle of molecular imprinting. A molecular template (c) is mixed with functional monomers (a) and a cross-linker (b) resulting in the formation of a self-assembled complex (1). The polymerization of the resulting system produces a rigid structure (2). Subsequent removal of the template liberates cavities (3) that can specifically recognize and bind the target molecule (4). This figure is adapted from Ref [48].

One can take advantage of the binding ability of MIP with specific chemical targets to build FPI chemical sensors. If the optical cavity of the FPI is functionalized by MIP, the refractive index of the cavity is expected to be changed upon the binding of MIP with analyte targets, resulting in a shift in the FPI signal. Indeed, Queirós et al. [49] reported a fiber optic FPI chemical sensor using MIP for the detection of microcystin-LR, see Figure 1.15. In this study, the authors formulated a membrane of MIP on the fiber facet by dip-coating the fiber in a sol-gel MIP solution. This study demonstrates a potential fiber optic FPI-based MIP for the sensitive and selective sensing of chemical analytes. The advantage of the FPI chemical sensors is that they can be used for a wide range of analytes, including both non-fluorescent and fluorescent targets.

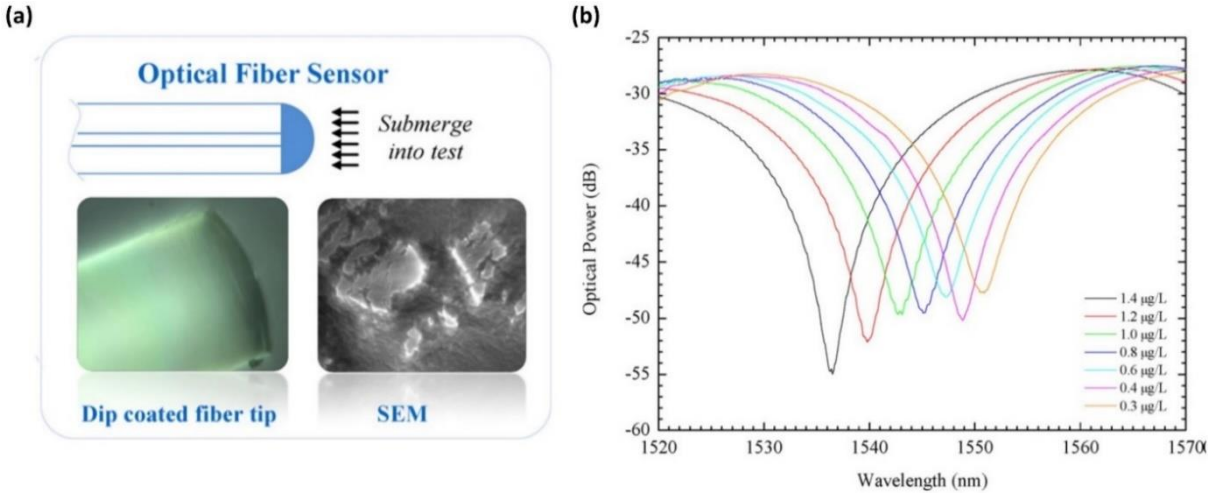

Figure 1. 15. (a) Scheme of the Fabry–Pérot cavity based on MIP sol–gel membrane on the facet of an optical fiber. (b) Optical power and wavelength shift variation according to the concentration of microcystin-LR using the FPI based MIP sol–gel membrane. This figure is adapted from [49].

1.5. Aims and outline of the thesis

Fiber optic FPI sensors with various designs have been developed in recent decades. They exhibit a great potential for detecting different physical and chemical parameters. However, available methods for making FPI-based sensors such as fiber splicing, direct laser writing, and chemical etching are often complicated and requires specific skills and expensive equipment. Hence, there is still a high demand for the creation of fiber optic FPI-based sensors featuring a simpler design and a more affordable production method. In addition, the FPI sensor reported in the literature is typically suitable for a single sensing application. It would be an attractive research objective to develop an FPI-based sensor that can function effectively in multiple sensing applications. Hence, this thesis aims to develop a simply structured fiber optic FPI-based sensor which can effectively detect humidity, water, and chemical targets.

This thesis consists of six chapters. Apart from the first introductory chapter for background of FPI and motivation of the thesis which is currently presented, the four research chapters addressing different objectives and the final chapter for conclusion are organized as follows:

Chapter 2 presents the development of a micro-length tip made of pentaerythritol triacrylate (PETA) on the facet of an optical fiber by self-guiding photopolymerization. The

formation of the tip is optimized in term of injected laser power and exposure time to achieve a straight and mechanical stable tip. The polymerization extent of PETA chains is indirectly characterized by dynamic resonant frequency measurement and subsequently improved by a post-polymerization under a UV irradiation.

Chapter 3 demonstrates the application of the p(PETA) tip as an FPI-based sensor for detecting humidity in the air. The p(PETA) tip acts as an optical cavity formed between the fiber-core/PETA and the PETA/air interface, resulting in a clear interferometric signal. The FPI signal of the tip is highly sensitive to humidity in the air. This performance is based on a strong water absorption of OH- groups within the PETA structure, causing significant swelling of the tip. The length and/or the refractive index of the tip are therefore changed, resulting in an FPI shift.

Chapter 4 proposes a new and simple method of using the p(PETA) tip as an FPI-based sensor for detecting water content in glycerol and ethylene glycol solutions. The working principle of the sensor is based on the absorption and desorption of water molecules within the PETA structure when the tip is in contact with water and hydroscopic solutions, respectively. When the water is below 10 wt.% in the solution, the shift of the FPI signal is linearly dependent on the water content. This makes the tip usable as a water sensor for hygroscopic aqueous solutions, including hydrocarbons.

Chapter 5 presents the development of a tip comprising a core of p(PETA) and a shell of molecularly imprinted polymers (MIPs) which can be used as an FPI-based sensor for detecting Dansyl-L-phenylalanine. The p(PETA) tip is initially fabricated using the self-guiding polymerization and a shell layer of MIP is subsequently formed around the p(PETA) tip. Upon binding to Dansyl-L-phenylalanine, the refractive index of the MIP layer changes, leading to the change in the FPI signal of the whole p(PETA)/MIP tip. This straightforward method offers new innovative possibilities for designing MIP-based FPI sensors for a wide range of analytes.

Chapter 6 summarizes the main findings of the thesis and suggests some future research objectives for further improving the performance of the fiber optic FPI-based sensor made from the p(PETA) tip.

References

[1] Y.-J. Rao, Z.-L. Ran, and Y. Gong, *Fiber-optic Fabry-Perot sensors: an introduction*. in Series in fiber optic sensors. Boca Raton London New York: CRC Press, Taylor & Francis Group, 2017.

[2] Z. L. Ran, Y. J. Rao, W. J. Liu, X. Liao, and K. S. Chiang, 'Laser-micromachined Fabry-Perot optical fiber tip sensor for high-resolution temperature-independent measurement of refractive index', *Opt. Express*, vol. 16, no. 3, p. 2252, 2008, doi: 10.1364/OE.16.002252.

[3] J.-R. Zhao, X.-G. Huang, W.-X. He, and J.-H. Chen, 'High-Resolution and Temperature-Insensitive Fiber Optic Refractive Index Sensor Based on Fresnel Reflection Modulated by Fabry–Perot Interference', *J. Lightwave Technol.*, vol. 28, no. 19, pp. 2799–2803, Oct. 2010, doi: 10.1109/JLT.2010.2065215.

[4] Q. Rong, H. Sun, X. Qiao, J. Zhang, M. Hu, and Z. Feng, 'A miniature fiber-optic temperature sensor based on a Fabry–Perot interferometer', *J. Opt.*, vol. 14, no. 4, p. 045002, Apr. 2012, doi: 10.1088/2040-8978/14/4/045002.

[5] B. H. Lee, Y. H. Kim, K. S. Park, J. B. Eom, M. J. Kim, B. S. Rho, and H. Y. Choi, 'Interferometric Fiber Optic Sensors', *Sensors*, vol. 12, no. 3, pp. 2467–2486, Feb. 2012, doi: 10.3390/s120302467.

[6] Woo-Hu Tsai and Chun-Jung Lin, 'A novel structure for the intrinsic Fabry-Perot fiber-optic temperature sensor', *J. Lightwave Technol.*, vol. 19, no. 5, pp. 682–686, May 2001, doi: 10.1109/50.923481.

[7] Y.-J. Rao, M. Deng, D.-W. Duan, and T. Zhu, 'In-line fiber Fabry-Perot refractive-index tip sensor based on endlessly photonic crystal fiber', *Sensors and Actuators A: Physical*, vol. 148, no. 1, pp. 33–38, Nov. 2008, doi: 10.1016/j.sna.2008.06.030.

[8] Y.-J. Rao, M. Deng, D.-W. Duan, X.-C. Yang, T. Zhu, and G.-H. Cheng, 'Micro Fabry-Perot interferometers in silica fibers machined by femtosecond laser', *Opt. Express*, vol. 15, no. 21, p. 14123, 2007, doi: 10.1364/OE.15.014123.

[9] T. Wei, Y. Han, H.-L. Tsai, and H. Xiao, 'Miniaturized fiber inline Fabry-Perot interferometer fabricated with a femtosecond laser', *Opt. Lett.*, vol. 33, no. 6, p. 536, Mar. 2008, doi: 10.1364/OL.33.000536.

[10] T. Wei, Y. Han, Y. Li, H.-L. Tsai, and H. Xiao, 'Temperature-insensitive miniaturized fiber inline Fabry-Perot interferometer for highly sensitive refractive index measurement', *Opt. Express*, vol. 16, no. 8, p. 5764, Apr. 2008, doi: 10.1364/OE.16.005764.

[11] V. R. Machavaram, R. A. Badcock, and G. F. Fernando, 'Fabrication of intrinsic fibre Fabry–Perot sensors in silica fibres using hydrofluoric acid etching', *Sensors and Actuators A: Physical*, vol. 138, no. 1, pp. 248–260, Jul. 2007, doi: 10.1016/j.sna.2007.04.007.

[12] P. A. R. Tafulo, Pedro. A. S. Jorge, J. L. Santos, F. M. Araujo, and O. Frazao, 'Intrinsic Fabry–Pérot Cavity Sensor Based on Etched Multimode Graded Index Fiber for Strain and Temperature Measurement', *IEEE Sensors J.*, vol. 12, no. 1, pp. 8–12, Jan. 2012, doi: 10.1109/JSEN.2011.2107737.

[13] D.-H. Kim, J.-W. Park, H.-K. Kang, C.-S. Hong, and C.-G. Kim, 'Measuring dynamic strain of structures using a gold-deposited extrinsic Fabry Perot interferometer', *Smart Mater. Struct.*, vol. 12, no. 1, pp. 1–5, Feb. 2003, doi: 10.1088/0964-1726/12/1/301.

[14] D. Duan, Y. Rao, and T. Zhu, 'High sensitivity gas refractometer based on all-fiber open-cavity Fabry–Perot interferometer formed by large lateral offset splicing', *J. Opt. Soc. Am. B*, vol. 29, no. 5, p. 912, May 2012, doi: 10.1364/JOSAB.29.000912.

[15] J. S. Santos, I. M. Raimundo, C. M. B. Cordeiro, C. R. Biazoli, C. A. J. Gouveia, and P. A. S. Jorge, 'Characterisation of a Nafion film by optical fibre Fabry–Perot interferometry for humidity sensing', *Sensors and Actuators B: Chemical*, vol. 196, pp. 99–105, Jun. 2014, doi: 10.1016/j.snb.2014.01.101.

[16] X. L. Tan, Y. F. Geng, X. J. Li, Y. L. Deng, Z. Yin, and R. Gao, 'UV-Curable Polymer Microhemisphere-Based Fiber-Optic Fabry–Perot Interferometer for Simultaneous Measurement of Refractive Index and Temperature', *IEEE Photonics J.*, vol. 6, no. 4, pp. 1–8, Aug. 2014, doi: 10.1109/JPHOT.2014.2332460.

[17] T. T. Salunkhe, D. J. Lee, H. K. Lee, H. W. Choi, S. J. Park, and I. T. Kim, 'Enhancing Temperature Sensitivity of the Fabry–Perot Interferometer Sensor with Optimization of the Coating Thickness of Polystyrene', *Sensors*, vol. 20, no. 3, p. 794, Jan. 2020, doi: 10.3390/s20030794.

[18] O. Frazão, P. Caldas, J. L. Santos, P. V. S. Marques, C. Turck, D. J. Lougnot, and O. Soppera, 'Fabry-Perot refractometer based on an end-of-fiber polymer tip', *Opt. Lett.*, vol. 34, no. 16, p. 2474, Aug. 2009, doi: 10.1364/OL.34.002474.

[19] Z. Hu, Y. Chen, J. Tan, Z. Yan, Z. Weng, M. Gusain, Y. Zhan, and L. Xiao, 'A hybrid self-growing polymer microtip for ultracompact and fast fiber humidity sensing', *Sensors and Actuators B: Chemical*, vol. 346, p. 130462, Nov. 2021, doi: 10.1016/j.snb.2021.130462.

[20] M. Li, Y. Liu, R. Gao, Y. Li, X. Zhao, and S. Qu, 'Ultracompact fiber sensor tip based on liquid polymer-filled Fabry-Perot cavity with high temperature sensitivity', *Sensors and Actuators B: Chemical*, vol. 233, pp. 496–501, Oct. 2016, doi: 10.1016/j.snb.2016.04.121.

[21] L. Li, Z. Feng, X. Qiao, H. Yang, R. Wang, D. Su, Y. Wang, W. Bao, J. Li, Z. Shao, and M. Hu, 'Ultrahigh Sensitive Temperature Sensor Based on Fabry–Pérot Interference Assisted by a Graphene Diaphragm', *IEEE Sensors J.*, vol. 15, no. 1, pp. 505–509, Jan. 2015, doi: 10.1109/JSEN.2014.2361174.

[22] T. Zhu, T. Ke, Y. Rao, and K. S. Chiang, 'Fabry–Perot optical fiber tip sensor for high temperature measurement', *Optics Communications*, vol. 283, no. 19, pp. 3683–3685, Oct. 2010, doi: 10.1016/j.optcom.2010.05.037.

[23] S. Liu, Y. Wang, C. Liao, G. Wang, Z. Li, Q. Wang, J. Zhou, K. Yang, X. Zhong, J. Zhao, and J. Tang, 'High-sensitivity strain sensor based on in-fiber improved Fabry–Perot interferometer', *Opt. Lett.*, vol. 39, no. 7, p. 2121, Apr. 2014, doi: 10.1364/OL.39.002121.

[24] Y. J. Rao, T. Zhu, X. C. Yang, and D. W. Duan, 'In-line fiber-optic etalon formed by hollow-core photonic crystal fiber', *Opt. Lett.*, vol. 32, pp. 2662–2664, 2007, doi: 10.1364/OL.32.002662.

[25] M. S. Ferreira, J. Bierlich, J. Kobelke, K. Schuster, J. L. Santos, and O. Frazão, 'Towards the control of highly sensitive Fabry-Pérot strain sensor based on hollow-core ring photonic crystal fiber', *Opt. Express*, vol. 20, no. 20, p. 21946, Sep. 2012, doi: 10.1364/OE.20.021946.

[26] Y. Chenchen, C. Zhigang, Z. Zhao, S. Tao, W. Rui, W. Jian, L. Liang, Z. Shenglai, and Y. Benli, 'Temperature-Independent Ultrasensitive Fabry–Perot All-Fiber Strain Sensor Based on a Bubble-Expanded Microcavity', *IEEE Photonics J.*, vol. 6, no. 4, pp. 1–9, Aug. 2014, doi: 10.1109/JPHOT.2014.2345883.

[27] K. Zhou, M.-Z. Ai, Z.-H. Qian, X.-X. Gao, Z.-H. Hu, Q. Li, L. Yuan, Z. Wang, Y.-F. Huang, T. Tu, J.-M. Cui, C.-F. Li, and G.-C. Guo, 'High-sensitivity strain sensor with an in-fiber air-bubble Fabry-Perot interferometer', *Applied Physics Letters*, vol. 113, no. 18, p. 181901, Oct. 2018, doi: 10.1063/1.5058200.

[28] Y. Zhang, L. Yuan, X. Lan, A. Kaur, J. Huang, and H. Xiao, 'High-temperature fiber-optic Fabry–Perot interferometric pressure sensor fabricated by femtosecond laser', *Opt. Lett.*, vol. 38, no. 22, p. 4609, Nov. 2013, doi: 10.1364/OL.38.004609.

[29] J. Ma, W. Jin, H. L. Ho, and J. Y. Dai, 'High-sensitivity fiber-tip pressure sensor with graphene diaphragm', *Opt. Lett.*, vol. 37, no. 13, p. 2493, Jul. 2012, doi: 10.1364/OL.37.002493.

[30] Z. Zhang, C. Liao, J. Tang, Z. Bai, K. Guo, M. Hou, J. He, Y. Wang, S. Liu, F. Zhang, and Y. Wang, 'High-Sensitivity Gas-Pressure Sensor Based on Fiber-Tip PVC Diaphragm Fabry–Pérot Interferometer', *J. Lightwave Technol.*, vol. 35, no. 18, pp. 4067–4071, Sep. 2017, doi: 10.1109/JLT.2017.2710210.

[31] R. Pan, W. Yang, L. Li, Y. Yang, X. Yu, J. Fan, S. Yu, Y. Xiong, and L. Zhang, 'High-sensitive fiber-optic pressure sensor based on Fabry-Perot interferometer filled with ultraviolet glue film and Vernier effect', *Optical Fiber Technology*, vol. 67, p. 102710, Dec. 2021, doi: 10.1016/j.yofte.2021.102710.

[32] M. Chen, H. Wei, Y. Zhao, X. Lei, and S. Krishnaswamy, 'Temperature insensitive air-cavity Fabry-Perot gas pressure sensor based on core-offset fusion of hollow-core fibers', *Sensors and Actuators A: Physical*, vol. 298, p. 111589, Oct. 2019, doi: 10.1016/j.sna.2019.111589.

[33] T. L. Yeo, T. Sun, and K. T. V. Grattan, 'Fibre-optic sensor technologies for humidity and moisture measurement', *Sensors and Actuators A: Physical*, vol. 144, no. 2, pp. 280–295, Jun. 2008, doi: 10.1016/j.sna.2008.01.017.

[34] X. Wang, and O. S. Wolfbeis, 'Fiber-Optic Chemical Sensors and Biosensors (2015−2019)', *Analytical Chemistry*, vol. 92, no. 1, pp. 397–430, 2020, doi: 10.1021/acs.analchem.9b04708.

[35] L. H. Chen, T. Li, C. C. Chan, R. Menon, P. Balamurali, M. Shaillender, B. Neu, X. M. Ang, P. Zu, W. C. Wong, and K. C. Leong, 'Chitosan based fiber-optic Fabry–Perot humidity sensor', *Sensors and Actuators B: Chemical*, vol. 169, pp. 167–172, Jul. 2012, doi: 10.1016/j.snb.2012.04.052.

[36] Y. Zhao, R. Tong, M.-Q. Chen, and F. Xia, 'Relative humidity sensor based on hollow core fiber filled with GQDs-PVA', *Sensors and Actuators B: Chemical*, vol. 284, pp. 96–102, Apr. 2019, doi: 10.1016/j.snb.2018.12.130.

[37] Y. Zhao, Y. Yuan, W. Gan, and M. Yang, 'Optical fiber Fabry–Perot humidity sensor based on polyimide membrane: Sensitivity and adsorption kinetics', *Sensors and Actuators A: Physical*, vol. 281, pp. 48–54, Oct. 2018, doi: 10.1016/j.sna.2018.08.044.

[38] S. Wu, G. Yan, Z. Lian, X. Chen, B. Zhou, and S. He, 'An open-cavity Fabry-Perot interferometer with PVA coating for simultaneous measurement of relative humidity and temperature', *Sensors and Actuators B: Chemical*, vol. 225, pp. 50–56, Mar. 2016, doi: 10.1016/j.snb.2015.11.015.

[39] C. Lang, Y. Liu, K. Cao, Y. Li, and S. Qu, 'Ultra-compact, fast-responsive and highly-sensitive humidity sensor based on a polymer micro-rod on the end-face of fiber core', *Sensors and Actuators B: Chemical*, vol. 290, pp. 23–27, Jul. 2019, doi: 10.1016/j.snb.2019.03.099.

[40] W. Zhang, Y. Liu, T. Zhang, D. Yang, Y. Wang, and D. Yu, 'Integrated Fiber-Optic Fabry-Pérot Interferometer Sensor for Simultaneous Measurement of Liquid Refractive Index and Temperature', *IEEE Sensors J.*, vol. 19, no. 13, pp. 5007–5013, Jul. 2019, doi: 10.1109/JSEN.2019.2903583.

[41] M. Yin, B. Gu, Q.-F. An, C. Yang, Y. L. Guan, and K.-T. Yong, 'Recent development of fiber-optic chemical sensors and biosensors: Mechanisms, materials, micro/nano-fabrications and applications', *Coordination Chemistry Reviews*, vol. 376, pp. 348–392, Dec. 2018, doi: 10.1016/j.ccr.2018.08.001.

[42] S. Tierney, S. Volden, and B. T. Stokke, 'Glucose sensors based on a responsive gel incorporated as a Fabry-Perot cavity on a fiber-optic readout platform', *Biosensors and Bioelectronics*, vol. 24, no. 7, pp. 2034–2039, Mar. 2009, doi: 10.1016/j.bios.2008.10.014.

[43] X. Zhang, Y. Guan, and Y. Zhang, 'Ultrathin Hydrogel Films for Rapid Optical Biosensing', *Biomacromolecules*, vol. 13, no. 1, pp. 92–97, Jan. 2012, doi: 10.1021/bm2012696.

[44] Q. Li, Y. Guan, and Y. Zhang, 'Thin hydrogel films based on lectin-saccharide biospecific interaction for label-free optical glucose sensing', *Sensors and Actuators B: Chemical*, vol. 272, pp. 243–251, Nov. 2018, doi: 10.1016/j.snb.2018.05.166.

[45] X. Wang, Q. Li, Y. Guan, and Y. Zhang, 'Glucose oxidase-incorporated hydrogel thin film for fast optical glucose detecting under physiological conditions', *Materials Today Chemistry*, vol. 1–2, pp. 7–14, Oct. 2016, doi: 10.1016/j.mtchem.2016.10.005.

[46] L. H. Chen, C. C. Chan. R. Menon, P. Balamurali, W. C. Wong, X. M. Ang, P. B. Hu, M. Shaillender, B. Neu, P. Zu, Z. Q. Tou, C. L. Poh, and K. C. Leong, 'Fabry–Perot fiber-optic

immunosensor based on suspended layer-by-layer (chitosan/polystyrene sulfonate) membrane', *Sensors and Actuators B: Chemical*, vol. 188, pp. 185–192, Nov. 2013, doi: 10.1016/j.snb.2013.06.093.

[47] X. Liu, M. Jiang, T. Dong, Q. Sui, and X. Geng, 'Label-Free Immunosensor Based on Optical Fiber Fabry–Perot Interferometer', *IEEE Sensors J.*, vol. 16, no. 20, pp. 7515–7520, Oct. 2016, doi: 10.1109/JSEN.2016.2600632.

[48] K. Haupt, A.V. Linares, M. Bompart, and B. Tse Sum Bui, 'Molecularly Imprinted Polymers', Top. Curr. Chem., vol. 325, pp. 1–28, 2012, doi: 10.1007/128_2011_307.

[49] R. B. Queirós, S. O. Silva, J. P. Noronha, O. Frazão, P. Jorge, G. Aguilar, P. V. S. Marques, and M. G. F. Sales, 'Microcystin-LR detection in water by the Fabry–Pérot interferometer using an optical fibre coated with a sol–gel imprinted sensing membrane', *Biosensors and Bioelectronics*, vol. 26, no. 9, pp. 3932–3937, May 2011, doi: 10.1016/j.bios.2011.03.015.

Chapter 2

Elaboration of a polymer tip at the end of optical fiber for Fabry-Perot interferometer sensor

Abstract. A polymer tip attached to the end of an optical fiber can function as a Fabry-Perot interferometer (FPI), which is promising for sensor applications. The formation of the polymer tip is significantly more straightforward and cost-effective than other FPI creation techniques. This chapter presents in detail the development of a polymer tip, made by pentaerythritol triacrylate (PETA), on the facet of an optical fiber by self-guiding polymerization. One end of the optical fiber is stably placed inside a PETA droplet while the other end of the fiber is injected by a 375-nm laser. The laser actuates self-guiding polymerization of PETA chains, resulting in a cylindrical tip on the facet of the fiber. The formation of the PETA tip is strongly influenced by the exposure dose (injected laser power × exposure time). An inefficient exposure dose produces a tip with unstable mechanical strength while an over dose results in a tip with an enlarged head. The optimal dose corresponds to an injected laser power of 1.0 μW during an exposure time of 1.0 s, forming a mechanically strong PETA tip with a straight form. However, the p(PETA) tip exhibit inconsistent dynamic resonant frequencies. This is attributed to the incomplete polymerization of the PETA chains during the self-polymerization process. The PETA tip therefore needs a post-polymerization under a 365-nm UV lamp for a minimum of 3 h. The final PETA tip exhibits a clear and stable dynamic resonant frequency, making it potential for future sensor applications.

2.1. Introduction

In practical applications, Fabry-Perot interferometers (FPI) are commonly accompanied with optical fibers to form compact sensor devices. The optical fibers work as a waveguide for incident and reflected signal. The sensors are therefore not only more compact, but also provide enhanced performance efficiency. As seen in the introduction, fiber optic FPI-based sensors are categorized as either intrinsic FPI, where the optical cavity is located inside the optical fiber or extrinsic FPI, where the optical cavity is located outside the optical fiber [1], [2].

The fabrication technique of the optical cavity is crucial in determining the reflection coefficients, mechanical strength and stability of the cavity, as well as the cost of the device. All of these parameters directly decide the practical application of the FPI sensor. Previously developed intrinsic FPI sensors usually require expensive equipment, specialized skills and dangerous chemical reagents. For instance, one splices optical fibers with mismatched refractive-index [3], [4]. Another technique is using of femtosecond lasers to form a micro-notch inside the optical fiber [5]–[7]. Chemical etching can also be used to create an air hole inside the fiber and the etched fibers are subsequently spliced to form an intrinsic FPI sensor [8], [9]. Some available extrinsic FPI sensors have been also created by splicing optical fibers. For instance, Kim et al. [10] used a silica capillary tube to bond two optical fibers which are separated by an air gap with epoxy. Duan et al. [11] created an air cavity by splicing a short SMF section between two other SMFs with a large lateral offset. The gap between the fibers works as an open cavity where external gas or liquid can enter or exit easily, making it suitable for sensing the refractive index of the surrounding medium. Again, these fabrication techniques require specialized skills and equipment.

In the attempt to produce cost-effective devices, one has proposed extrinsic FPI sensors involving a coated layer or a grown micro tip of an environmentally sensitive material, typically polymers, on the facet of an optical fiber [12]–[17]. In this design, the optical cavity is formed between the fiber-facet/polymer interface and the polymer/ambient interface. The thickness of the deposited polymer layer is controlled manually and roughly by either using different aliquot solutions [13], or adjusting the concentration of the precursor solutions [15], or by using fibers with different diameters [14]. Meanwhile, the polymer tip can be formed

rapidly at the end of the optical fiber by self-guiding photo-polymerization [16], [17]. The polymer tip itself forms an optical cavity that functions directly as an FPI. However, the study of this end-of-fiber polymer tip for sensor applications still remains limited. Moreover, the self-guiding photo-polymerization process occurs rapidly, which might result in a tip with insufficient mechanical strength and an inconsistent refractive index. These problems could lead to imprecise and inconsistent performance of the tip during sensing measurements. Therefore, it is necessary to employ a method for assessing the quality of the tips following their fabrication.

In this chapter, we first present the fabrication of a pentaerythritol triacrylate (PETA) polymer tip attached to the end of an optical fiber by self-guiding photo-polymerization method. A UV laser is injected at one end of the optical fiber, illuminating a droplet of the PETA solution where the other end of the fiber is dipped. The photo-polymerization of PETA is activated, allowing a solid polymer tip to grow from the optical fiber facet. The laser power and exposure duration are carefully optimized to obtain a polymer tip with relatively straight shape. We then study the dynamic characteristics (i.e. resonant frequency) of the polymer tip using a home-made setup and a laser Doppler vibrometer (LDV). Based on these results, we show that the photo-polymerization of the PETA chains within the as-prepared tip is incomplete. To ensure a fully complete polymerization of the polymer chains within the tip, we conduct post-polymerization process by either exposing the tip to a UV lamp or injecting the UV laser to the tip through the optical fiber. The resulting PETA tip with a full complete polymerization of the polymer chains is then ready for sensor applications as presented in the following chapters.

2.2. Fabrication of a polymer tip on the facet of an optical fiber

2.2.1. Materials

The polymer selected in this work is pentaerythritol triacrylate (PETA), which is curable under UV irradiation, enabling a quick formation of well-defined polymerized tips at the end of optical fibers. Also, thanks to three polymerizable functional groups, PETA can form a highly crosslinked polymer network, thus providing a good mechanical stiffness for the tips.

Moreover, the resulting p(PETA) contains hydroxyl groups (OH-) that absorb water molecules, resulting in a significant swelling effect in water containing environments. This makes the polymer tips become good candidates for detecting levels of humidity and water content, which will be presented in more details in the following chapters.

2.2.2. Self-guiding polymerization method

The polymer microtip is fabricated at the facet of a single-mode optical fiber (SMF) by self-guiding photopolymerization, schematically illustrated in Figure 2.1. Initially, a SMF (Thorlabs SMF-28 with a core diameter of 8.2 μm and cladding diameter of 125 μm, or Thorlabs 780HP with a core diameter of 5 μm and cladding diameter of 125 μm) is carefully cleaned, cleaved and vertically mounted into a fiber holder. The SMF is then connected to a laser source (OXXIUS, with a wavelength of 375 nm) via an optical shutter, a focus lens and a multi-mode fiber (MMF) at one end. Using the MMF with a core diameter of 50 μm allows us to efficiently couple the laser light into the SMF via a fiber connector. The free end of the SMF is gradually inserted into a droplet of PETA mixed with photo-initiator 2,2-dimethoxyl-2-phenylacetophenon (DMPAP) on a horizontal flat substrate. The molecular ratio of DMPAP is equal to 1 % of PETA polymerizable groups. When the power source is turned on, the laser passes through the optical fiber and exposes the photopolymer droplet, thereby triggering a photopolymerization within the droplet. After a given exposure, the fiber end is lifted up out of the photopolymer droplet and gently dipped into ethanol for about 10 s. The unpolymerized polymer is rinsed out by ethanol, resulting in a well-defined polymer tip at the end of the optical fiber. The geometrical shape of the polymer tip is controlled by the exposure dose, while the length of the tip (L) is controlled by the distance between the fiber facet and substrate of the PETA droplet.

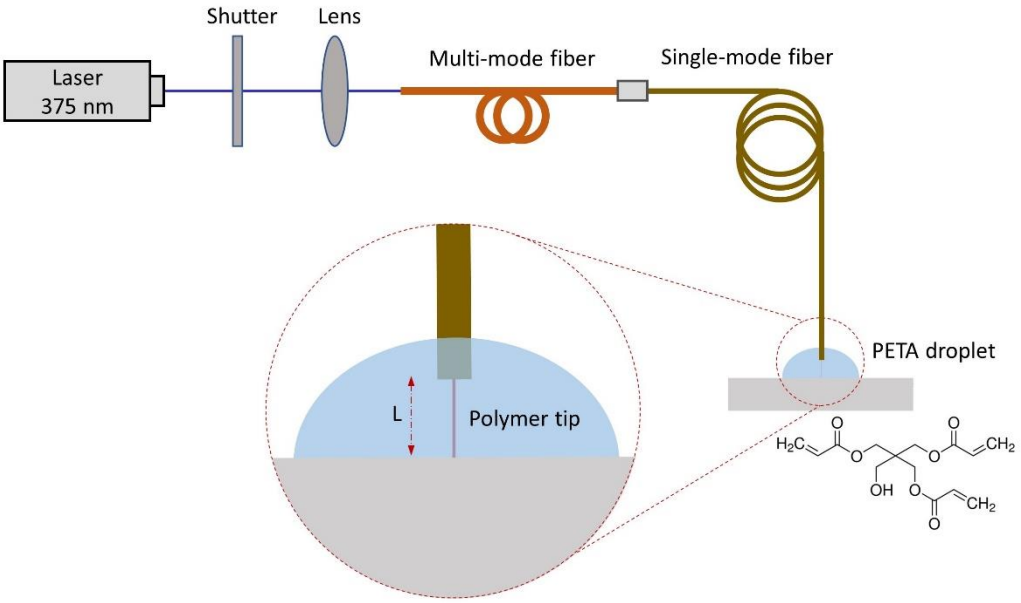

Figure 2. 1. Schematic diagram of the experimental setup for fabrication of a polymer tip at the end of an optical fiber.

2.2.3. Results and discussion

Figure 2.2 shows PETA-based tips fabricated at the end of the SMF-28 fiber by various exposure doses, which correspond the product of the laser power and the exposure time (D = injected laser power × exposure time). It should be noted that the laser power mentioned here is the value measured immediately in front of the SMF, after passing through the shutter, lens and MMF. Initially, we conducted trials using a laser power of 0.5 µW and exposure time of few minutes. Under these conditions, it was not possible to obtain a PETA-based tip due to the power being below the threshold required for the initial activation of polymerization. Subsequently, the laser power was increased to 1.0 µW and a PETA-based tip was obtained in only 0.25 s. The tip has a straight length of up to 100 µm. However, when exceeding 100 µm in length, the tip curves and becomes easily breakable, even during the rinsing step. By further increasing the exposure time, we discovered that an exposure power of 1.0 µW and an exposure time of 0.5 – 1.0 s are optimal to form a straight polymer tip, irrespective of its length. If overexposed by either increasing the laser power and/or the exposure time, the tip presents an enlarge head.

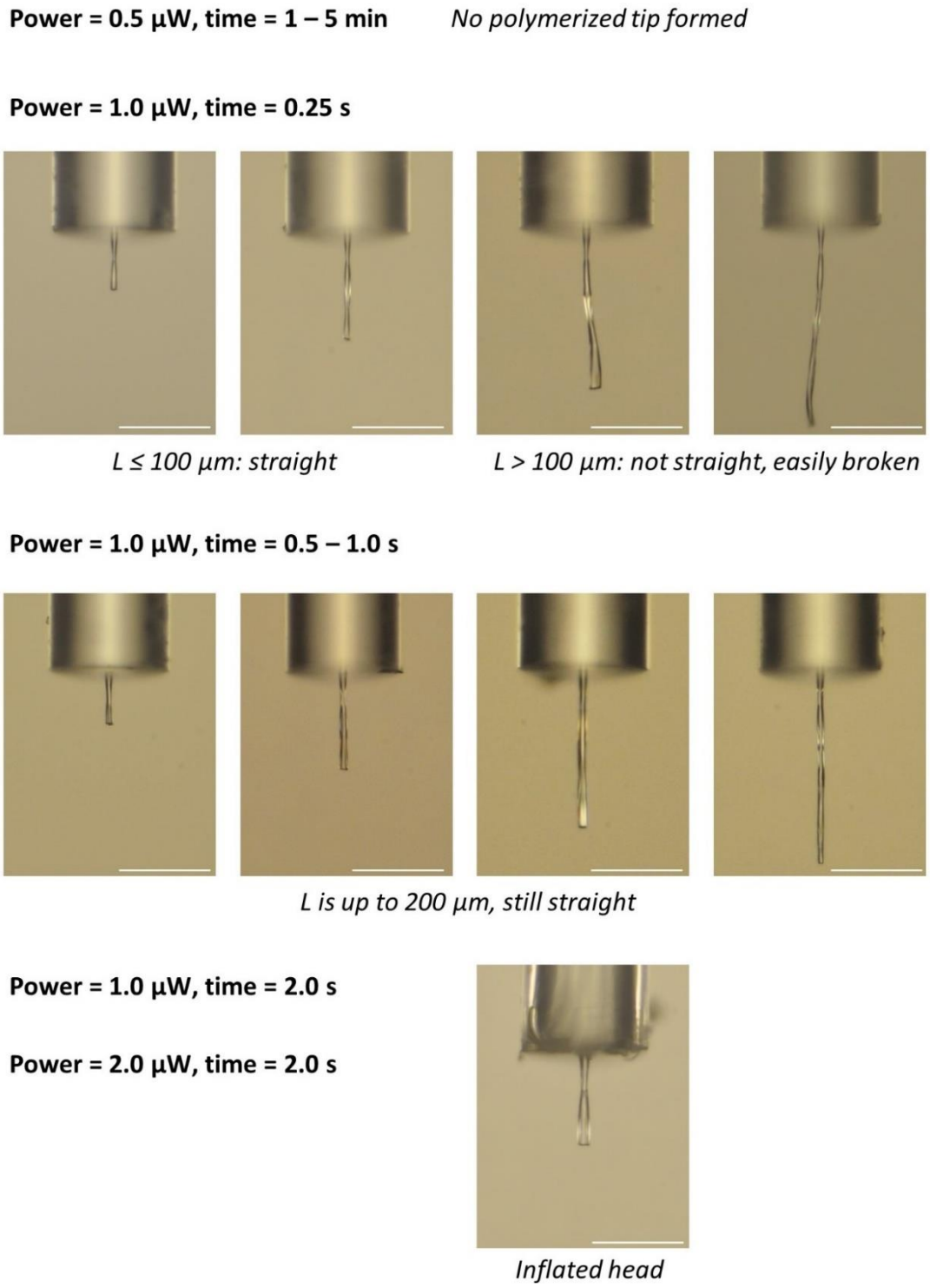

Figure 2. 2. PETA-based tips at the end of SMF-28 obtained by different exposure conditions. The scale bar is 100 µm.

The aforementioned fabrication conditions are also applied to the fabrication of PETA-based tips on the facet of the fiber 780HP, which will be used for Fabry-Perot interferometer characterization in the following chapters.

The SEM images of the PETA-based tips attached on the facet of the fiber 780HP are presented in Figure 2.3. An exposure dose of 1.0 µW laser power and 1.0 s exposure time is optimal to form a polymer tip with a defined and uniform shape, see Figure 2.3(a-b). When underexposed, the polymerization is insufficiently activated, resulting in tips with unstable mechanical strength. In contrast, overexposure by either increasing the laser power and/or the exposure time results in PETA-based tips with an inflated head, see Figure 2.3(c). By adjusting the distance between the fiber facet and the droplet substrate, polymer tips with different micro-scale lengths are obtained. These results demonstrate the simple, rapid and controllable process of producing polymer tips at the end of optical fibers.

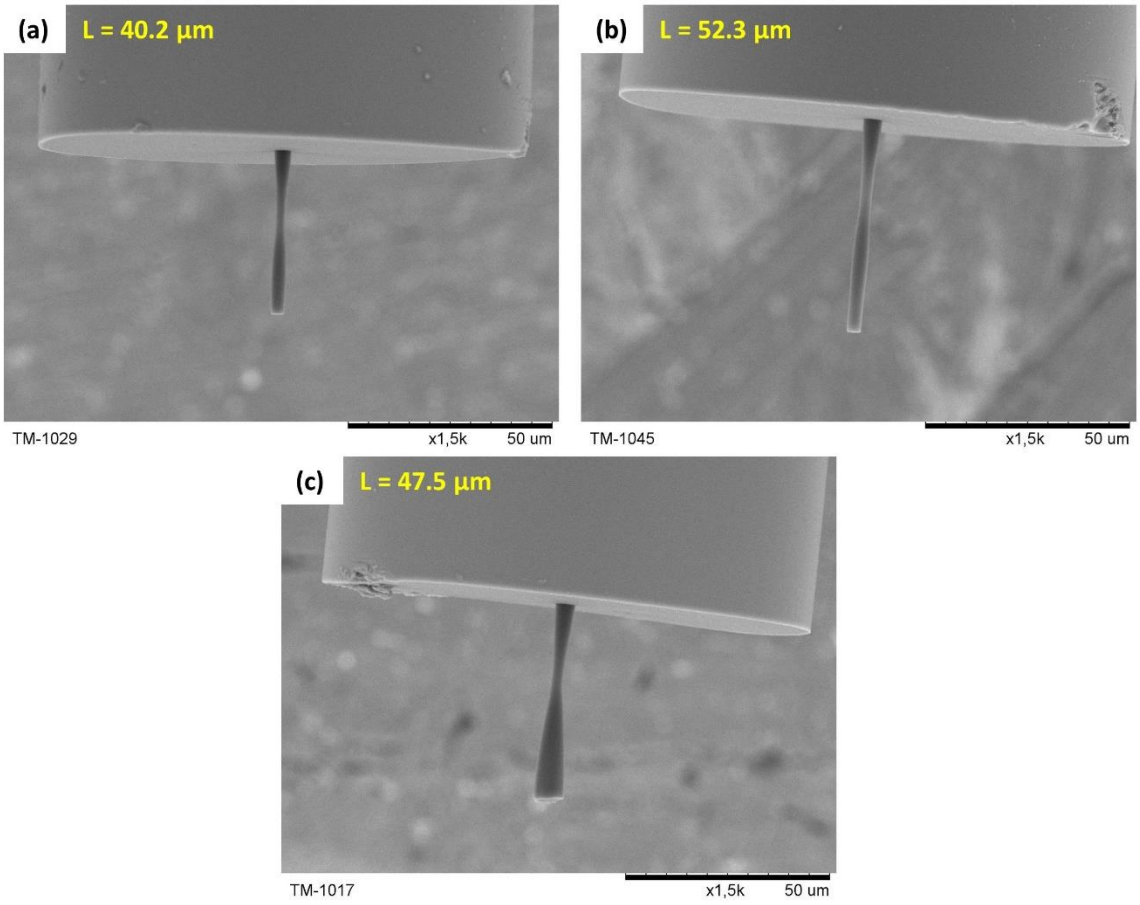

Figure 2. 3. SEM images of PETA-based tips at the end of the 780HP fiber formulated under optimized exposure dose (a-b) and over exposure dose (c).

The aforementioned experimental results demonstrate the successful fabrication of a polymer tip at the end of an optical fiber without any enlargement, even though the laser tends to diverge at the output of the fiber. This is attributed to the self-guiding and self-focusing of the laser within the formulated polymer segment [18]–[22]. Indeed, the refractive index of the PETA droplet gradually increases during the photo-polymerization process. Thus, as soon as the polymer section is polymerized, it immediately acts as an optical waveguide with the polymerized area acting as the core, and the surrounding unpolymerized area as the cladding. The laser then propagates within this waveguide and avoids a diverge effect.

Moreover, exposure of the PETA droplet to intense electromagnetic radiation causes a change in the refractive index of the material, resulting in a self-focusing effect of the light, a non-linear optical process. This effect concentrates the laser at particular points, resulting in a node as experimentally observed in our fabricated tips. These results are consistent with the experimental and simulation data in previous studies [20], [21].

2.3. Dynamic characterization of the p(PETA) tip

2.3.1. Method

To evaluate the quality of the fabricated PETA-based tip, we analyzed the dynamic characteristics of the tip by measuring its resonant frequency. It is worth noting that previously, the through-fiber PETA tip was demonstrated to operate in dynamic mode in a PhD work conducted at the IMS laboratory, University of Bordeaux and the GEC laboratory, University of Compiegne [23]. The resonant frequency of the PETA tip was analyzed by a laser Doppler vibrometer (Polytec MSA 500), which relies on the Doppler effect. This technique measures vibrational velocity and displacement of an object by examining the frequency shift of back-scattered light from the moving object surface. Figure 2.4 displays the working principle and basic setup of the laser Doppler vibrometer. A laser beam, with a wavelength of 633 nm and frequency f_0, is split into two parts by a beam splitter: a reference beam and a test beam. The reference beam, after passing through the Bragg cell that introduces a frequency shift f_b, propagates to the photodetector with a frequency of $f_0 + f_d$. In the meantime, the test beam is directed at the moving object and scattered by the moving surface. The frequency and phase of the backscattered light are now changed depending on

the velocity and displacement of the moving object. In particular, the object motion adds a Doppler shift to the test beam given by $f_d = \frac{2v(t)\cos\propto}{\lambda}$, where v(t) is the velocity of the object, which is a function of time, α is the angle between the laser beam and the velocity vector, and λ is the wavelength of the light. The back-scattered light (with a frequency of $f_0 + f_d$) continues to reach the photodetector and interferes with the reference beam. The superposition of the two beams creates a modulated output signal, revealing the Doppler shift in frequency and thus provides the vibrational velocity and displacement of the test object.

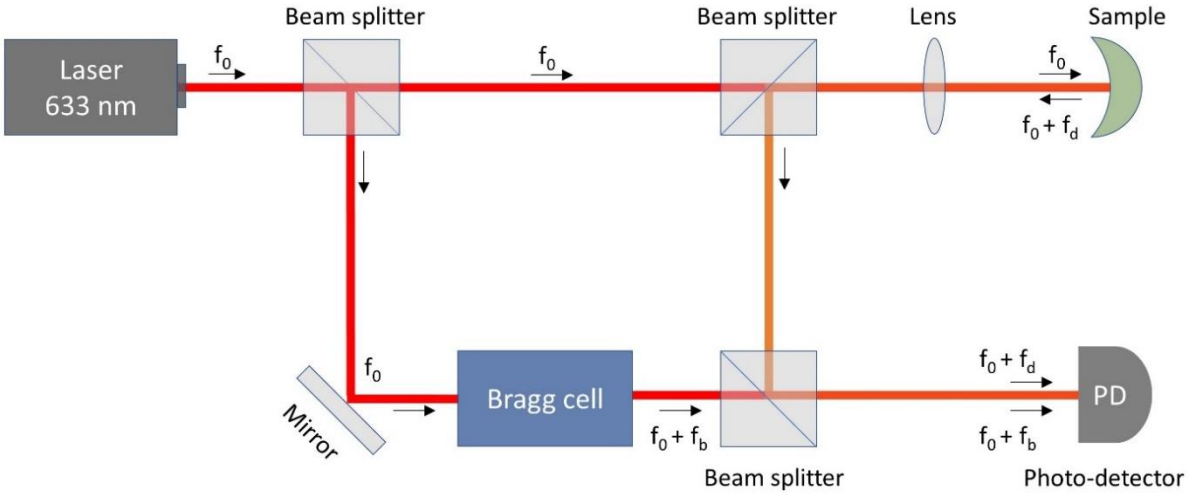

Figure 2. 4. Measurement principle and setup of a laser Doppler vibrometer.

To measure the dynamic characteristics of a device, inducing its dynamic motion is the primary and crucial step. One of the most common techniques is using a piezoelectric actuator element. Previously at IMS laboratory, Bokeloh [23] used a piezo-driven lead zirconate titanate (PZT) to actuate a device which consists of a fiber optic PETA tip attached to a glass substrate using a double-sized adhesive tape. This method requires specific skills and the device response may exhibit spurious resonance modes [24]–[26]. On the other hand, laser excitation has been demonstrated as a promising method to actuate the device motion thanks to its ability to integrate easily and produce clean cantilever resonance peaks in both air and liquid phases [24]–[26].

In this study, the mechanical vibration of the p(PETA) tip is actuated by photo-thermal excitation caused by an intensity-modulated laser diode [24], [26]–[28]. We then recorded the frequency spectrum of the tip using the laser Doppler vibrometer, as schematically shown in

Figure 2.5. The p(PETA) tips used in the dynamic characterizations were fabricated at the end of the optical fiber SMF-28. A 20-nm-thick Au layer is deposited onto one side of the p(PETA) tip by thermal evaporation method. The p(PETA) tip has therefore one half of the lateral surface covered by Au and the other half surface free. Such asymmetry is required for the integrated actuation of the tip. A laser diode with a wavelength of 1310 nm (QPhotonics, QDFBLD-1310-5AX) is transmitted to the p(PETA) tip through an isolator. The intensity of the laser diode is modulated by a laser driver current which is synchronized with a commercial Laser Doppler vibrometer (LDV). A red laser from the LDV is directed to the extremity of the tip and its deflection is then recorded by the LDV itself. Since this LDV laser's output power is constant and small, it does not affect the dynamic response. This work utilizes the photo-thermal excitation, in which the Au layer absorbs the injected laser 1310 nm and converts the light into heat. Due to different thermal expansion coefficient of Au and p(PETA), a thermal stress is generated with the bi-layer tip, making the tip bended. The laser excitation with a modulated intensity results in a vibration of the tip at varying frequencies. This method allows us to determine the resonant frequency of the tip.

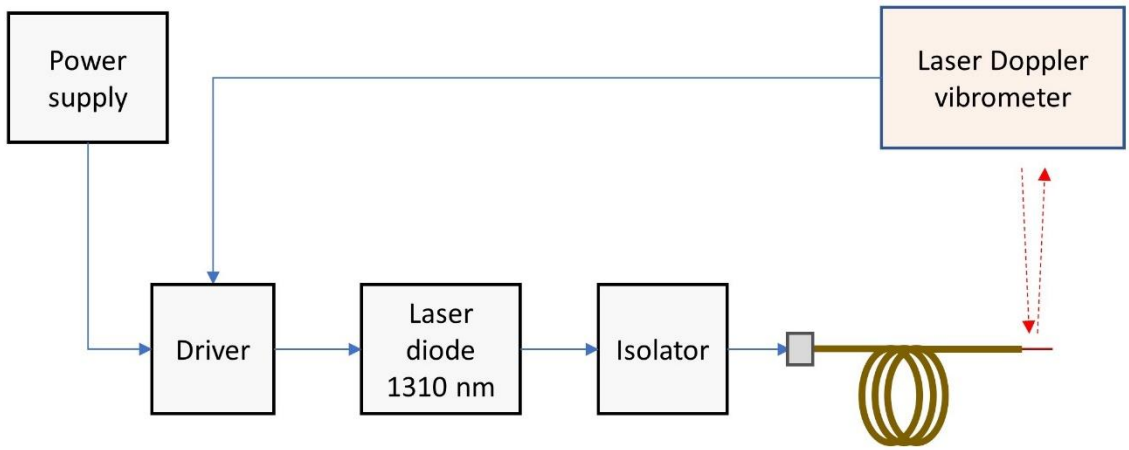

Figure 2. 5. The schematic diagram of the experimental setup for measuring the dynamic response (resonant frequency) of the polymer tip.

2.3.2. Results and discussion

Figure 2.6 shows the first out-of-plane bending resonance mode of a 173.0 µm-long p(PETA) tip that was recorded with an average excitation power of 1.5 mW. The resonant frequency

(f_r) of the tip can be determined by analyzing the maximum magnitude (A) or 90° phase shift. In addition, the quality factor of the tip can be calculated using the equation:

$$Q = \frac{f_r}{\Delta f} \tag{2.1}$$

where f_r is the resonant frequency, Δf is the resonance width or full width at half maximum (FWHM). The p(PETA) tip shows a distinct resonant frequency of 76 kHz and a quality factor of 17. It is worth noting that the spectrum actuated by the laser reveals no additional spurious oscillation modes, indicating that only the first flexural vibrational mode is excited.

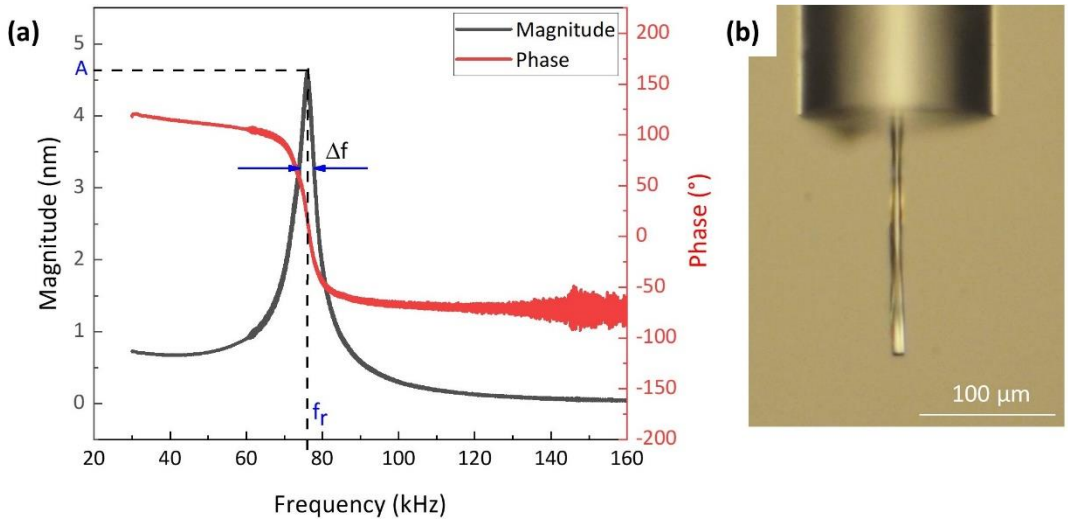

Figure 2. 6. (a) Frequency spectrum of a p(PETA) tip 173.0 µm long which has a microscope image shown in (b).

We also studied the frequency response of another p(PETA) tip of 105.8 µm in length excited by an actuation laser power of 4.6 mW. The results, shown in Figure 2.7, indicate a clear resonant frequency of 155.5 kHz. However, conducting a second measurement with the identical laser power, we obtained another resonant frequency of 159.6 kHz, indicating a 2.6 % difference compared to the first result. We propose that during the measurement, the Au layer absorbs some energy from the actuation laser, which was then converted into heat and transferred to the tip, resulting in a further cross-linking in the PETA chains within the tip. The polymerization of the PETA chain might not have been fully completed during the tip fabrication which takes place during only 1 s. When the tip is further polymerized, it becomes stiffer and achieves a higher Young's modulus. The effective Young's modulus of the Au/ p(PETA) tip is therefore also increased. A correlation between the resonant frequency of a

single clamped beam with a cylindrically cross-section and its Young modulus is described as follows [23], [29], [30]:

$$E = (\frac{4\pi f_r L^2}{\lambda^2 R})^2 \rho \tag{2.2}$$

where E is the tip Young's modulus, f_r is the resonant frequency, L is the tip length, R is the tip radius, ρ is the mass density of the material, λ is the eigenvalue of the resonance mode. For the first out-of-plane resonance mode, λ = 1.875. From Equation (2.2), it is evident that an increase in the Young's modulus leads to a higher resonant frequency of the tip. This explains well our observation presented above. Therefore, to ensure the tip is completely polymerized and exhibits stable properties, it is crucial to conduct a post-polymerization process after the self-guiding polymerization of the tip.

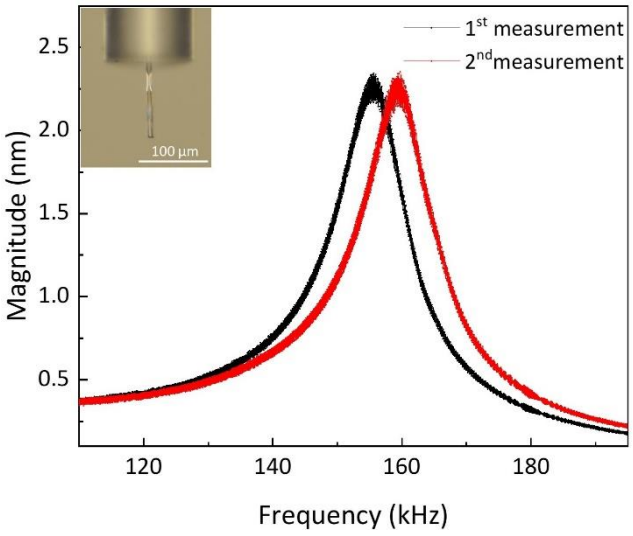

Figure 2. 7. Frequency spectrum of the p(PETA) tip 105.8 µm long in two different measurements. Inset is the microscope image of the tip.

2.4. Post-polymerization of p(PETA) tip

2.4.1 Injecting a UV laser into the tip

As presented in the previous section, the well-defined p(PETA) tip is formed by a self-guiding polymerization using an optimized exposure dose of 1.0 µW laser power and 0.5 – 1.0 s exposure time. However, the polymerization of the PETA chains is not fully completed, consequently causes dynamic properties of the tip inconsistent. Our primary consideration

was to take advantage of the current fabrication setup to reinject a UV laser into the fabricated tip, as schematically shown in Figure 2.8. The laser is used at its maximum power and the power measured in front of the free end of the optical fiber is 40 µW. The experiment is carried out for various periods up to 15 min. Our aim is to determine the optimized periods to fully complete the polymerization process of the PETA chains, which allows the tip to achieve a stable resonant frequency.

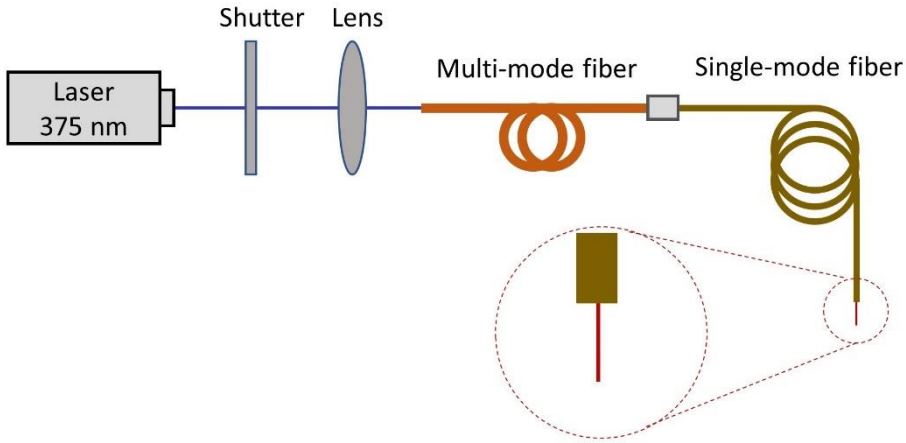

Figure 2. 8. The schematic diagram of the experimental setup for post polymerization of PETA-based tips by injecting a UV laser 375 nm into the tip.

The resonance spectrum of a 103.7-µm-long PETA-based tip is recorded after various post-polymerization periods, as shown in Figure 2.9(a). The excitation laser is set to be 1.65 mW. By plotting the resonant frequency versus the post-polymerization time, we can clearly observe an increase in the resonant frequency with longer post-polymerization times, see Figure 2.9(b). This result indicates that the tip absorbs more energy with increasing post-polymerization time to further complete the cross-linking process within the PETA chains, resulting in a stiffer tip with a higher resonant frequency. However, after 15 min of UV laser irradiation, the tip still exhibits an unstable resonant frequency, implying that this condition is inadequate for the post-polymerization of PETA tip. The laser injection can theoretically continue for a longer duration; however, this method will be time consuming when dealing with numerous devices because we only can perform the post-polymerization on a single tip at one time.

Furthermore, we examined the evolution of the resonant frequency of the obtained PETA tip after post-polymerization (by injecting 40µW-power UV laser for 15 min) in different measurements, in particularly two increase-decrease cycles of the power excitation, see Figure 2.9(c). At a specific power actuation, the f_r of the tip measured in the second cycle is still higher than the one measured in the first cycle. It again indicates that an injection of 40µW-power UV laser into the tip for 15-min is insufficient for its post-polymerization.

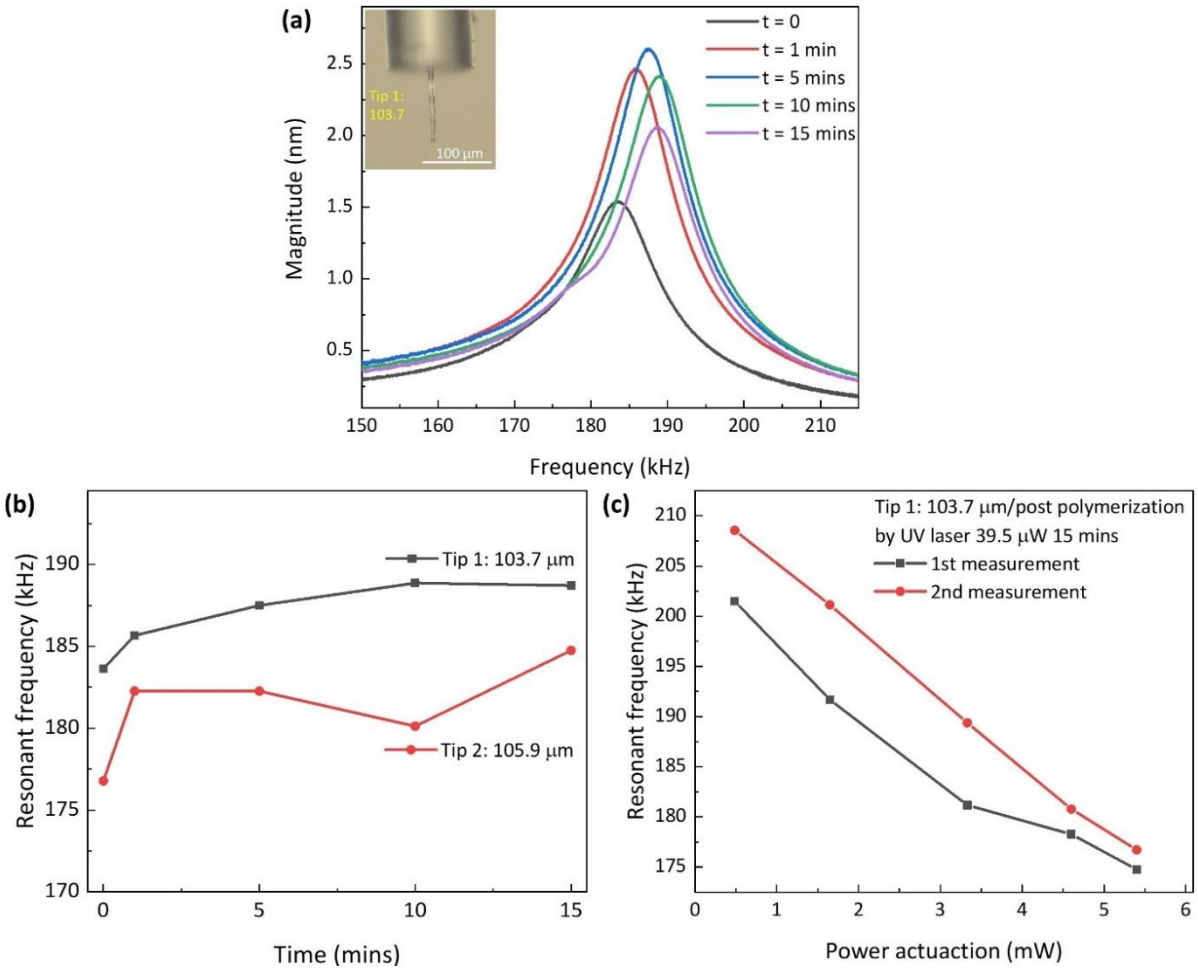

Figure 2. 9. (a) Frequency spectra of the 103.7 µm long tip after being injected with UV laser over different periods of time. Inset is the microscope image of the tip. (b) Evolution of the resonant frequency of PETA tips as a function of the UV laser injection time. The measurements in (a,b) were conducted at an actuation power of 1.65 mW. (c) Evolution of the resonant frequency of the 103.7 µm long tip as a function of the power actuation in different measurements.

2.4.2 Exposing the tip to external UV irradiation

The second method for post-polymerizing the PETA tip is exposing the tip under an external UV lamp. A batch of PETA tips is exposed under a UV lamp (Fisher Scientific – 6 W) with a wavelength of 365 nm inside a glovebox to prevent the influence of oxygen on polymerization, as schematically shown in Figure 2.10. In fact, oxygen is known to interact with initiators and free radicals within the material, subsequently generating peroxy radicals which are incapable of reinitiating a polymerization process [31]. Thus, the post-polymerization needs to be conducted in an oxygen-free environment. The devices are taken out after various exposure times for dynamic measurement.

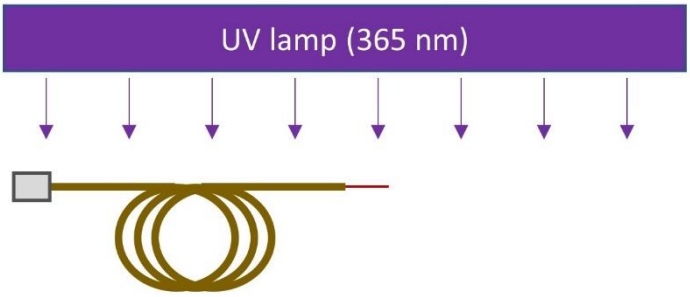

Figure 2. 10. The schematic diagram of the post polymerization of PETA tips under a 365-nm UV lamp.

Figure 2.11(a) shows the frequency spectrum of a 111.6-µm-long tip after various times of post-polymerization. The excitation laser is again fixed to be 1.65 mW. The resonant frequency shifts to a longer value with increasing exposure time. When the resonant frequency is plotted as a function of the post-polymerization time, as in Figure 2.11(b), we can clearly see that the resonant frequency increases by approximately 10 % after exposure from 0 to 3 h. However, if the tip is continuously exposed for 3 to 20 h, the resonant frequency remains unchanged. This behavior is consistently observed for a 115.0 µm-long tip also. These data suggest that a minimum of 3 h exposure of PETA tips under the UV lamp is necessary to complete the polymerization of the PETA chains. However, it should be noted that during measurement, the excitation laser may also contribute to the polymerization of the structure. We assumed that this contribution is much smaller compared to that of the UV lamp as the laser excitation was carried out rapidly.

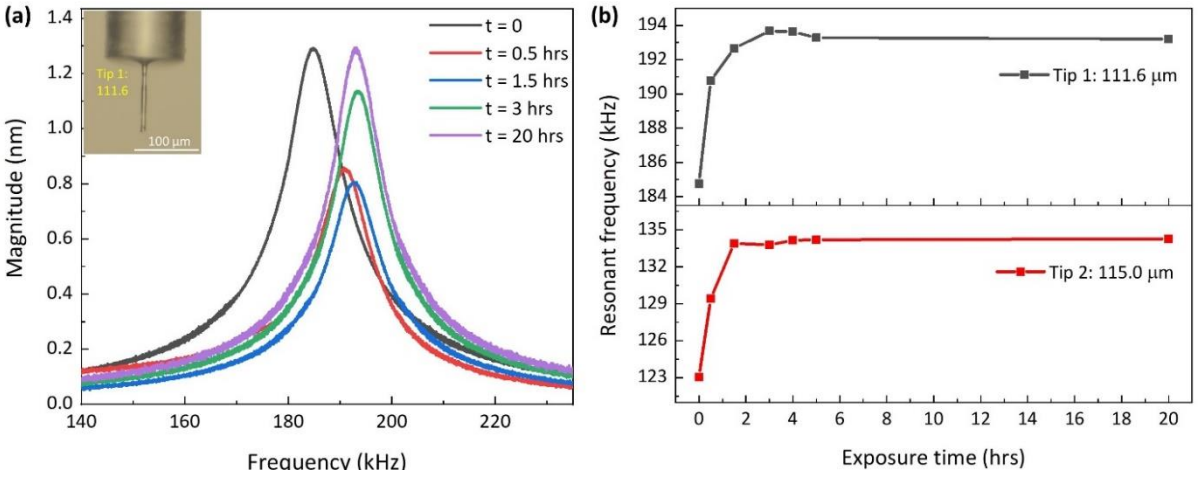

Figure 2. 11. (a) Frequency spectra of 111.6 µm long tip after being exposed under UV lamp over time. Inset is microscope image of the p(PETA) tip. (b) Evolution of the resonant frequency of two tips with the UV lamp exposure time. The measurements were conducted with an actuation power of 1.65 mW.

To confirm the fully complete polymerization of the PETA chains within the tip, we measured the resonant frequency of the tip being UV lamp exposed for 3 h by using different excitation laser powers, see Figure 2.12(a). It is seen that as the excitation power increases from 0.49 to 5.40 mW, the resonant frequency of the tips decreases by 8.45 kHz. Then, as the excitation power decreases from 5.40 to 0.49 mW, the tip shows a reversed shift of 8.66 kHz in the resonant frequency. At a given excitation power, the resonant frequency of the tip is almost identical in different measurements, see Figure 2.12(b). These results confirm the complete polymerization of the polymer chains within the PETA tip after exposure to the UV lamp for 3 h.

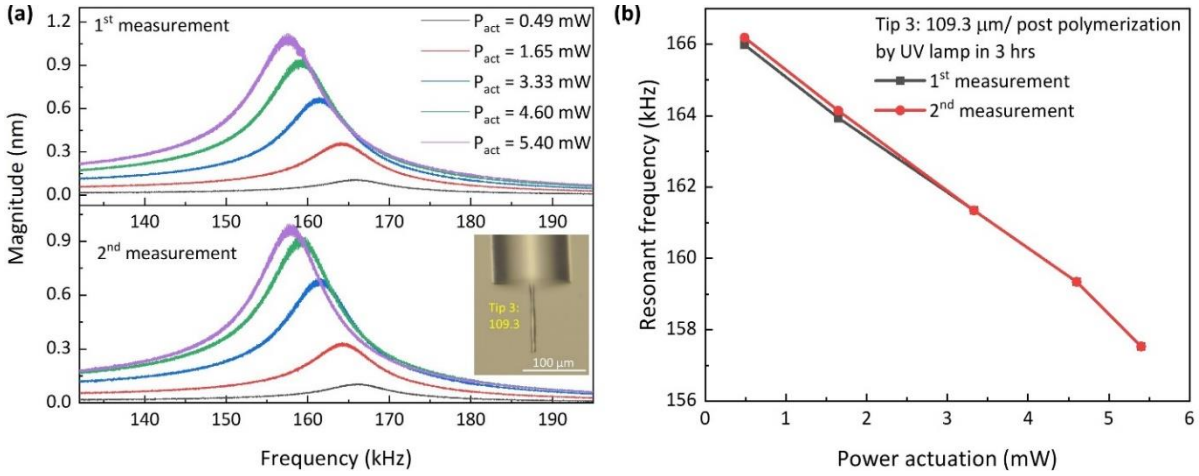

Figure 2. 12. (a). Frequency spectra of the 109.3 µm long tip after post-polymerized under the UV lamp for 3 h, measured with various power actuations. Inset is the microscope image of the tip. (b) Evolution of the resonant frequency of the tip with the power actuation in different measurements.

2.5. Conclusion

In summary, we have presented the successful fabrication of a PETA-based tip attached to the free end of an optical fiber by self-guiding polymerization method. The self-guiding polymerization is actuated by using a OXXIUS laser with a wavelength of 375 nm injected to one end of the optical fiber while the other end of the fiber is stably placed inside a PETA droplet. The geometric shape of the PETA-based tip strongly sensitive to the exposure dose; inefficient dose is not possible to form a tip with stable mechanical strength while overdose causes the tip with enlarged head. The optimal dose is found to be corresponding with an injected laser power of 1.0 µW during an exposure time of 1.0 s. These conditions allow us to obtain p(PETA) tips with straight length and stable mechanical strength. However, the PETA chains are not fully polymerized during the tip fabrication, resulting in a tip with unreproducible dynamic resonant frequency. The formulated p(PETA) tip therefore needs to be post-polymerized under a 365-nm UV lamp for at least 3 h. The final p(PETA) tip exhibits clear and stable dynamic characteristics, validating the optimized fabrication process.

References

[1] Y.-J. Rao, Z.-L. Ran, and Y. Gong, *Fiber-optic Fabry-Perot sensors: an introduction*. in Series in fiber optic sensors. Boca Raton: CRC Press, Taylor & Francis Group, 2017.

[2] B. H. Lee, Y. H. Kim, K. S. Park, J. B. Eom, M. J. Kim, B. S. Rho, and H. Y. Choi, 'Interferometric Fiber Optic Sensors', *Sensors*, vol. 12, no. 3, pp. 2467–2486, Feb. 2012, doi: 10.3390/s120302467.

[3] Woo-Hu Tsai and Chun-Jung Lin, 'A novel structure for the intrinsic Fabry-Perot fiber-optic temperature sensor', *J. Lightwave Technol.*, vol. 19, no. 5, pp. 682–686, May 2001, doi: 10.1109/50.923481.

[4] Y.-J. Rao, M. Deng, D.-W. Duan, and T. Zhu, 'In-line fiber Fabry-Perot refractive-index tip sensor based on endlessly photonic crystal fiber', *Sensors and Actuators A: Physical*, vol. 148, no. 1, pp. 33–38, Nov. 2008, doi: 10.1016/j.sna.2008.06.030.

[5] Y.-J. Rao, M. Deng, D.-W. Duan, X.-C. Yang, T. Zhu, and G.-H. Cheng, 'Micro Fabry-Perot interferometers in silica fibers machined by femtosecond laser', *Opt. Express*, vol. 15, no. 21, p. 14123, 2007, doi: 10.1364/OE.15.014123.

[6] T. Wei, Y. Han, H.-L. Tsai, and H. Xiao, 'Miniaturized fiber inline Fabry-Perot interferometer fabricated with a femtosecond laser', *Opt. Lett.*, vol. 33, no. 6, p. 536, Mar. 2008, doi: 10.1364/OL.33.000536.

[7] T. Wei, Y. Han, Y. Li, H.-L. Tsai, and H. Xiao, 'Temperature-insensitive miniaturized fiber inline Fabry-Perot interferometer for highly sensitive refractive index measurement', *Opt. Express*, vol. 16, no. 8, p. 5764, Apr. 2008, doi: 10.1364/OE.16.005764.

[8] V. R. Machavaram, R. A. Badcock, and G. F. Fernando, 'Fabrication of intrinsic fibre Fabry–Perot sensors in silica fibres using hydrofluoric acid etching', *Sensors and Actuators A: Physical*, vol. 138, no. 1, pp. 248–260, Jul. 2007, doi: 10.1016/j.sna.2007.04.007.

[9] P. A. R. Tafulo, Pedro. A. S. Jorge, J. L. Santos, F. M. Araujo, and O. Frazão, 'Intrinsic Fabry–Pérot Cavity Sensor Based on Etched Multimode Graded Index Fiber for Strain and Temperature Measurement', *IEEE Sensors J.*, vol. 12, no. 1, pp. 8–12, Jan. 2012, doi: 10.1109/JSEN.2011.2107737.

[10] D.-H. Kim, J.-W. Park, H.-K. Kang, C.-S. Hong, and C.-G. Kim, 'Measuring dynamic strain of structures using a gold-deposited extrinsic Fabry Perot interferometer', *Smart Mater. Struct.*, vol. 12, no. 1, pp. 1–5, Feb. 2003, doi: 10.1088/0964-1726/12/1/301.

[11] D. Duan, Y. Rao, and T. Zhu, 'High sensitivity gas refractometer based on all-fiber open-cavity Fabry–Perot interferometer formed by large lateral offset splicing', *J. Opt. Soc. Am. B*, vol. 29, no. 5, p. 912, May 2012, doi: 10.1364/JOSAB.29.000912.

[12] Q. Rong, H. Sun, X. Qiao, J. Zhang, M. Hu, and Z. Feng, 'A miniature fiber-optic temperature sensor based on a Fabry–Perot interferometer', *J. Opt.*, vol. 14, no. 4, p. 045002, Apr. 2012, doi: 10.1088/2040-8978/14/4/045002.

[13] J. S. Santos, I. M. Raimundo, C. M. B. Cordeiro, C. R. Biazoli, C. A. J. Gouveia, and P. A. S. Jorge, 'Characterisation of a Nafion film by optical fibre Fabry–Perot interferometry for humidity sensing', *Sensors and Actuators B: Chemical*, vol. 196, pp. 99–105, Jun. 2014, doi: 10.1016/j.snb.2014.01.101.

[14] X. L. Tan, Y. F. Geng, X. J. Li, Y. L. Deng, Z. Yin, and R. Gao, 'UV-Curable Polymer Microhemisphere-Based Fiber-Optic Fabry–Perot Interferometer for Simultaneous Measurement of Refractive Index and Temperature', *IEEE Photonics J.*, vol. 6, no. 4, pp. 1–8, Aug. 2014, doi: 10.1109/JPHOT.2014.2332460.

[15] T. T. Salunkhe, D. J. Lee, H. K. Lee, H. W. Choi, S. J. Park, and I. T. Kim, 'Enhancing Temperature Sensitivity of the Fabry–Perot Interferometer Sensor with Optimization of the Coating Thickness of Polystyrene', *Sensors*, vol. 20, no. 3, p. 794, Jan. 2020, doi: 10.3390/s20030794.

[16] O. Frazão, P. Caldas, J. L. Santos, P. V. S. Marques, C. Turck, D. J. Lougnot, and O. Soppera, 'Fabry-Perot refractometer based on an end-of-fiber polymer tip', *Opt. Lett.*, vol. 34, no. 16, p. 2474, Aug. 2009, doi: 10.1364/OL.34.002474.

[17] Z. Hu, Y. Chen, J. Tan, Z. Yan, Z. Weng, M. Gusain, Y. Zhan, and L. Xiao, 'A hybrid self-growing polymer microtip for ultracompact and fast fiber humidity sensing', *Sensors and Actuators B: Chemical*, vol. 346, p. 130462, Nov. 2021, doi: 10.1016/j.snb.2021.130462.

[18] A. S. Kewitsch and A. Yariv, 'Self-focusing and self-trapping of optical beams upon photopolymerization', *Opt. Lett.*, vol. 21, no. 1, p. 24, Jan. 1996, doi: 10.1364/OL.21.000024.

[19] C. Ecoffet, R. Bachelot, D. Deloeil, P. Royer, and D. J. Lougnot, 'Integration of polymer elements at the end of optical fibers by free-radical photopolymerization', *Synthetic Metals*, 2001, doi: 10.1016/S0379-6779(01)00415-5.

[20] R. Bachelot, C. Ecoffet, D. Deloeil, P. Royer, and D.-J. Lougnot, 'Integration of micrometer-sized polymer elements at the end of optical fibers by free-radical photopolymerization', *Appl. Opt.*, vol. 40, no. 32, p. 5860, Nov. 2001, doi: 10.1364/AO.40.005860.

[21] M. Hocine, R. Bachelot, C. Ecoffet, N. Fressengeas, P. Royer, and G. Kugel, 'End-of-fiber polymer tip: manufacturing and modeling', *Synthetic Metals*, vol. 127, no. 1–3, pp. 313–318, Mar. 2002, doi: 10.1016/S0379-6779(01)00645-2.

[22] S. Jradi, O. Soppera, D. J. Lougnot, R. Bachelot, and P. Royer, 'Tailoring the geometry of polymer tips on the end of optical fibers via control of physico-chemical parameters', *Optical Materials*, vol. 31, no. 4, pp. 640–646, Feb. 2009, doi: 10.1016/j.optmat.2008.06.021.

[23] F. Bokeloh, 'Development of organic microelectromechanical chemosensors based on fiber optics', 2017. [Online]. Available: https://www.theses.fr/2017COMP2381

[24] D. Kiracofe, K. Kobayashi, A. Labuda, A. Raman, and H. Yamada, 'High efficiency laser photothermal excitation of microcantilever vibrations in air and liquids', *Review of Scientific Instruments*, vol. 82, no. 1, p. 013702, Jan. 2011, doi: 10.1063/1.3518965.

[25] D. R. Evans, P. Tayati, H. An, P. K. Lam, V. S. J. Craig, and T. J. Senden, 'Laser Actuation of Cantilevers for Picometre Amplitude Dynamic Force Microscopy', *Sci Rep*, vol. 4, no. 1, p. 5567, Jul. 2014, doi: 10.1038/srep05567.

[26] Y. Miyahara, H. Griffin, A. Roy-Gobeil, R. Belyansky, H. Bergeron, J. Bustamante, and P. Grutter, 'Optical excitation of atomic force microscopy cantilever for accurate spectroscopic measurements', *EPJ Techn Instrum*, vol. 7, no. 1, p. 2, Dec. 2020, doi: 10.1140/epjti/s40485-020-0053-9.

[27] L.-H. Han and S. Chen, 'Wireless bimorph micro-actuators by pulsed laser heating', *Sensors and Actuators A: Physical*, vol. 121, no. 1, pp. 35–43, May 2005, doi: 10.1016/j.sna.2004.12.012.

[28] H. Yamashita, N. Kodera, A. Miyagi, T. Uchihashi, D. Yamamoto, and T. Ando, 'Tip-sample distance control using photothermal actuation of a small cantilever for high-speed atomic force microscopy', *Review of Scientific Instruments*, vol. 78, no. 8, p. 083702, Aug. 2007, doi: 10.1063/1.2766825.

[29] G. Dubourg, L. Fadel-Taris, I. Dufour, C. Pellet, and C. Ayela, 'Collective fabrication of all-organic microcantilever chips based on a hierarchical combination of shadow-masking

and wafer-bonding processing methods', *J. Micromech. Microeng.*, vol. 21, no. 9, p. 095021, Sep. 2011, doi: 10.1088/0960-1317/21/9/095021.

[30] G. Dubourg, I. Dufour, C. Pellet, and C. Ayela, 'Optimization of the performances of SU-8 organic microcantilever resonators by tuning the viscoelastic properties of the polymer', *Sensors and Actuators B: Chemical*, vol. 169, pp. 320–326, Jul. 2012, doi: 10.1016/j.snb.2012.04.088.

[31] A. K. O'Brien and C. N. Bowman, 'Impact of Oxygen on Photopolymerization Kinetics and Polymer Structure', *Macromolecules*, vol. 39, no. 7, pp. 2501–2506, Apr. 2006, doi: 10.1021/ma051863l.

Chapter 3

Fabry-Perot interferometer-based polymer tip: Working principle and its application for humidity sensing

Abstract. A p(PETA) tip attached to the end of an optical fiber has been successfully formulated by self-guiding polymerization combined with a post-polymerization step, as presented in Chapter 2. In this chapter, we demonstrate that the p(PETA) tip works as a Fabry-Perot interferometer (FPI), resulting in an interferometric signal with clear maximum (peak) and minimum (dip) wavelength positions. More importantly, the FPI signal of the tip is highly sensitive to the variation of the humidity in the air. The tip exhibits a consistent sensitivity of 90pm/%RH, equivalent to a relative sensitivity of 104 ppm/%RH in the humidity range from 30 to 80 %, independent of the tip length. These results are comparable with those of previously reported fiber optic FPI humidity sensors. The humidity sensing principle of the tip is based on the swelling effect of PETA chains, which is resulted from the water absorption of OH- functional groups within the polymer structure. The length and/or the refractive index of the tip is therefore changed with the humidity variation in the air, resulting in a wavelength shift in the FPI signal. The sensing performance of the tip is highly reproducible. Furthermore, cross effect of temperature variations on the FPI signal of the tip is negligible, thereby indicating a great potential for practical sensor devices.

3.1. Introduction

Humidity refers to the presence of water molecules in gaseous environments. Determination of humidity is crucially important for human comfort and technical fields such as structural health monitoring, chemical processing, food storage, and agriculture [1]–[3].

Fiber optic sensors, particularly FPI-based sensors have been widely used for the detection of humidity [4]–[10]. In general, FPI humidity sensors require an optical cavity being functionalized by a hygroscopic material. The hygroscopic material absorbs water molecules from a humid environment, thereby causing the cavity to swell. As a result, the length and refractive index of the cavity change with the environment humidity, leading to a shift in the maximum and minimum wavelength position of the FPI signal. Among the commonly used polymers, polyvinyl alcohol (PVA) is highly sensitive to water and shows a significant swelling effect. Many FPI humidity sensors have been therefore developed by using optical cavity made of PVA [4]–[6]. Aside from PVA, one has also attempted to employ other potential hygroscopic materials for humidity FPI-based sensor, such as chitosan [7] , nafion [8], polymethyl methacrylate [9].

In this chapter, we demonstrate that the p(PETA) tip grown on the facet of an optical fiber works effectively as a FPI humidity sensor. We first theoretically discuss the FPI principle of the tip. We then apply the tip to measure the relative humidity of the air and obtain a constant sensitivity of 90 pm/%RH, which corresponds to a relative sensitivity of 104 ppm/% RH, in the range of relative humidity from 30 to 80 %. This excellent sensing performance is attributed to the strong absorption of water molecules in the humid atmosphere by hydroxyl groups (OH-) within the PETA material, resulting in a significant tip swelling. The changes in the length and/or refractive index of the tip lead to a change in the FPI signal. The sensing performance of the tip is observed to be good reproducible and stable. Moreover, we observe that the FPI signal of the p(PETA) tip is insensitive to temperature change. These properties facilitate the application of p(PETA) tips in practical humidity sensor devices.

3.2. Fabry-Perot interferometer (FPI) based on polymer tip

3.2.1. Working principle and simulated FPI signal of the polymer tip

The fabricated p(PETA) tip has the capability to function as a Fabry-Perot interferometer (FPI). The FPI working principle of a polymer tip attached at the end of an optical fiber is schematically shown in Figure 3.1. When light is injected into the fiber, one part is reflected at the first interface between the fiber core and the polymer tip, while the other part is reflected at the second interface between the polymer tip and the surrounding environment. The Fresnel reflection coefficients at these two interfaces are defined as R_1 and R_2, determined by the following equations:

$$R_1 = \frac{(n_f - n_p)^2}{(n_f + n_p)^2} \tag{3.1}$$

$$R_2 = \frac{(n_p - n_e)^2}{(n_p + n_e)^2} \tag{3.2}$$

where n_f, n_p and n_e are the refractive indices of the core fiber, the p(PETA) tip and the surrounding environment, respectively. In this study, we have $\mathrm{n_f} = 1.456$, (the fiber used in applications is single mode fiber Thorlabs 780HP), $\mathrm{n_p}$ is in the vicinity of 1.483 and $\mathrm{n_e}$ can be changed, depending on the surrounding medium. These refractive indices are close to each other, resulting in small values of R_1 and R_2. We therefore ignore the multiple reflections within the polymer tip and only consider a model for two-beam interference. The resulting interference signal is determined as follows:

$$E_r = \pm E_0 . \sqrt{R_1} + (1 - A_1)(1 - R_1) . E_0 . e^{-2j\beta L} . (1 - \alpha) . \sqrt{R_2} \tag{3.3}$$

where E_0 is the input electric field, A_1 is the transmission loss factor at the reflection interface 1, β is the propagation constant within the polymer tip, and α is the loss factor of the tip. The expression has sign (+) if $n_f > n_p$ and sign (-) if $n_f < n_p$. The normalized intensity $R_{FP}(\lambda)$ of the interferometric pattern is then determined as follows:

$$\begin{aligned} R_{FP} = \left|\frac{E_r}{E_0}\right|^2 = {} & R_1 + (1 - R_1)^2 \cdot (1 - A_1)^2 \cdot (1 - \alpha)^2 \cdot R_2 \\ & \pm 2\sqrt{R_1 R_2}(1 - A_1)(1 - R_1)(1 - \alpha) \cos\left(\frac{4\pi n_p L}{\lambda}\right) \end{aligned} \tag{3.4}$$

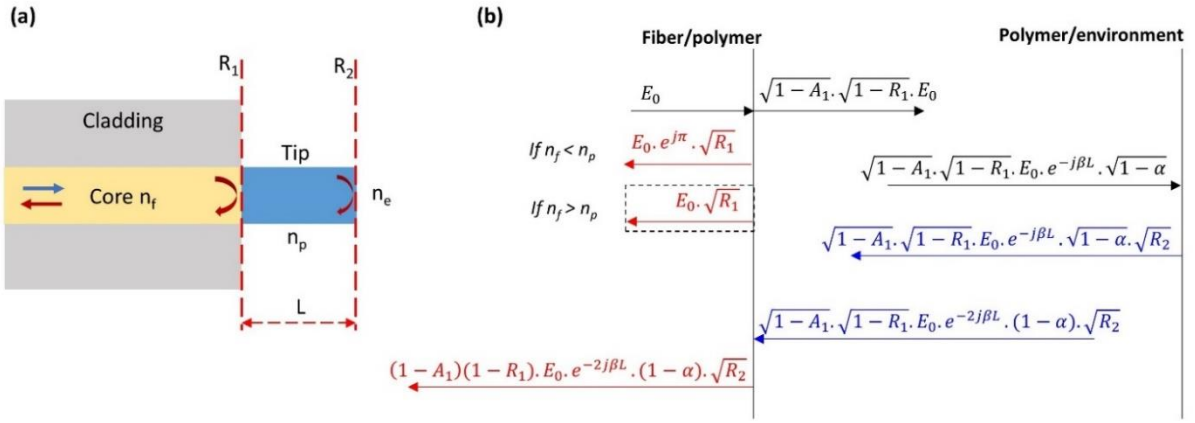

Figure 3. 1. (a) Schematic diagram of the polymer tip working as a Fabry-Perot cavity with two reflecting surfaces R_1 and R_2. (b) The electric field amplitudes of the incident, transmitted and reflected light inside the polymer tip.

It is seen that the interferometric signal depends on the phase difference ($\frac{4\pi n_p L}{\lambda}$) of the two reflected beams which is determined by the refractive index and length of the tip. When the phase difference satisfies the condition $n_p \frac{4\pi nL}{\lambda_{min}} = 2m\pi$ (where m is an integer), the corresponding dip wavelength can be achieved with:

$$\lambda_{min} = \frac{2n_p L}{m} \tag{3.5}$$

Generally, the interference pattern depends on the length and refractive index of the cavity and the refractive index of the surrounding environment. Interferometric patterns of a polymer tip with different lengths or refractive indices are simulated and shown in Figure 3.2. For simplification, all the losses are neglected and the input electric field is set to be constant over the whole range of wavelengths. It can be seen that the interference pattern shows a visible red shift (towards higher wavelength) as the length of the tip increases (Figure 3.2(a)) and shows a visible blue shift (towards shorter wavelength) as the refractive index of polymer tip decreases (Figure 3.2(b)).

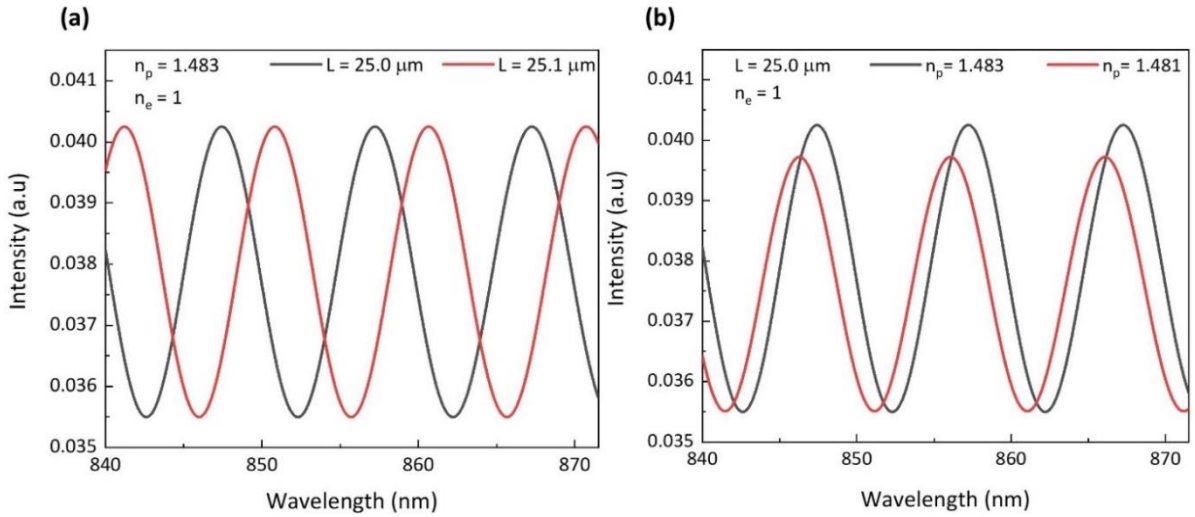

Figure 3. 2. Simulated FPI signals of the polymer tip with (a) different lengths (L) and (b) different refractive indices (n_p) in air.

Moreover, the interference pattern of a polymer tip also depends on the refractive index (n_e) of the surrounding medium, as shown in Figure 3.3. The wavelength positions of the maximum and minimum intensities are unchanged, whereas the signal intensity decreases with the increase of n_e. The difference between the maximum and minimum intensity ($I_{max} - I_{min}$) decreases linearly as the external refractive index increases, as simulated in Figure 3.3(b). The refractive index of fluidic media is often directly related to the concentration of the component materials. Therefore, the FPI signal of a polymer tip dipped inside a solution is sensitive to the solution concentration.

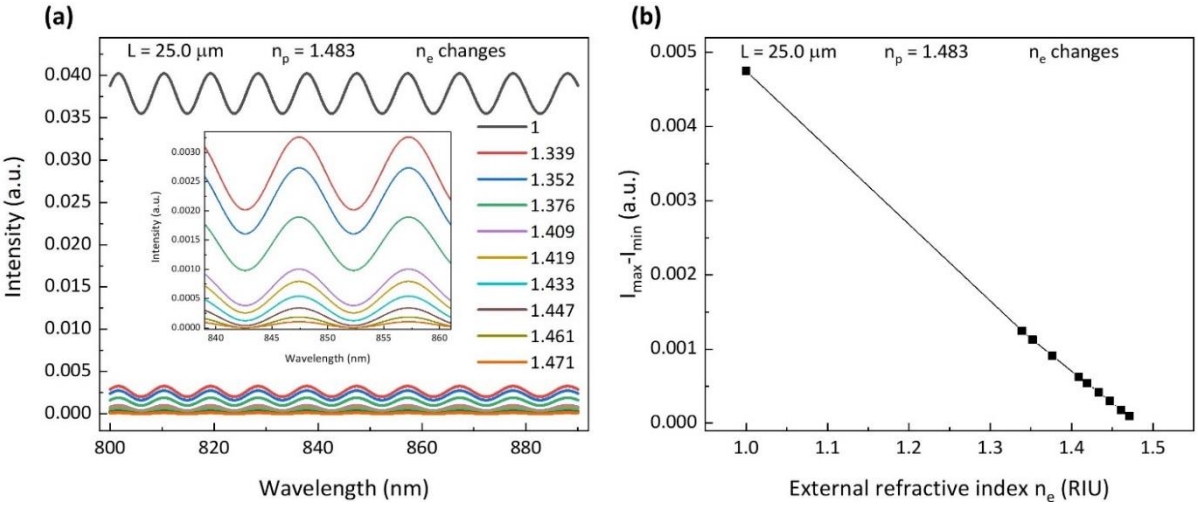

Figure 3. 3. Simulated (a) FPI signal and (b) $I_{max} - I_{min}$ of the polymer tip in different surrounding environments (n_e).

In a nutshell, the variation in temperature, humidity, and material concentration of the surrounding medium will result in a change in the length and refractive index of the polymer tip, consequently affecting its FPI signal. By measuring the changes in the FPI signal of the polymer tip, one can thus detect the changes in these environment parameters.

3.2.2. Setup for recording FPI signal of the p(PETA) tip

To record the FPI signal from the polymer tip attached to the end of an optical fiber, we used a home-made setup, as schematically shown in Figure 3.4. This setup consists of a superluminescent diode (SLED, Qphotonics, QSDM-860-8B, wavelength ranging from 800 to 890 nm, maximum output power of 8mW), an isolator (PMoptics), a fiber coupler (Thorlabs, TW850R5A2), a spectrometer (Ocean Optics, HR2000+, wavelength range of 200-1100 nm and resolution of 0.4 nm). The emitted light from the SLED travels through the isolator and fiber coupler via port (1) and (3) before reaching the polymer tip. The interferometric reflected light induced by the polymer tip travels through the fiber coupler via port (3) and (2) and is subsequently recorded by the spectrometer connected to a computer. The use of an isolator ensures that the reflected light cannot reach the light source, thus preventing instabilities and damage to the source. It is important to mention that during the measurements, the characterization setup is kept to be well fixed and stable to prevent the impact of polarization sensitivity of the fiber on the FPI signal.

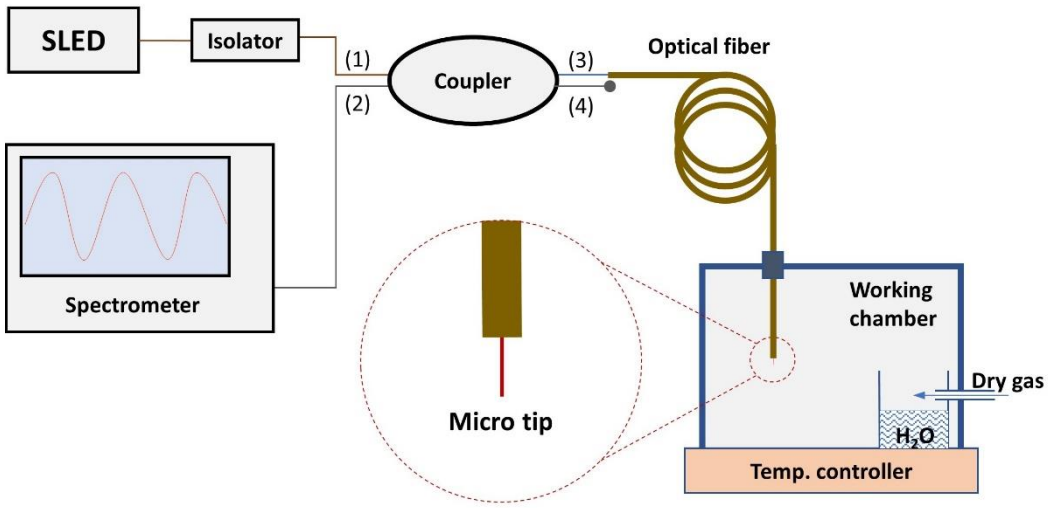

Figure 3. 4. The schematic diagram of the experimental setup for measuring the FPI signal from the polymer tip under different humidity levels.

3.2.3. FPI signal of the p(PETA) tip

The FPI signal produced from polymer tips of different lengths formulated under optimized exposure doses (injected laser power = 1.0 µW and exposure time = 0.5 – 1.0 s) are shown in Figure 3.5. It should be noted that the tips were treated with a post-polymerization under the UV 365-nm lamp to achieve a complete polymerization of the PETA chains, as shown in chapter 2. Their FPI signals were then recorded under identical conditions with a SLED power injected to the fiber of 2.0 mW and the integration time of the spectrometer of 5.0 ms. It is seen that all the tips exhibit a clear FPI signal with highly visible peak and dip positions. When the length of the tip increases, the free spectral range of the FPI (the distance between the two consecutive peaks) decreases. This experimental observation is well consistent with the simulated data (Figure 3.5(c, f, i)).

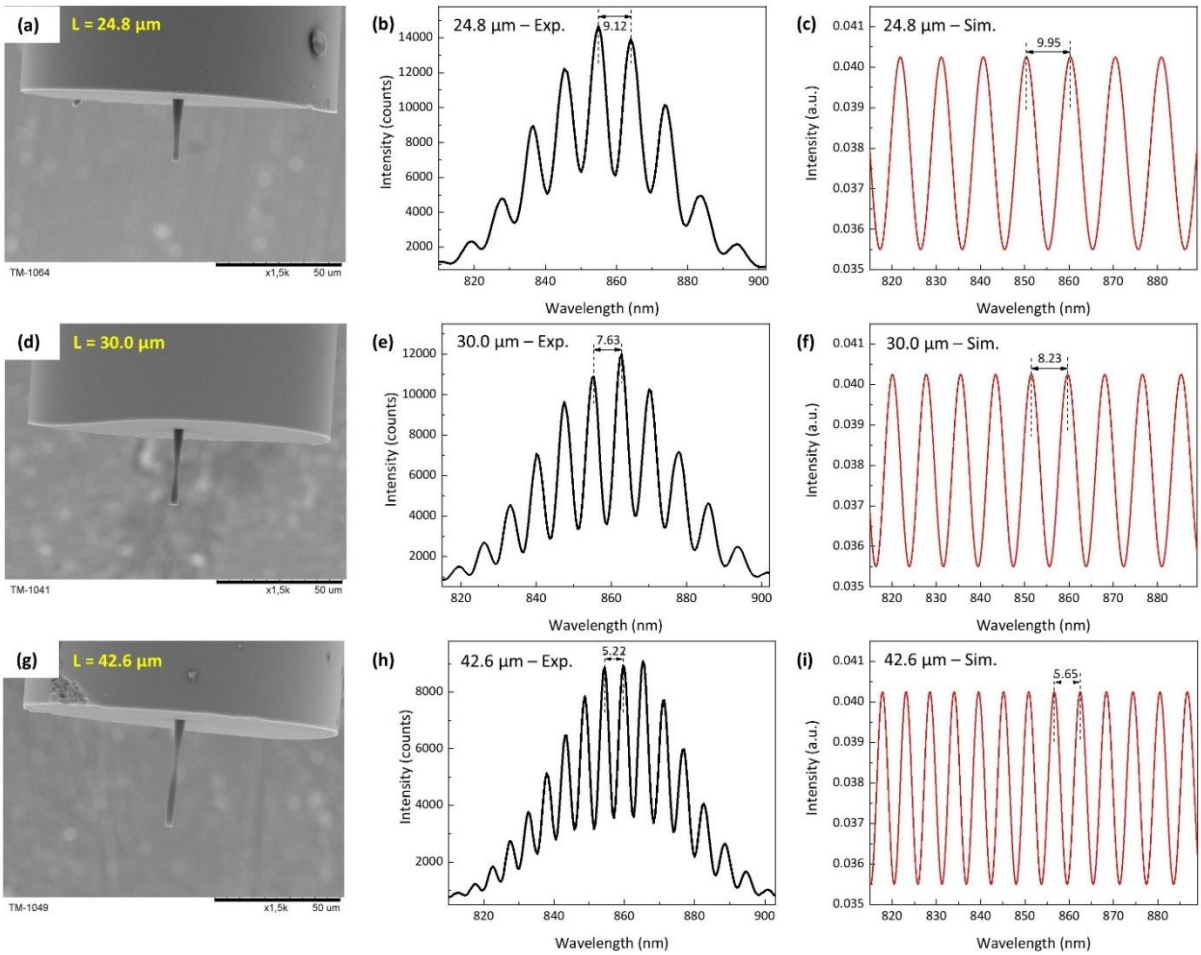

Figure 3. 5. (a, d, g) SEM images of p(PETA) tips formed under a sufficient exposure and (b, e, h) their corresponding FPI signals. (c, f, i) Simulated FPI signal of the polymer tips (n_p = 1.483) in the air.

To observe the effect of the geometric form of the tip on the FPI signal, we study the FPI signals of the tips formulated under an over exposure (injected laser power = 2.0 µW and exposure time = 1.0 – 2.0 s), see Figure 3.6. Compared to the FPI signal of the optimized tips previously shown in Figure 3.5, the FPI signals of the tips fabricated under an over dose exposure display significantly less intensity and contrast. This problem can be attributed to the expanded head of the over-exposure tip, which could decrease the guidance of the light propagating within the tip. Therefore, one needs to carefully optimize the shape of the polymer tip by controlling the exposure dose to obtain a clear and high contrast FPI signal. To further increase the FPI intensity and contrast, one can deposit a thin layer of Au or Ag on the free end of the polymer cavity to attain high reflectivity [11]–[13]. Another way is to fabricate a hybrid tip consisting of a polymer tip grown on a UV cured polymer film covered on an optical

fiber [10]. These both methods however are rather complicated. In this work, the p(PETA) tip with optimized fabrication process already exhibits a clear FPI signal with sufficient contrast for further application studies.

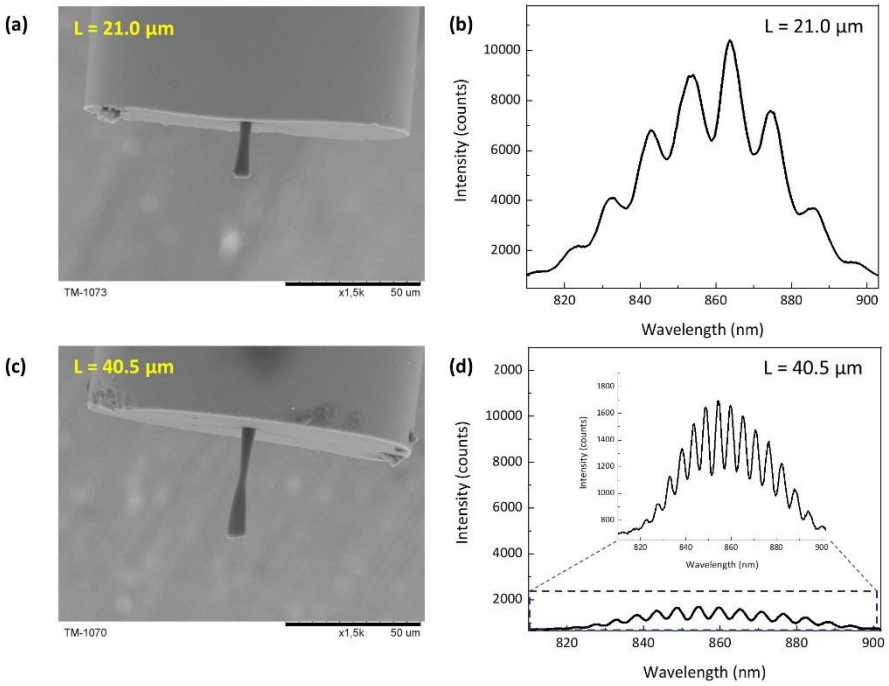

Figure 3. 6. (a, c) SEM images of p(PETA) tips formed under over exposure and (b, d) their corresponding FPI signals.

3.3. FPI-based polymer tip for humidity sensing

3.3.1. Experimental method

Humidity sensing tests

For humidity sensing tests, the polymer tip was placed in a sealed chamber (Surface Measurement Systems, SMS VGI-2000M) where the relative humidity was controlled by a flow of dry N_2 gas passing over a batch of water while the temperature of the chamber was constantly maintained at 23 ± 1 °C. The FPI signal from the tip was recorded by a home-made setup in which the spectrometer collected the reflected light from the tip upon being injected with a broad band source, as mentioned in Section 3.2.2. The interference signal from the tip was monitored as the relative humidity changes (Figure 3.4).

Temperature sensing tests

In practical sensor applications, a change in relative humidity is often accompanied by a change in temperature, that can yield inaccurate measurement outcomes. Therefore, we need to study the impact of temperature variations on the FPI signal of the p(PETA) tip. For this purpose, the polymer tip was positioned in a sealed chamber on top of a hot plate, similar to the setup presented in section 3.2.2. However, a constant flow of dry N_2 gas was directly introduced into the chamber to so that the relative humidity inside the chamber was always maintained at below 2 %. The temperature inside the chamber was varied by the hot plate underneath and calibrated by using a commercially available temperature sensor. The FPI signal of the tip was recorded as a function of the chamber temperature.

3.3.2. Sensitivity of FPI-based p(PETA) tip for humidity sensor

PETA-based tips with different lengths are studied in the relative humidity ranging from 30 to 80 %RH with a step of 10 %RH. As shown in Figure 3.7, the FPI signals of all the tips shift towards longer wavelength with increasing the relative humidity of the chamber. Specifically, the FPI pattern of a 19.7 μm tip consistently shifts by 0.86 nm for every 10% change in RH,

resulting in a total red shift of 4.29 nm as humidity increases from 30 to 80 %. The FPI signal of a 26.9 µm tip exhibits a red shift of 3.99 nm in the same range of relative humidity.

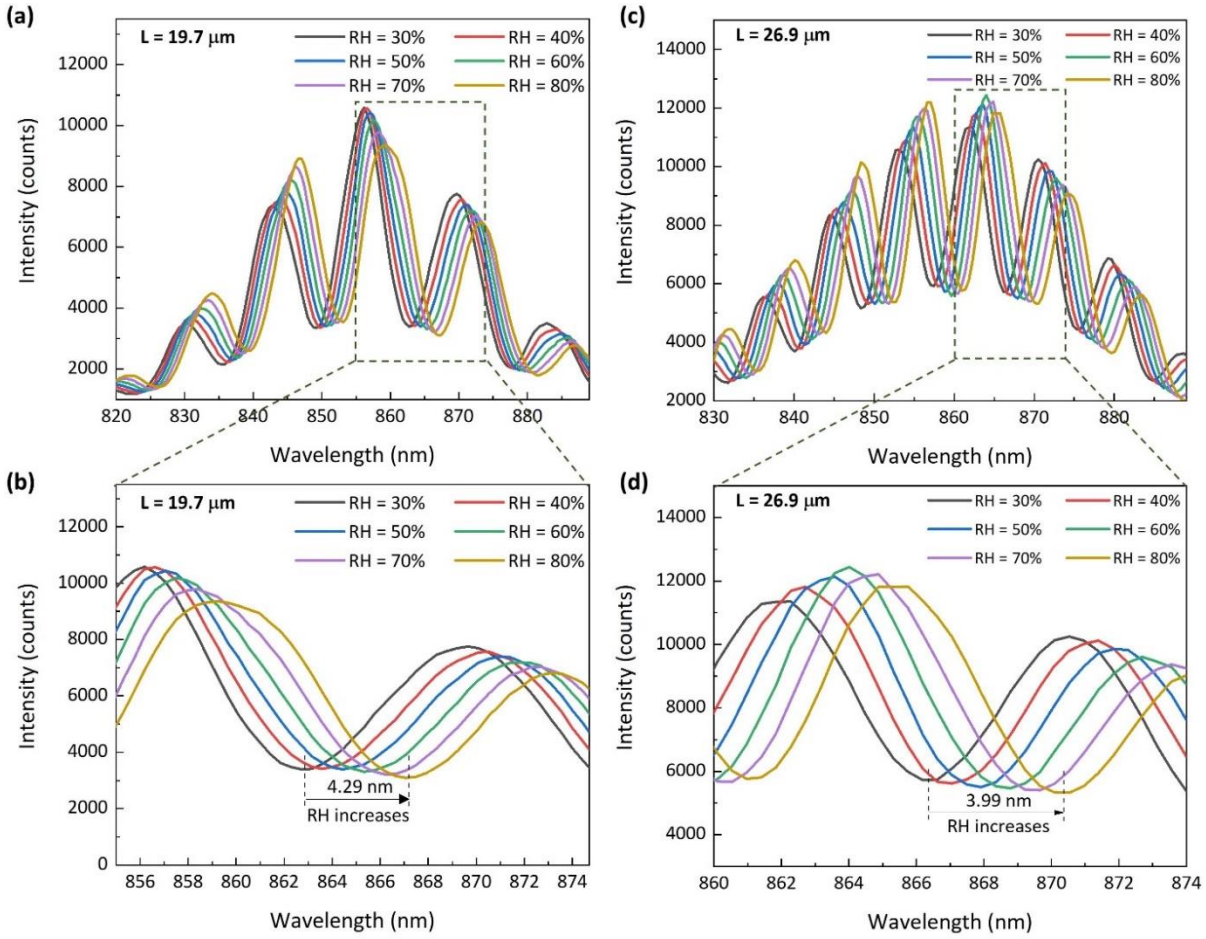

Figure 3. 7. FPI spectra of the p(PETA) tip (a-b) 19.7 µm long and (c-d) 26.9 µm long at various relative humidity values.

The dip-wavelength positions of the FPI spectrum of the tip follow a linear dependence on the relative humidity, see Figure 3.8(a). This dependence allows us to extrapolate the sensitivity of the tips. The tips with a length of 19.7, 26.9, and 31.4 µm exhibit a sensitivity of 90, 80, and 80 pm/%RH, respectively. The difference in the sensitivity of the tips may result from the difference in the wavelength dip position being analyzed. Therefore, we plotted the relative change of dip wavelength ($\Delta\lambda/\lambda$) of the tips as a function of humidity, as shown in Figure 3.8(b). It is clear that the response of the polymer tips to humidity sensing is practically independent of the tip length, allowing to produce easily reproducible and reliable sensors.

Furthermore, based on the fit of Figure 3.8(b), we can estimate the relative sensitivity ($\frac{d\lambda}{\lambda dH}$) of our sensors to be approximately 104 ppm/%RH. Compared to FPI-based sensors reported in previous studies (see Table 3.1), our sensor shows a state-of-the-art relative sensitivity, except for those in [6], [10].

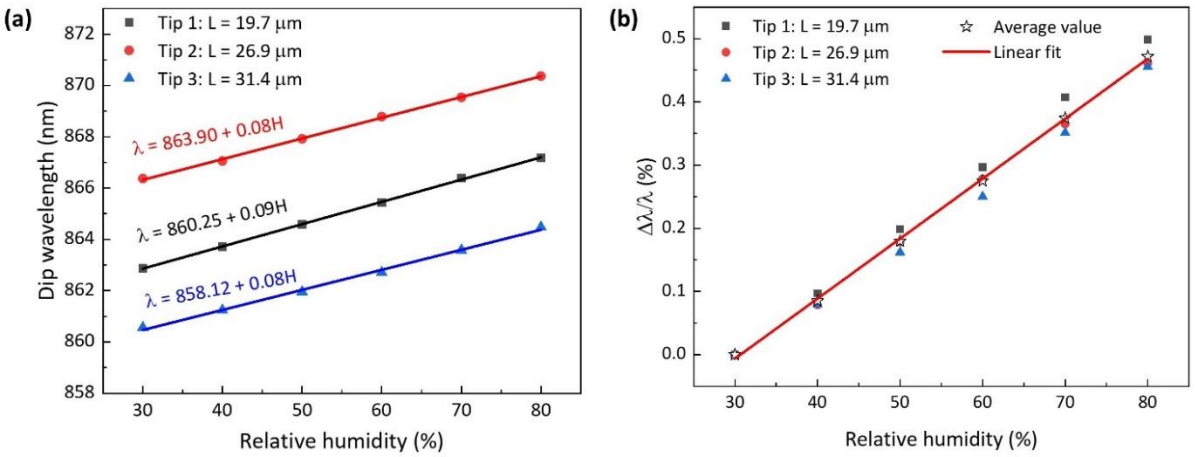

Figure 3. 8. (a) The dip wavelength position and (b) the relative change of the dip-wavelength position of different tips as a function of relative humidity.

Table 3.1. Comparison of sensing performance of some fiber optic FPI humidity sensors available in the literature.

Configuration/ Material	Fabrication method	Relative humidity sensitivity $\frac{d\lambda}{\lambda dH}$ (ppm/%RH)	Range (% RH)	Ref
Thin film chitosan-coated air cavity	Splicing fibers, dip coating	84.27	20 – 95	[7]
Air cavity with PVA coating	Splicing fibers, chemical etching, coating	14.85	30 – 90	[4]
Air cavity with graphene quantum dot/PVA cavity	Splicing fibers, dip coating	74.30	13.47 – 81.34	[5]
NOA61 thin film with micro-tip (eosin Y, MDEA and PETA)	Dip coating	129.69	30 – 90	[10]
Cavity filled with PVA	Splicing fibers, drawing-curing	158.79	46 – 75	[6]
PETA micro-tip	Self-guiding polymerization	104.30	30 – 80	This work

It is noted that we have only studied the wavelength shift of the FPI signal in the humidity sensing tests. We have not considered the change in the FPI intensity. In principle, one can expect that when the humidity changes, the refractive index of the surrounding environment also changes, resulting in a variation in the FPI intensity. However, the change of the refractive index of the air due to a humidity variation is very small, in the order of 10^{-4} - 10^{-5} [14]–[16]. Therefore, we assume that the refractive index of the air is constant during the humidity test, and consequently has no effect on the FPI signal intensity. Indeed, it is observed that the intensity of the FPI peaks clearly changes with varying humidity values, as shown in

Figure 3.7. This change simply results from the non-uniformity of the intensity profile of the SLED source. The intensity profile of the incident SLED light follows a Gaussian function of wavelength, so the intensity of the reflected signal also depends on the wavelength position. To accurately determine the actual effect of environment humidity on the FPI signal intensity, one needs to use a broad-band light source with a flat intensity-wavelength profile.

3.3.3. Humidity sensing principle of p(PETA) tip

The shift in the FPI signal of the tip with variation of the environment humidity can be understood by considering the strong water absorption capability of PETA polymer. The available hydroxyl functional groups (OH-) of p(PETA) can form hydrogen bonds with the surrounding water molecules, resulting in polymer swelling and a consequent expanded change in the tip length. In addition, the refractive index of the polymer tip could also be influenced by the presence of water molecules into the polymer. Therefore, the shift of the FPI spectrum with relative humidity is concurrently attributed to the change of the length and the refractive index of the tip. From Equation (3.5), the shift of the FPI fringe induced by the change of environment humidity can be deduced as following:

$$\frac{d\lambda}{dH} = \lambda\left(\frac{1}{L}\frac{dL}{dH} + \frac{1}{n_{eff}}\frac{dn_{eff}}{dH}\right) \tag{3.6}$$

The first term indicates the effect of the change of the length while the second term denotes the effect of the change of the refractive index of the tip. When the relative humidity increases, the length of the tip increases due to the swelling effect, then one has $dL/dH > 0$. This means the tip shows a red shift in its FPI signal with increasing humidity. However, the absorption of water reduces the effective refractive index of the polymer because the refractive index of water (1.339) is lower than the one of PETA (1.483). This means $dn_{eff}/dH < 0$ with increasing relative humidity and subsequently a blue shift should be observed in the FPI spectrum. The red shift caused by the increase of the tip length and the blue shift caused by the decrease of the tip refractive index compete to each other, resulting in a final effective shift of the FPI pattern. Based on the experimental results where the effective shift is towards the longer wavelength as observed in Figure 3.7, we can conclude that the effect caused by the change of the tip length is much more predominant than the

effect caused by the change of the tip refractive index. Thus, the polymer tip-based FPI sensor proposed here is mechanically sensitive to the water content of the environment.

3.3.4. Repeatability of the FPI signal of the p(PETA) tip

To evaluate the repeatability of the FPI signal of the tip, we investigated its signal evolution for two cycles of increasing and decreasing relative humidity, see Figure 3.9. The FPI spectrum of the 31.4 µm tip shows a red shift of 3.93 nm upon increasing relative humidity from 30 to 80 %. Following the decrease of relative humidity from 80 to 30 %, the tip shows a reversible blue shift of precisely 3.93 nm. Moreover, the dip-wavelength position of the interference spectra remains consistent at a specific humidity value, irrespective of the evolution trend of relative humidity, see Figure 3.9(c). These data indicate the excellent sensing repeatability of the p(PETA) tip.

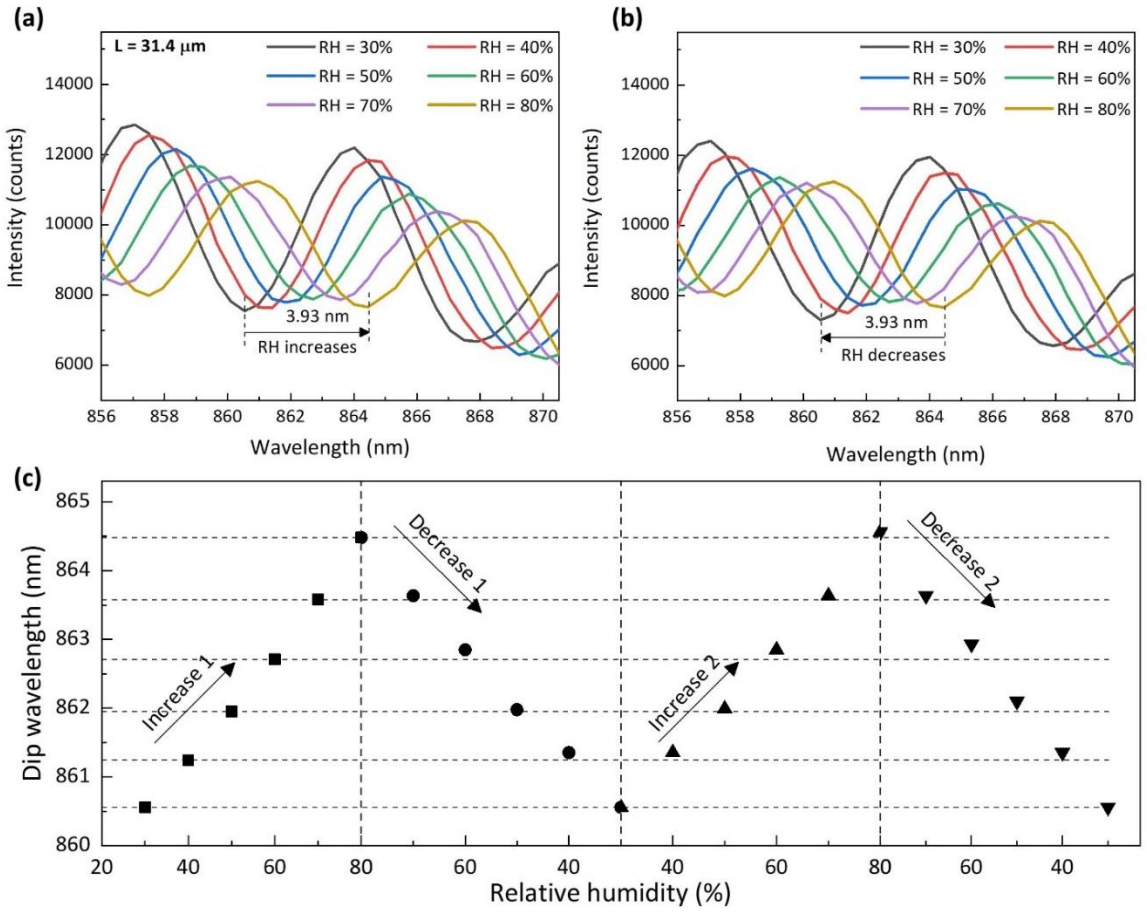

Figure 3. 9. The FPI spectra of the p(PETA) tip 31.4 µm long in the process of (a) increasing RH and (b) decreasing RH. (c) The dip wavelength positions at given relative humidity values during 2 increasing-decreasing cycles of humidity.

3.3.5. Stability of the FPI signal of the p(PETA) tip

In addition to the evaluation of the sensing sensitivity and reproducibility, we also investigated the sensing stability of the p(PETA) tips by monitoring their FPI spectra at specific given relative humidity levels over a period of time. The interference spectra of a tip of 46.7 µm long at relative humidity levels of 25, 50 and 80 % stay unchanged for 90 min of testing, as shown in Figure 3.10. These results confirm that the p(PETA) tip performance is well stable over time.

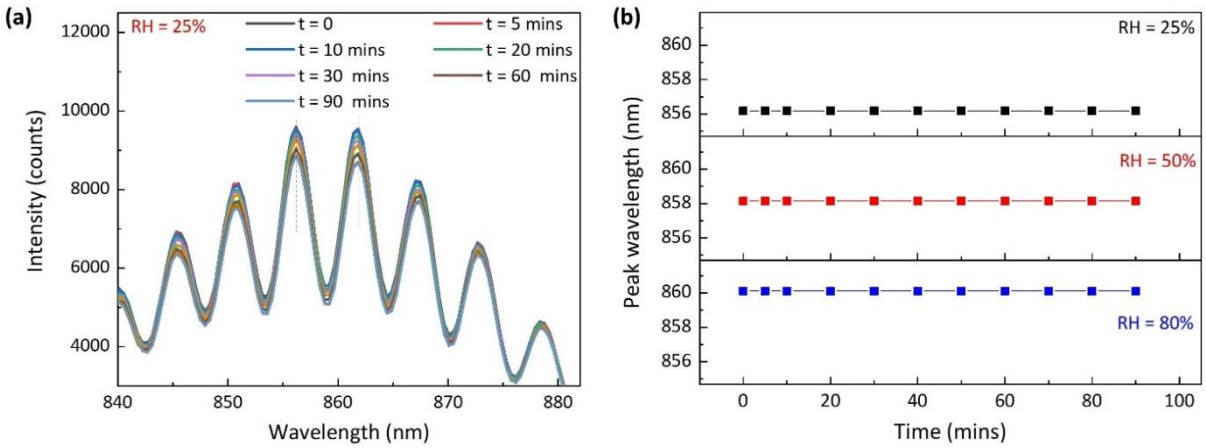

Figure 3. 10. (a) FPI spectra of a p(PETA) tip over time at relative humidity = 25 %. (b) Dip wavelength positions of the FPI of the tip measured over time at three different relative humidity values. The measurements were conducted at room temperature.

3.3.6. Effect of temperature on the FPI signal of the tip

In practical applications, a change in relative humidity is often accompanied by a change in temperature [17], [18]. The temperature change might have some cross effects on the FPI signal of the sensor, consequently lead to inaccurate measurement results. We therefore investigated the effect of temperature variations on the FPI signal of the p(PETA) tip. The p(PETA) tip is placed in a working chamber where the temperature can be varied. To maintain the air inside the chamber at a low relative humidity (RH < 2 %), we introduced a constant flow of dry N_2 gas. The FPI signal of the tip is then recorded at different temperatures, see Figure 3.11. One can see that the tips consistently show their FPI spectra almost unchanged over a temperature range from 23 to 70 °C.

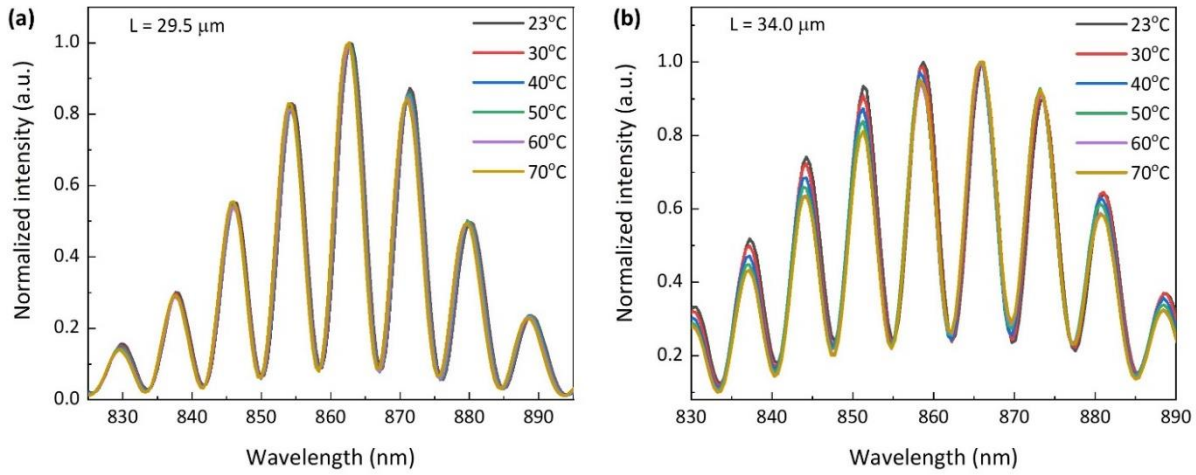

Figure 3. 11. The FPI spectra of the p(PETA) tip 29.5 µm in length (a) and 34.0 µm in length (b) measured in the environment with various temperatures. The environment humidity is maintained below 2 %.

In general, the wavelength shift of the FPI spectra induced by the temperature variation can be attributed to the change in length and refractive index of the tip according to the equation:

$$\frac{d\lambda}{dT} = \lambda\left(\frac{1}{L}\frac{dL}{dT} + \frac{1}{n_{eff}}\frac{dn_{eff}}{dT}\right) = \lambda(\alpha + \frac{\sigma}{n_{eff}}) \qquad (3.7)$$

Where α and σ are the thermal expansion and thermo-optic coefficients of the p(PETA). As the temperature increases, the length of the tip increases due to a positive thermal expansion coefficient, resulting in a red shift of the interference spectrum. Meanwhile, the refractive index of the material decreases with increasing temperature (i.e. a negative thermo-optic coefficients), resulting in a blue shift. There are no reported values of these coefficients for p(PETA) in the literature, so we cannot theoretically estimate the shift of the FPI signal with temperature variation. However, as observed above, the total shift of the FPI signal of the PETA tip is almost zero with increasing temperature, indicating that the red shift due to the length increase and the blue shift due to the refractive index decrease cancel each other out. With the insensitivity to temperature variation, FPI based on p(PETA) tips are greatly potential for practical humidity sensors.

3.4. Conclusion

In conclusion, we have demonstrated that a micro-length PETA tip attached to an optical fiber can be effectively used as an FPI sensor for relative humidity. The tip forms an optical cavity with fiber-core/ p(PETA) and p(PETA)/air interfaces acting as the two reflectors, resulting in an FPI signal with clear contrast between maximum and minimum wavelength positions. The FPI signal of the tip is highly sensitive to the relative humidity in the air, making it as an excellent humidity sensor. The sensitivity of the tip is consistently found to be approximately of 90pm/%RH, which is equivalent to a relative sensitivity of 104 ppm/%RH, in the humidity range from 30 to 80 %. This result is comparable to the data of previously reported fiber optic FPI humidity sensors. We have showcased the good reproducibility and stability of the FPI signal of the p(PETA) tip. The humidity sensing principle of the tip is attributed to the swelling effect of the p(PETA) in an increasingly humid environment, which consequently makes the polymer tip expanded, resulting in a red shift in the FPI signal. The cross effect of the temperature on the measurements is negligible as the FPI signal is insensitive to the temperature variation from 23 to 70 °C. All of these findings indicate a great potential of p(PETA) tips for fiber optic FPI humidity sensors.

References

[1] T. L. Yeo, T. Sun, and K. T. V. Grattan, 'Fibre-optic sensor technologies for humidity and moisture measurement', *Sensors and Actuators A: Physical*, vol. 144, no. 2, pp. 280–295, Jun. 2008, doi: 10.1016/j.sna.2008.01.017.

[2] L. Alwis, T. Sun, and K. T. V. Grattan, 'Optical fibre-based sensor technology for humidity and moisture measurement: Review of recent progress', *Measurement*, vol. 46, no. 10, pp. 4052–4074, Dec. 2013, doi: 10.1016/j.measurement.2013.07.030.

[3] X. Wang and O. S. Wolfbeis, 'Fiber-Optic Chemical Sensors and Biosensors (2015–2019)', vol. 92, no. 1, pp. 397–430, 2020, doi: 10.1021/acs.analchem.9b04708.

[4] S. Wu, G. Yan, Z. Lian, X. Chen, B. Zhou, and S. He, 'An open-cavity Fabry-Perot interferometer with PVA coating for simultaneous measurement of relative humidity and

temperature', *Sensors and Actuators B: Chemical*, vol. 225, pp. 50–56, Mar. 2016, doi: 10.1016/j.snb.2015.11.015.

[5] Y. Zhao, R. Tong, M.-Q. Chen, and F. Xia, 'Relative humidity sensor based on hollow core fiber filled with GQDs-PVA', *Sensors and Actuators B: Chemical*, vol. 284, pp. 96–102, Apr. 2019, doi: 10.1016/j.snb.2018.12.130.

[6] M. Chen, Y. Zhao, H. Wei, C. Zhu, and S. Krishnaswamy, '3D printed castle style Fabry-Perot microcavity on optical fiber tip as a highly sensitive humidity sensor', *Sensors and Actuators B: Chemical*, vol. 328, p. 128981, Feb. 2021, doi: 10.1016/j.snb.2020.128981.

[7] L. H. Chen, T. Li, C. C. Chan, R. Menon, P. Balamurali, M. Shaillender, B. Neu, X. M. Ang, P. Zu, W. C. Wong, and K. C. Leong., 'Chitosan based fiber-optic Fabry–Perot humidity sensor', *Sensors and Actuators B: Chemical*, vol. 169, pp. 167–172, Jul. 2012, doi: 10.1016/j.snb.2012.04.052.

[8] J. S. Santos, I. M. Raimundo, C. M. B. Cordeiro, C. R. Biazoli, C. A. J. Gouveia, and P. A. S. Jorge, 'Characterisation of a Nafion film by optical fibre Fabry–Perot interferometry for humidity sensing', *Sensors and Actuators B: Chemical*, vol. 196, pp. 99–105, Jun. 2014, doi: 10.1016/j.snb.2014.01.101.

[9] C. Lang, Y. Liu, K. Cao, Y. Li, and S. Qu, 'Ultra-compact, fast-responsive and highly-sensitive humidity sensor based on a polymer micro-rod on the end-face of fiber core', *Sensors and Actuators B: Chemical*, vol. 290, pp. 23–27, Jul. 2019, doi: 10.1016/j.snb.2019.03.099.

[10] Z. Hu, Y. Chen, J. Tan, Z. Yan, Z. Weng, M. Gusain, Y. Zhan, and L. Xiao, 'A hybrid self-growing polymer microtip for ultracompact and fast fiber humidity sensing', *Sensors and Actuators B: Chemical*, vol. 346, p. 130462, Nov. 2021, doi: 10.1016/j.snb.2021.130462.

[11] J. Liu, Y. Sun, and X. Fan, 'Highly versatile fiber-based optical Fabry-Pérot gas sensor', *Opt. Express*, vol. 17, no. 4, p. 2731, Feb. 2009, doi: 10.1364/OE.17.002731.

[12] M. Llera, T. Aellen, J. Hervas, Y. Salvadé, P. Senn, S. Le Floch, and H. Keppner, 'Liquid-air based Fabry-Pérot cavity on fiber tip sensor', *Opt. Express*, vol. 24, no. 8, p. 8054, Apr. 2016, doi: 10.1364/OE.24.008054.

[13] D. Zhang, H. Wei, H. Hu, and S. Krishnaswamy, 'Highly sensitive magnetic field microsensor based on direct laser writing of fiber-tip optofluidic Fabry–Pérot cavity', *APL Photonics*, vol. 5, no. 7, p. 076112, Jul. 2020, doi: 10.1063/5.0012988.

[14] P. E. Ciddor, 'Refractive index of air: new equations for the visible and near infrared', *Appl. Opt.*, vol. 35, no. 9, p. 1566, Mar. 1996, doi: 10.1364/AO.35.001566.

[15] K. P. Birch and M. J. Downs, 'An Updated Edlén Equation for the Refractive Index of Air', *Metrologia*, vol. 30, no. 3, pp. 155–162, Jan. 1993, doi: 10.1088/0026-1394/30/3/004.

[16] K. P. Birch and M. J. Downs, 'Correction to the Updated Edlén Equation for the Refractive Index of Air', *Metrologia*, vol. 31, no. 4, pp. 315–316, Jan. 1994, doi: 10.1088/0026-1394/31/4/006.

[17] J. Mathew, Y. Semenova, and G. Farrell, 'Fiber Optic Hybrid Device for Simultaneous Measurement of Humidity and Temperature', *IEEE Sensors J.*, vol. 13, no. 5, pp. 1632–1636, May 2013, doi: 10.1109/JSEN.2013.2238229.

[18] C.-L. Lee, Y.-W. You, J.-H. Dai, J.-M. Hsu, and J.-S. Horng, 'Hygroscopic polymer microcavity fiber Fizeau interferometer incorporating a fiber Bragg grating for simultaneously sensing humidity and temperature', *Sensors and Actuators B: Chemical*, vol. 222, pp. 339–346, Jan. 2016, doi: 10.1016/j.snb.2015.08.086.

Chapter 4

Fabry-Perot interferometer-based polymer tip for direct determination of water content in liquid phase

Abstract. Water contamination can detrimentally affect the quality, stability, and functions of many chemical products, making it critical to assess water content in various industrial fields. In this chapter, we propose a simple method using an FPI-based p(PETA) tip to determine water content directly in glycerol and ethylene glycol solutions, two important hygroscopic liquids widely used in various research and industrial fields. The p(PETA) tip is fully saturated by water prior to the sensing test in these hygroscopic solutions. The FPI signal of the p(PETA) tip immersed inside the solution was found to shift towards longer wavelengths with increasing water content in the solution. When the water contamination is below 10 wt.%, the shift of the FPI signal is reasonably considered to be linearly dependent on the water content. Within this range of water contamination, the sensitivities of the tip are approximately of 394 pm/wt.% for glycerol solution and 226 pm/wt.% for ethylene glycol solution. The shift in the FPI signal occurs due to the variation of the tip length, which is due to the loss of water molecules inside the p(PETA) structure caused by the hygroscopic solutions. Also, the intensity of the FPI signal is sensitive to the water content in the testing solutions. Therefore, FPI-based p(PETA) tips have a high potential for determining water content in solvents, including hydrocarbons.

4.1. Introduction

Water can detrimentally affect the quality, stability, and function of many products, including hydrocarbons [1]–[4], pharmaceuticals [5], [6] and food [7], [8]. It is therefore critical to assess the water content contaminated in liquid media in various industrial fields.

There are several common techniques for detecting the water contaminated in materials. The most common technique is Karl Fischer titration [9]. It relies on the oxidation of sulfur dioxide by iodine with the consumption of water in an alcohol solution containing a base. Once the titrating agent has achieved a volume sufficient for reacting with all the water inside the sample, the titration reaches its endpoint. This allows determination of water in equimolar proportion with iodine. This technique shows a high sensitivity; however, it is indirect and thus time-consuming, and requires the use of toxic chemicals. Another widely used method involves evaluating the changes in the fluorescence emission of receptors upon exposed to water [10]–[12]. Some typical receptors are anthracene [13], rhodamine [14], tetraphenylethene [15]. The fluorescence technique sometimes encounters photostability issues. Capacitance-based sensors are also a common type of water sensors, where water absorption typically leads to a change in both dielectric constant and conductivity, resulting in a change in the device capacitance [16], [17]. The method presented in [17] is indirect as it responds to water activity rather than water concentration.

Fiber optic sensors have also been widely used to measure water content in fluidic media based on different working principles. For instance, Xiong et al. [3], [18] reported fiber optic sensors based on the evanescent wave absorption spectrum. When light reflects at angles close to the critical angle within a fiber, a significant portion of the power extends into the cladding or medium surrounding the core, forming an fiber optic evanescent wave [19]. When the device is immersed in different fluidic media, both the evanescent field distribution and the effective refractive index of the guiding mode change, resulting in a wavelength shift in the FPI signal. Although these devices function well in glycerol, glycol and ethanol, they are very fragile due to the removal of the fiber cladding. In addition, they show an intensive noise and have a narrow sensing region. Fiber optic sensors based on surface plasmon resonance (SPR) are also introduced for measuring water content [4], [20]–[22]. SPR is an optical phenomenon that electrons in a metal thin layer (commonly comprised of Au or Ag) become

excited by light directed to the layer at a certain incident angle, and then propagate parallel to the surface of the metal. In these devices, a section of the fiber cladding is firstly removed and then a thin layer of metal with a high reflectivity is deposited onto the fiber core by physical [4] or chemical techniques [22]. A broadband light source is initiated at the metallized area and the SPR spectrum is recorded at the other end of the fiber. The resonance wavelength of the transmitted SPR spectrum is highly sensitive to the refractive index of the surrounding medium. The device therefore can detect the change in the refractive index of the surrounding medium caused by the presence of water. These SPR sensors are also fragile, difficult to fabricate, and expensive.

In this chapter, we present a novel method of using an FPI-based p(PETA) tip as an easy-to-use and environmentally friendly sensor of water content in hygroscopic liquids. We focus on investigating the water sensing function of p(PETA) tips in glycerol and ethylene glycol solutions as model systems. Glycerol is an important component in food storage [23], [24], cosmetics, pharmaceuticals [25], diffusion studies [26] and biofuels [27], [28]. Ethylene glycol is also a crucial organic compound that serves as an antifreeze, coolant and heat transfer agent in automobiles [29]. It is used in the productions of fuel cells [30], [31], H_2 energy [32], [33], and chemicals such as glyoxal, glycolic acid, and methyl glycolate [29], [34]. Both glycerol and ethylene glycol contain hydrophilic groups, which can cause the solvents to have undesired water content, subsequently reducing their purity, stability, and function. The method of using p(PETA) tips for directly detecting water content in hydrophilic liquids is based on the reversible absorption and desorption of water in p(PETA) materials, which results in a reversible variation in the tip length. This simple approach can be employed to measure water content in various liquid products comprising undesired hygroscopic ingredients.

4.2. Experimental methods

Poly (PETA) tips, with different lengths grown at the end of an optical fiber, are used for measuring water content in hygroscopic liquids. A home-made setup consisting of a SLED, spectrometer, isolator, and coupler was used to record the FPI signal when the tip is immersed inside the liquid, as schematically illustrated in Figure 4.1(a). A detailed description of the equipment can be found in Chapter 3, section 3.2.2.

The as-prepared tip is firstly placed in pure water for 15 min so that the water is fully absorbed by the p(PETA) chains. The tip is then immersed in water/glycerol or water/ethylene glycol solutions of varying water contents. The corresponding FPI spectra of the tip in each solution were recorded *in situ* in the liquid. It is noted that prior to each immersion of the tip in a glycerol or ethylene glycol solution, the tip is dipped again into pure water for 15 min, see Figure 4.1b. This step eliminates residual liquids from the tip surface and ensures the p(PETA) hydroxyl chains within the tip to be fully saturated again by water. This is the key step of our sensing method, so that the p(PETA) tip can function properly in the subsequent testing solution. The measurement setup was mechanically stabilized to prevent the polarization sensitivity of the fiber, which can affect the FPI stabilization.

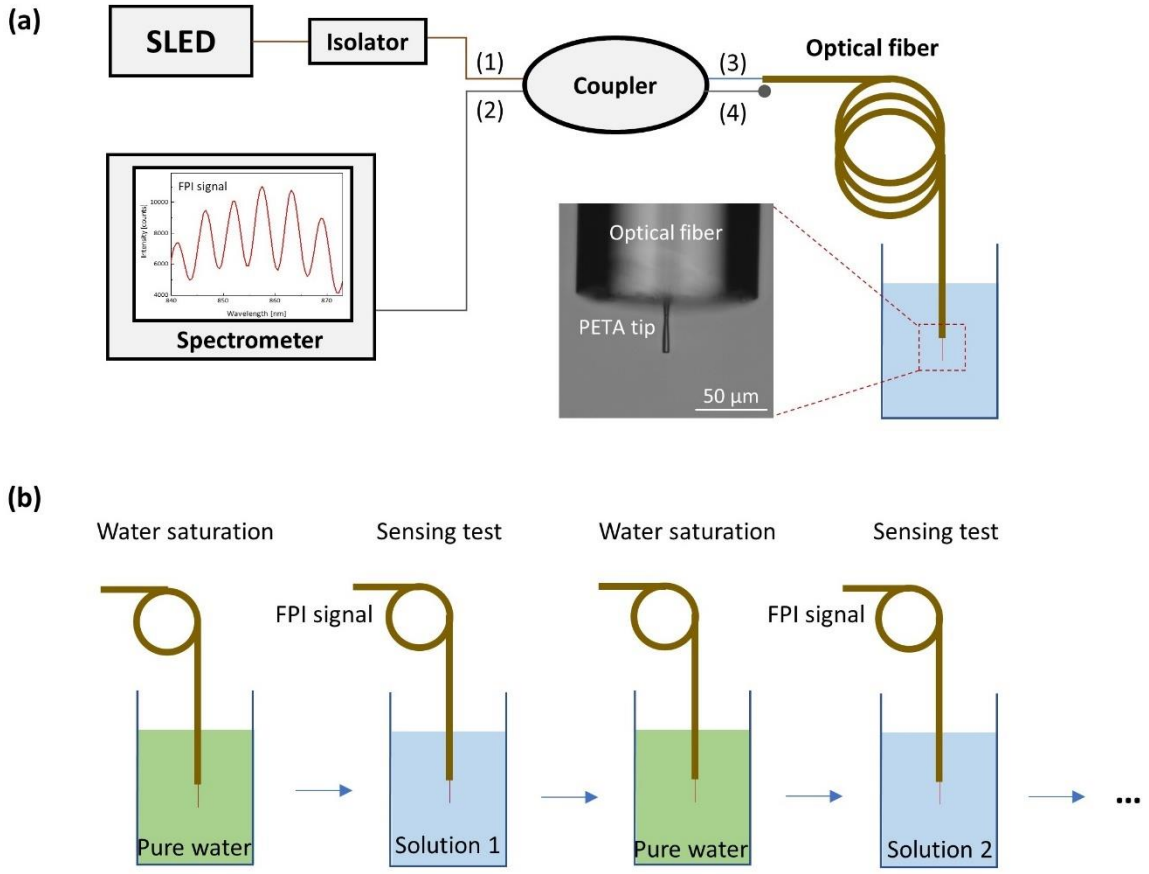

Figure 4. 1. (a) Schematic diagram of the experimental setup for measuring FPI signal of polymer tips in liquid environments. (b) Sequence of steps for detection of water content in hydrophilic solutions using the fiber optic p(PETA) tip.

4.3. Results and discussion: measurement of water content in glycerol solutions

4.3.1. FPI wavelength shift with varying water content

The FPI signal of the tip dipped inside the pure glycerol (water content = 0 wt.%) is recorded and considered as the reference signal. The FPI signals of the tip dipped inside water-contaminated glycerol samples are then recorded and compared with the reference FPI signal. It is observed that all the tips exhibit an FPI signal shifted towards longer wavelength with increasing water content in the glycerol solution, as shown in Figure 4.2. Namely, a 40.5 μm long tip exhibits an FPI signal with a maximum shift of 8.34 nm with water content in the glycerol solution increasing from 0 to 100 wt% (Figure 4.2(a)). Similarly, a 37.2 μm long tip shows an FPI signal with a red shift of 8.07 nm (Figure 4.2(b)).

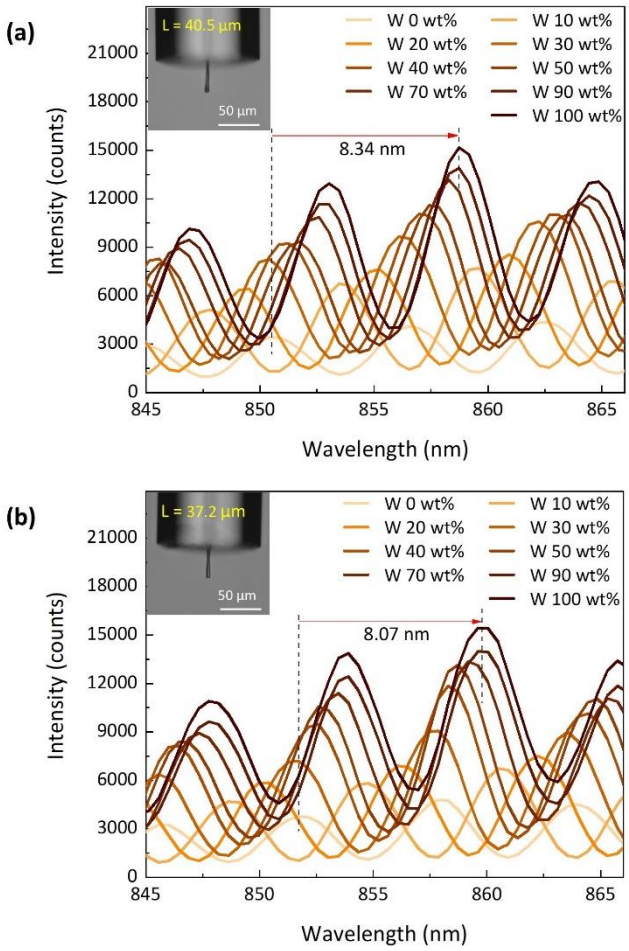

Figure 4. 2. FPI spectra of the p(PETA) tip (a) 40.5 µm long and (b) 37.2 µm long measured in glycerol solutions with various water contents. Insets are microscope images of used tips.

The dependence of the FPI wavelength shift of the tip on the water content is non-linear, as shown in Figure 4.3. The wavelength shift is significant in the low water content range and becomes less in the higher water content range. These trends are consistently observed for different tips regardless of the tip length, thereby affirming the excellent reproducibility of the sensors. Moreover, these data have suggested that the p(PETA) tips have great potential for sensing water at low contents, which is a promising development for practical applications.

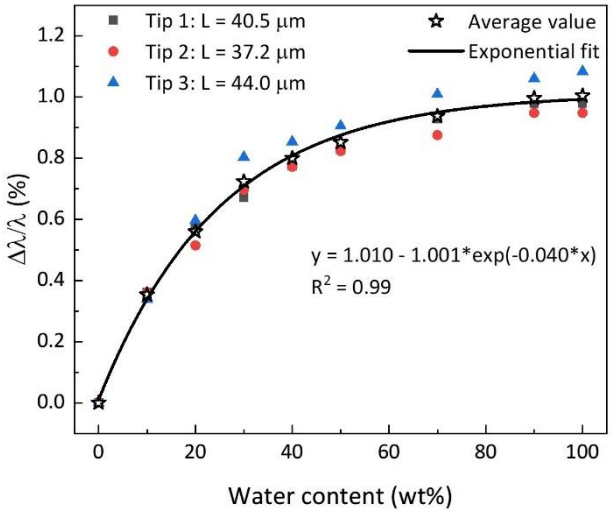

Figure 4. 3. The relative change of FPI wavelength position of different tips as a function of the water content in glycerol solutions.

We thus focus on the sensing performance of the p(PETA) tips in glycerol solutions where the water content is below 10 wt.%, see Figure 4.4. The polymer tip with a length of 40.5 µm exhibits a red shift of 3.51 nm in its FPI signal when the water content increases from 0 to 10 wt.%, as shown in Figure 4.4(a). Similarly, the 37.2 µm tip displays a red shift of 3.94 nm in the FPI signal with increasing the water content, as shown in Figure 4.4(b). The measurements performed on different tips reveal that the FPI wavelength shift follows nicely a linear dependence on the water content in the range from 0 to 10 wt.%, see Figure 4.4(c). The slope of this dependence indicates the sensitivity of the sensor, which is approximately of 394 pm/wt.%. With only minor deviation observed, we can conclude that the response of the p(PETA) tips to a low water content in glycerol solutions is sensitive and consistent.

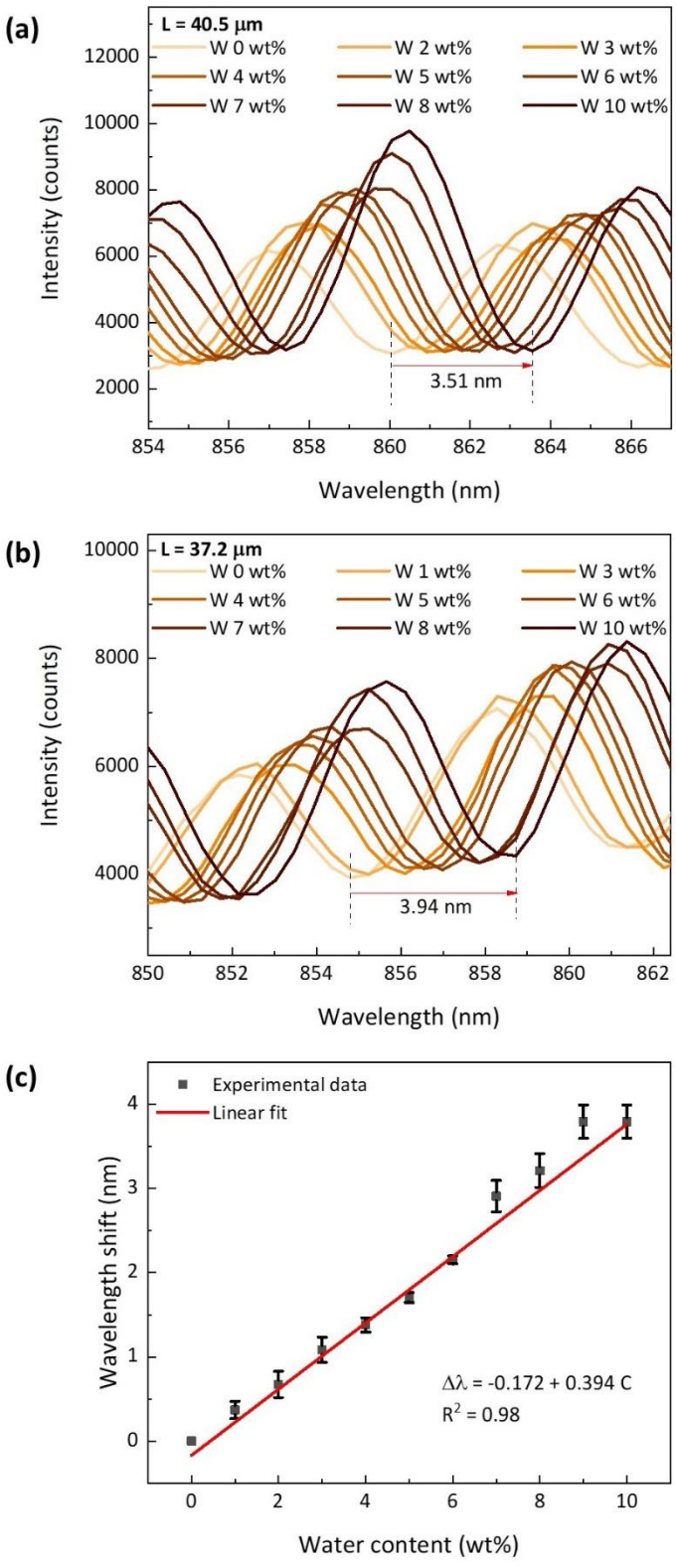

Figure 4. 4. FPI spectra of the p(PETA) tip (a) 40.5 µm long and (b) 37.2 µm long measured in glycerol solutions with various water contents (from 0 to 10 wt.%). (c) The FPI wavelength shift as a function of the water contaminated content.

4.3.2. Mechanism behind the FPI shift of the p(PETA) tip vs water content

The experimental results show that the FPI signal shifts towards longer wavelengths as the water content increases in glycerol solutions. However, mechanisms behind this shift have not been convincingly proposed in the literature. In a previous study, Frazão et al. [35] also observed a shift of the FPI signal of polymer tips in ethylene glycol/water solutions. These authors proposed that the shift is due to the evanescent field surrounding the polymer tip. When water concentration changes, the refractive index of the solution changes, causing the evanescent field and the effective refractive index of the tip-based cavity to change. This consequently leads to a shift of the FPI signal of the tip-based cavity. However, the contribution of the evanescent field is only significant in waveguides with a diameter in the nanometer range [36]. In our case, the p(PETA) tips have a diameter of approximately 5.0 µm, the same as the diameter of the fiber core. Therefore, the change of the effective refractive index of the guiding mode due to the evanescent field is negligible in our tips.

We propose that the primary cause behind the shift in the FPI signal of the p(PETA) tips is due to the high water-absorption capacity of glycerol [37]. It is noted that before each time of immersing the tip in aqueous glycerol solutions, the tip is always placed in pure water. This step allows water molecules to be fully absorbed by the hydroxyl groups within the p(PETA) chains, and inducing a maximum swelling effect in the tip. When the fully water-absorbed p(PETA) tip is immersed in a testing glycerol solution, the glycerol molecules strongly absorb water from the p(PETA) chains due to its highly hydrophilic nature, resulting in a reduction of the tip length. Compared to the pure glycerol, the water/glycerol solution absorb less water from the p(PETA) tip. The higher the amount of water contamination in the solution, the less the amount of water desorbed from the p(PETA) tip. The tip has its minimum length when being immersed in pure glycerol and then the length increases when the tip is inside the solution with higher water content. As a result, the FPI signal produced from the tip inside the solution with higher water content is red shifted as compare to that of the tip inside pure glycerol.

4.3.3. Repeatability of the FPI signal of the p(PETA) tips

Aside from a high sensitivity, a good signal repeatability and stability are also important for a sensor to be considered in practical applications. To study the repeatability of the FPI signal of the p(PETA) tip in glycerol-water mixtures with the water content varying from 0 wt.% to 100 wt.%, we recorded the FPI signal of the 40.5 µm long tip in two cycles of increasing and decreasing water content, see Figure 4.5(a, b). The peak wavelength position of the FPI signal at different water contents in both water variation cycles is shown in in Figure 4.5(c). It is evident that the wavelength position of the FPI spectra is repeatable for a specific water content, irrespective of the water variation trend.

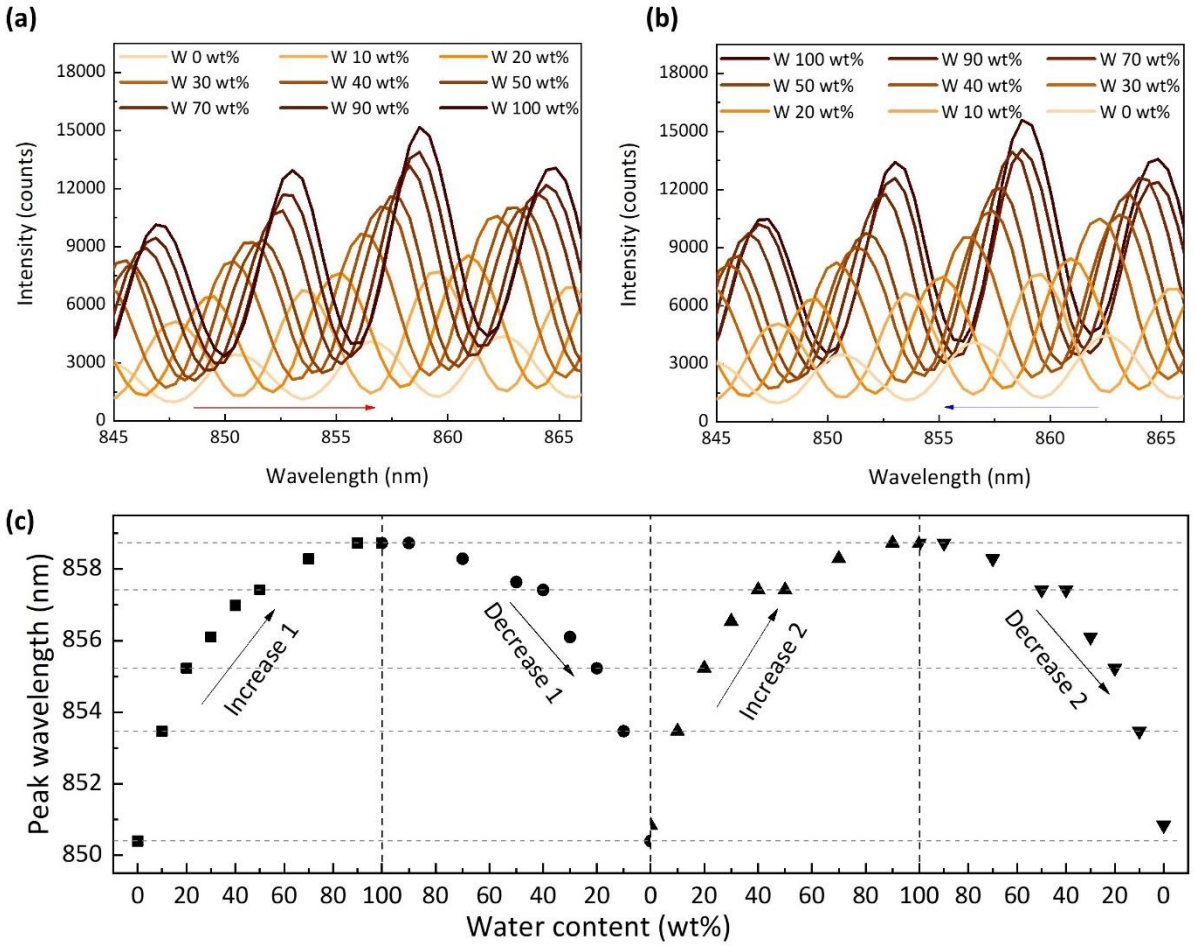

Figure 4. 5. FPI spectra of the tip 40.5 µm long measured in glycerol solutions with the water contaminated content (a) increases and (b) decreases. (c) The FPI wavelength positions of the p(PETA) tip at given water content during increasing-decreasing cycles. The measurements were conducted at room temperature.

4.3.4. Stability of the FPI signal of the p(PETA) tips

To study the sensing stability of the p(PETA) tips, we placed the tip a solution of a given specific water content and then examined the stability of the FPI signal over time. The FPI signal of a 44.0 μm long tip placed in glycerol solutions with 0, 50 and 100 wt.% water content are shown in Figure 4.6. The FPI signals measured immediately after the tip is dipped into the solution is considered as the 0-min data. It is seen that in all solutions, the tip needs a certain time to stabilize its FPI signal. In the pure water, the FPI signal slightly shifts to the right during the first 2 min before becoming stable. Meanwhile, in glycerol solutions, the tip needs approximately 10 min before producing a stable signal. However, the shifts of the FPI signal over time in all cases is only about 0.4 nm, the same to the resolution of our spectrometer and much smaller than the shift induced by the water content variation. We therefore can conclude that the p(PETA) tip sensor exhibits a good stability and a quick response time, considered to be 10 min.

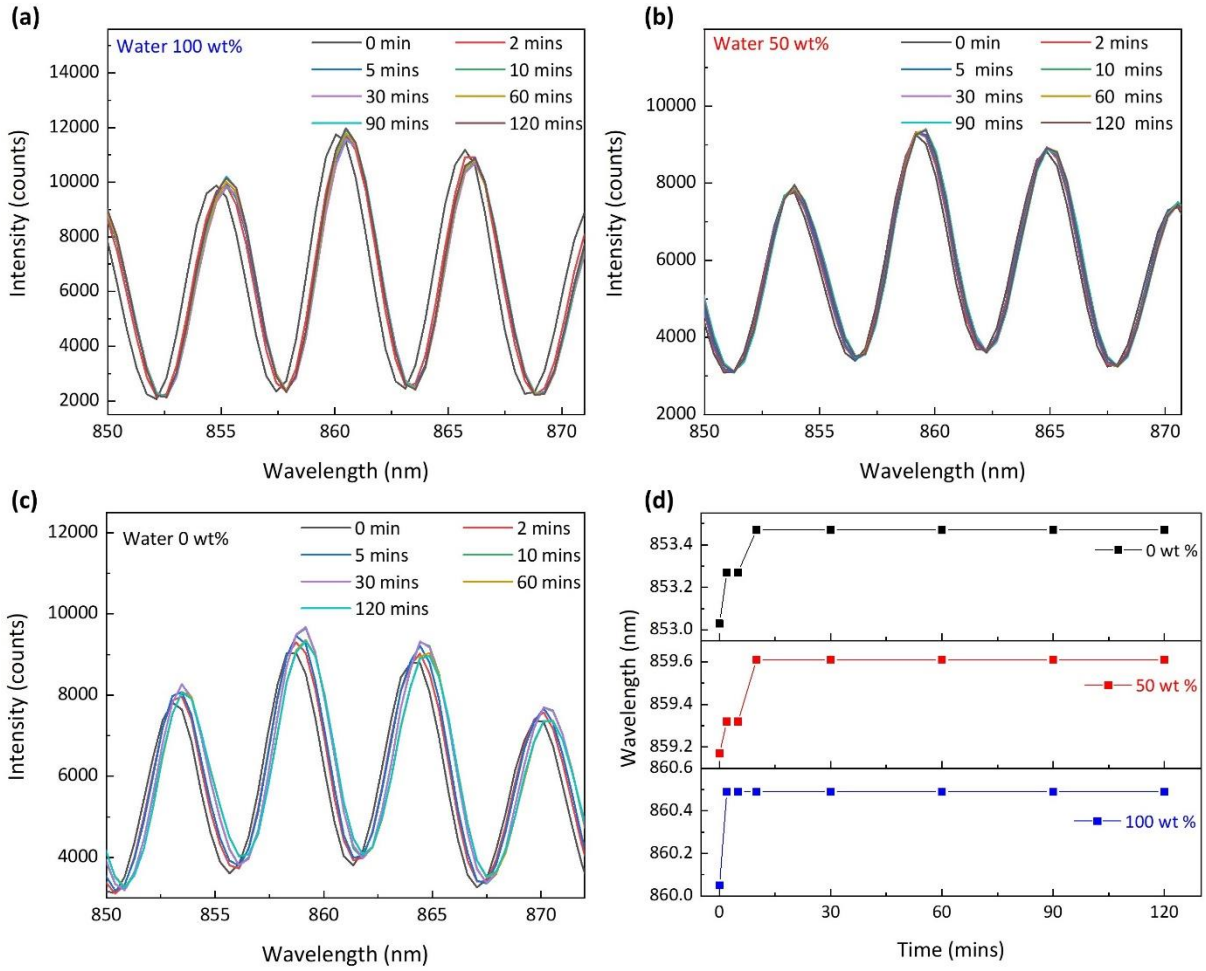

Figure 4. 6. (a-c) FPI spectra of the 44.0 µm long p(PETA) tip measured in different glycerol solutions. (d) FPI wavelength position of the tip as a function of time from when it was dipped into the solution.

4.3.5. Evolution of the FPI signal intensity with varying water content

From Figure 4.2, apart from the wavelength shift, one can also observe that the intensity of the FPI signal increases with increasing water content in the glycerol solution. Specifically, the intensity $(I_{max} - I_{min})$ of the FPI signal of the tip 40.5 µm long is linearly dependent on the water content of the solution, as shown in Figure 4.7(a). One therefore can use the change in the FPI peak intensity to detect the water content in the liquids. The sensitivity is estimated to be 78 counts/wt.%.

The change in the FPI intensity can be explained by considering the variation of the refractive index of the solution with different water contents. The refractive indices of the aqueous glycerol solutions were measured by an Abbe refractometer, see Figure 4.7(b). It is

seen that the refractive of the solution decreases linearly from 1.471 (for pure glycerol) to 1.339 (for pure water). As the refractive index of the solution decreases, the Fresnel reflection coefficient of the tip/solution interface ($R_2 = \frac{(n_p - n_e)^2}{(n_p + n_e)^2}$) increases, resulting in an increase in FPI signal intensity and $(I_{max} - I_{min})$, see the simulated results in Figure 4.7(c, d). The simulated data clearly confirm the obtained experimental data. However, it is noted that the FPI signal intensity is rather sensitive to the polarization of the fiber despite our best attempt to fix the measurement setup. Therefore, the change in signal intensity during the sensing measurements is not the primary principle for our sensors.

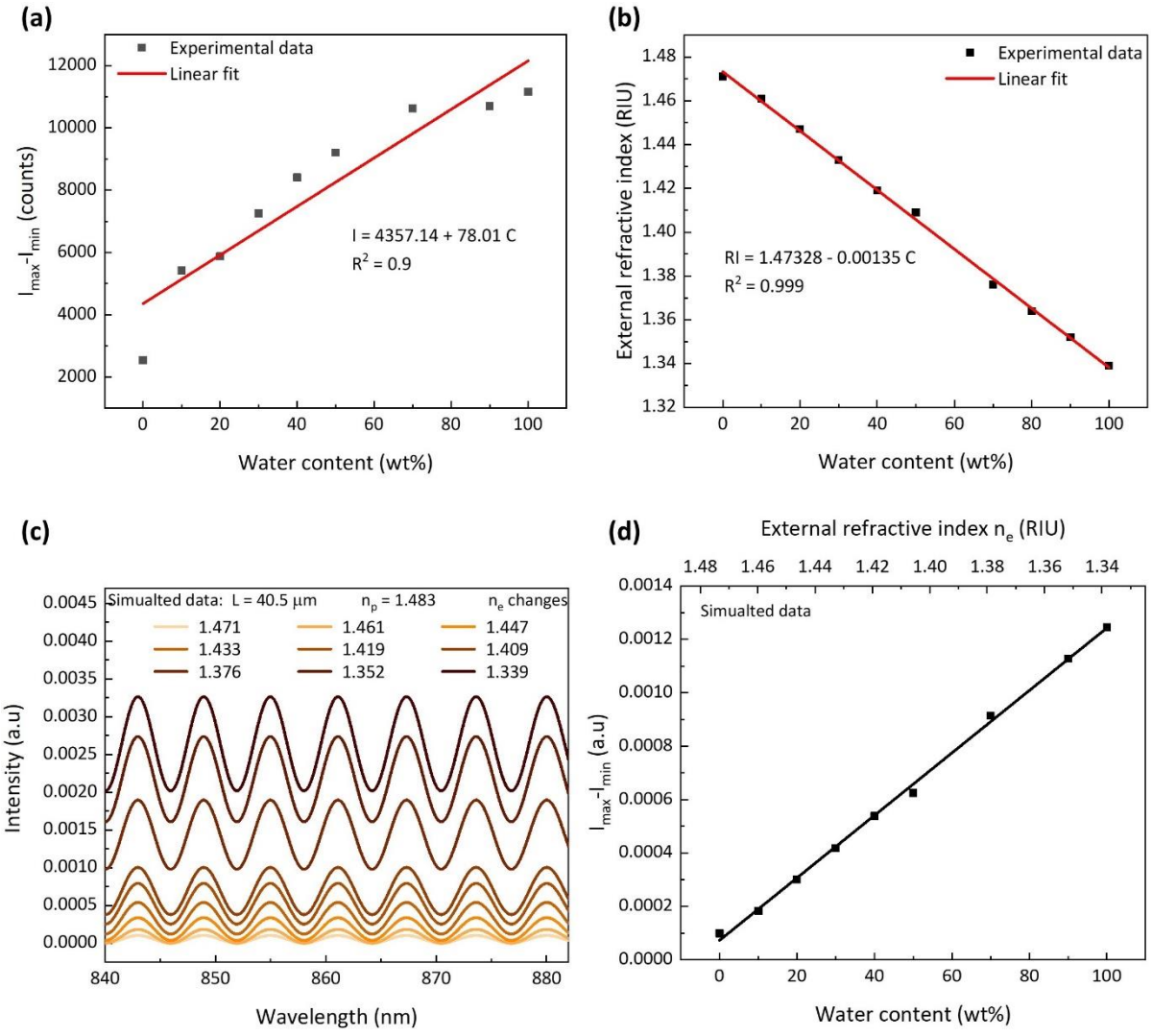

Figure 4. 7. (a) Evolution of the intensity of the FPI signal with the water content in glycerol. (b) Refractive index of glycerol solutions with different water contents. (c) Simulated FPI signal of the tip in the surrounding medium with various refractive indices. (d) Simulated $(I_{max} - I_{min})$ of the tip FPI signal as a function of the refractive index and water content in glycerol solution.

4.4. Measurements of water content in ethylene glycol solutions

The p(PETA) tip is able to detect water content not only in glycerol solutions, but also in ethylene glycol solutions. The measurement procedure is similar to that presented above for glycerol solutions. All the tips exhibit a red shift in their FPI signal when the water content in the ethylene glycol solution increases, see Figure 4.8(a, b). Namely, the FPI signal of the 40.5 µm and 37.2 µm long p(PETA) tips shifts towards longer wavelength of 4.20 nm and 4.39 nm, respectively, with increasing water from 0 to 100 wt.%. The signal shift follows a nonlinear function of the water content in the solution. A larger shift is observed in the low range of water content compared to the higher range, see Figure 4.8(c). This behavior is similar to that in the case of glycerol solutions. Additionally, the response of the tip is independent of its length, showing the good reproducibility of our sensors.

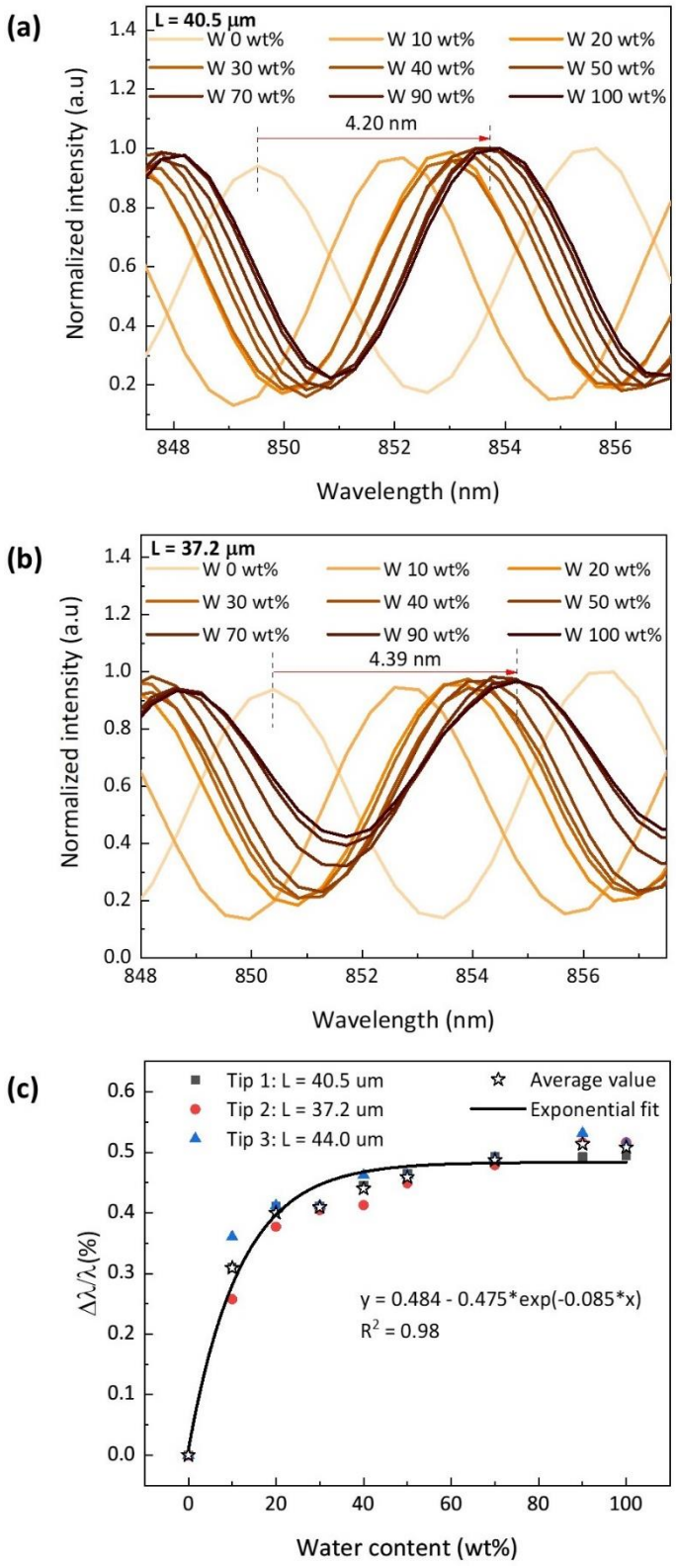

Figure 4. 8. FPI spectra of the p(PETA) tip (a) 40.5 µm long and (b) 37.2 µm long measured in ethylene glycol solutions with various water contents. (c) The relative change of FPI wavelength position as a function of water content in ethylene glycol solutions.

The sensing performance of the p(PETA) tips are then further examined in ethylene glycol solutions with a water content below 10 wt.%. As the water content increases from 0 to 10 wt.%, the polymer tips of 40.5 µm and 37.2 µm in length show a red shift of 2.63 nm and 2.42 nm in their FPI signals, respectively, see Figure 4.9(a, b). The average wavelength shift according to water content of various tips is shown in Figure 4.9(c), showing a good linearity function. The sensitivity of the tip is therefore estimated to be 226 pm/ wt.%. The mechanism behind the FPI wavelength shift of the tip in ethylene glycol solutions is similar to that in glycerol solutions. Ethylene glycol solution is more hydrophilic as compared with p(PETA), so it absorbs water from the p(PETA) chains when the tip is dipped inside the solution. The amount of water being absorbed depends on the concentration of the hydrophilic liquid. The tip length and consequently the FPI wavelength position are therefore sensitive to the water content in the solution. It is seen that the p(PETA) tip is less sensitive to water content in ethylene glycol than in glycerol. This is attributed to the less hydrophilic behavior of ethylene glycol compared to glycerol.

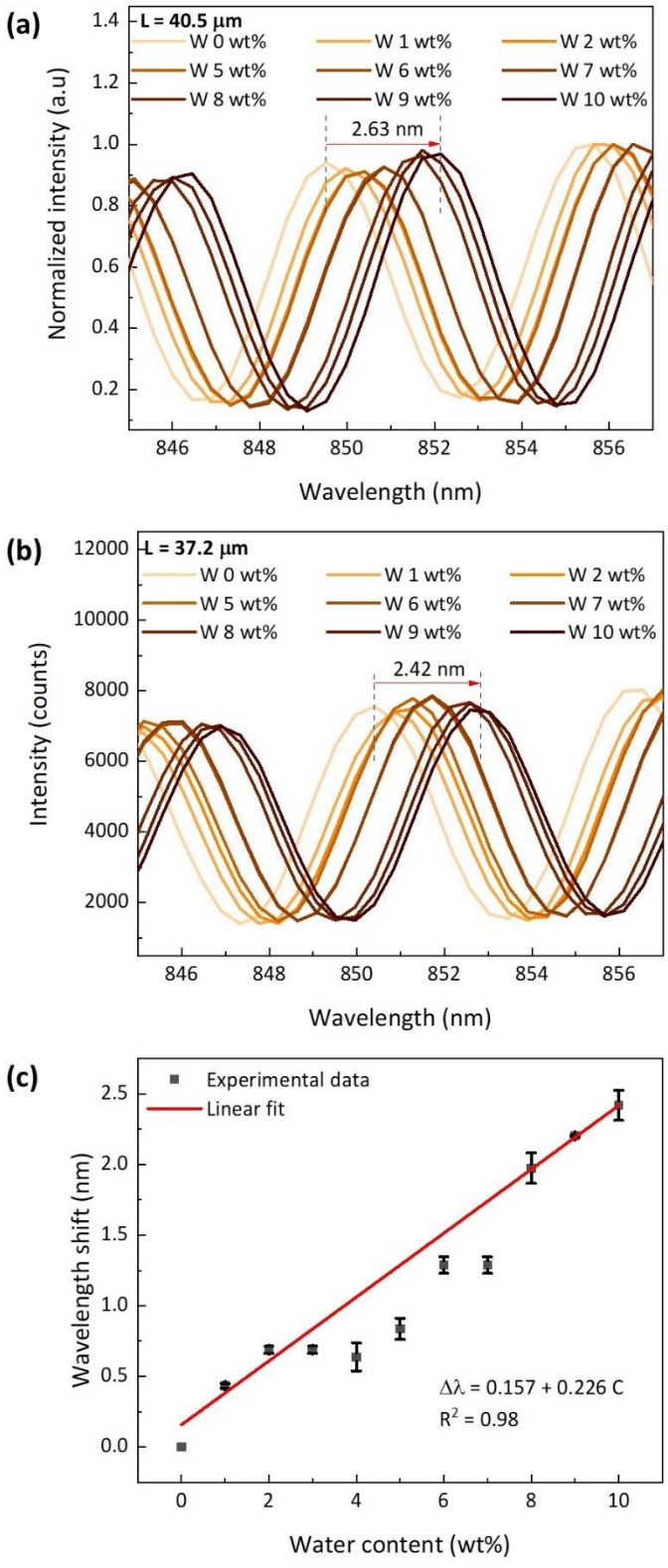

Figure 4. 9. FPI spectra of the p(PETA) tip (a) 40.5 µm long and (b) 37.2 µm long in ethylene glycol solutions with various water contents (from 0 to 10 wt.%). (c) The dependence of FPI wavelength position on the water content.

4.5. Conclusion

In this chapter, we have presented a simple method using the p(PETA) tip-based FPI for determining the water content of hygroscopic liquids, specifically in glycerol and ethylene glycol solutions. The as-prepared p(PETA) tip is initially saturated with water so that the polymer chains are fully swelled. The tip is then placed directly inside the hygroscopic solutions and the FPI signal was observed to sensitive to the water content within the solution. The FPI signal shifts towards longer wavelengths in a nonlinear function as the water content increases from 0 to 100 wt.%. However, when water content is below 10 wt.%, the FPI shift is reasonably in a linear dependence on the water content. Within this range of water contamination, the sensors display a sensitivity of 394 pm/wt.% for glycerol solutions and 226 pm/wt.% for ethylene glycol solutions. The FPI signal of the p(PETA) tip is highly stable and repeatable. The shift of the FPI signal is attributed to the reduction of the tip length, which is caused by the water absorption of the hygroscopic solutions. Moreover, the change of refractive index of the external environment affects the intensity of the FPI signal. Thus, the p(PETA) tip-based FPI sensor is promising for direct determination of water content in organic solutions, including hydrocarbons.

References

[1] S. A. Margolis, 'Effect of Hydrocarbon Composition on the Measurement of Water in Oils by Coulometric and Volumetric Karl Fischer Methods', *Anal. Chem.*, vol. 70, no. 20, pp. 4264–4270, Oct. 1998, doi: 10.1021/ac980149h.

[2] L. A. Frink and D. W. Armstrong, 'Determination of Trace Water Content in Petroleum and Petroleum Products', *Anal. Chem.*, vol. 88, no. 16, pp. 8194–8201, Aug. 2016, doi: 10.1021/acs.analchem.6b02006.

[3] F. B. Xiong and D. Sisler, 'Determination of low-level water content in ethanol by fiber-optic evanescent absorption sensor', *Optics Communications*, vol. 283, no. 7, pp. 1326–1330, Apr. 2010, doi: 10.1016/j.optcom.2009.11.075.

[4] S. K. Srivastava, R. Verma, and B. D. Gupta, 'Surface plasmon resonance based fiber optic sensor for the detection of low water content in ethanol', *Sensors and Actuators B: Chemical*, vol. 153, no. 1, pp. 194–198, Mar. 2011, doi: 10.1016/j.snb.2010.10.038.

[5] R. K. Khankari, D. Law, and D. J. W. Grant, 'Determination of water content in pharmaceutical hydrates by differential scanning calorimetry', *International Journal of Pharmaceutics*, vol. 82, no. 1–2, pp. 117–127, Apr. 1992, doi: 10.1016/0378-5173(92)90080-L.

[6] L. A. Frink and D. W. Armstrong, 'Water Determination in Solid Pharmaceutical Products Utilizing Ionic Liquids and Headspace Gas Chromatography', *Journal of Pharmaceutical Sciences*, vol. 105, no. 8, pp. 2288–2292, Aug. 2016, doi: 10.1016/j.xphs.2016.05.014.

[7] H.-D. Isengard, 'Water content, one of the most important properties of food', *Food Control*, vol. 12, no. 7, pp. 395–400, Oct. 2001, doi: 10.1016/S0956-7135(01)00043-3.

[8] M. Mathlouthi, 'Water content, water activity, water structure and the stability of foodstuffs', *Food Control*, vol. 12, no. 7, pp. 409–417, 2001, doi: 10.1016/S0956-7135(01)00032-9.

[9] E. Scholz, *Karl Fischer titration: determination of water*. Springer Science & Business Media, 2012.

[10] X. Yang, C.-G. Niu, Z.-J. Shang, G.-L. Shen, and R.-Q. Yu, 'Optical-fiber sensor for determining water content in organic solvents', vol. 75, no. 1, pp. 43–47, 2001, doi: 10.1016/S0925-4005(00)00740-1.

[11] Z. Li, Q. Yang, R. Chang, G. Ma, M. Chen, and W. Zhang, 'N-Heteroaryl-1,8-naphthalimide fluorescent sensor for water: Molecular design, synthesis and properties', *Dyes and Pigments*, vol. 88, no. 3, pp. 307–314, Mar. 2011, doi: 10.1016/j.dyepig.2010.07.009.

[12] S. Mishra and A. K. Singh, 'Optical sensors for water and humidity and their further applications', *Coordination Chemistry Reviews*, vol. 445, p. 214063, Oct. 2021, doi: 10.1016/j.ccr.2021.214063.

[13] Y. Ooyama, A. Matsugasako, K. Oka, T. Nagano, M. Sumomohi, K. Komaguchi, I. Imea, and Y. Harima, 'Fluorescence PET (photo-induced electron transfer) sensors for water based on anthracene–boronic acid ester', *Chem. Commun.*, vol. 47, no. 15, p. 4448, 2011, doi: 10.1039/c1cc10470e.

[14] G. Men, G. Zhang, C. Liang, H. Liu, B. Yang, Y. Pan, Z. Wang, and S. Jiang, 'A dual channel optical detector for trace water chemodosimetry and imaging of live cells', *Analyst*, vol. 138, no. 10, p. 2847, 2013, doi: 10.1039/c3an36887d.

[15] Y. Zhang, D. Li, Y. Li, and J. Yu, 'Solvatochromic AIE luminogens as supersensitive water detectors in organic solvents and highly efficient cyanide chemosensors in water', *Chem. Sci.*, vol. 5, no. 7, p. 2710, 2014, doi: 10.1039/c4sc00721b.

[16] M. A. Nurge and S. A. Perusich, 'In-line capacitance sensor for real-time water absorption measurements', *Sensors and Actuators B: Chemical*, vol. 150, no. 1, pp. 105–111, Sep. 2010, doi: 10.1016/j.snb.2010.07.035.

[17] S.-I. Ohira, K. Goto, K. Toda, and P. K. Dasgupta, 'A Capacitance Sensor for Water: Trace Moisture Measurement in Gases and Organic Solvents', *Anal. Chem.*, vol. 84, no. 20, pp. 8891–8897, Oct. 2012, doi: 10.1021/ac3024069.

[18] F. B. Xiong, W. Z. Zhu, H. F. Lin, and X. G. Meng, 'Fiber-optic sensor based on evanescent wave absorbance around 2.7 μm for determining water content in polar organic solvents', *Appl. Phys. B*, vol. 115, no. 1, pp. 129–135, Apr. 2014, doi: 10.1007/s00340-013-5583-2.

[19] G. P. Anderson, 'Chapter 2 - Evanescent wave fiber optic biosensors', in *Optical Biosensors (Second Edition)*, Elsevier, 2008, pp. 83–138. [Online]. Available: https://www.sciencedirect.com/science/article/pii/B9780444531254500048

[20] R. C. Jorgenson, and S. S. Yee, 'A fiber-optic chemical sensor based on surface plasmon resonance', *Sensors and Actuators B: Chemical*, vol. 12, no. 3, pp. 213–220, Apr. 1993, doi: 10.1016/0925-4005(93)80021-3.

[21] A. K. Sharma, R. Jha, and B. D. Gupta, 'Fiber-Optic Sensors Based on Surface Plasmon Resonance: A Comprehensive Review', *IEEE Sensors J.*, vol. 7, no. 8, pp. 1118–1129, Aug. 2007, doi: 10.1109/JSEN.2007.897946.

[22] Y. Zhao, Z. Deng, and Q. Wang, 'Fiber optic SPR sensor for liquid concentration measurement', *Sensors and Actuators B: Chemical*, vol. 192, pp. 229–233, Mar. 2014, doi: 10.1016/j.snb.2013.10.108.

[23] P. Cazón, M. Vázquez, and G. Velazquez, 'Cellulose-glycerol-polyvinyl alcohol composite films for food packaging: Evaluation of water adsorption, mechanical properties, light-barrier properties and transparency', *Carbohydrate Polymers*, vol. 195, pp. 432–443, Sep. 2018, doi: 10.1016/j.carbpol.2018.04.120.

[24] S. Galus and A. Lenart, 'Optical, mechanical, and moisture sorption properties of whey protein edible films', *J Food Process Engineering*, vol. 42, no. 6, p. e13245, Oct. 2019, doi: 10.1111/jfpe.13245.

[25] G. P. Da Silva, M. Mack, and J. Contiero, 'Glycerol: A promising and abundant carbon source for industrial microbiology', *Biotechnology Advances*, vol. 27, no. 1, pp. 30–39, Jan. 2009, doi: 10.1016/j.biotechadv.2008.07.006.

[26] A. D. Ruvalcaba-Cardenas, P. Thurgood, S. Chen, K. Khoshmanesh, and F. J. Tovar-Lopez, 'Droplet on Soft Shuttle: Electrowetting-on-Dielectric Actuation of Small Droplets', *ACS Appl. Mater. Interfaces*, vol. 11, no. 42, pp. 39283–39291, Oct. 2019, doi: 10.1021/acsami.9b10796.

[27] M. R. Monteiro, C. L. Kugelmeier, R. S. Pinheiro, M. O. Batalha, and A. Da Silva César, 'Glycerol from biodiesel production: Technological paths for sustainability', *Renewable and Sustainable Energy Reviews*, vol. 88, pp. 109–122, May 2018, doi: 10.1016/j.rser.2018.02.019.

[28] W. A. González, D. López, and J. F. Pérez, 'Biofuel quality analysis of fallen leaf pellets: Effect of moisture and glycerol contents as binders', *Renewable Energy*, vol. 147, pp. 1139–1150, Mar. 2020, doi: 10.1016/j.renene.2019.09.094.

[29] H. Yue, Y. Zhao, X. Ma, and J. Gong, 'Ethylene glycol: properties, synthesis, and applications', *Chem. Soc. Rev.*, vol. 41, no. 11, p. 4218, 2012, doi: 10.1039/c2cs15359a.

[30] A. O. Neto, T. R. R. Vasconcelos, R. W. R. V. D. Silva, M. Linardi, and E. V. Spinace, 'Electro-oxidation of ethylene glycol on PtRu/C and PtSn/C electrocatalysts prepared by alcohol-reduction process', *J Appl Electrochem*, vol. 35, no. 2, pp. 193–198, Feb. 2005, doi: 10.1007/s10800-004-5824-5.

[31] H. Wang, Z. Jusys, and R. J. Behm, 'Adsorption and electrooxidation of ethylene glycol and its C2 oxidation products on a carbon-supported Pt catalyst: A quantitative DEMS study', *Electrochimica Acta*, vol. 54, no. 26, pp. 6484–6498, Nov. 2009, doi: 10.1016/j.electacta.2009.05.097.

[32] R. D. Cortright, R. R. Davda, and J. A. Dumesic, 'Hydrogen from catalytic reforming of biomass-derived hydrocarbons in liquid water', vol. 418, pp. 964–967, 2002, doi: 10.1038/nature01009.

[33] D. J. M. De Vlieger, A. G. Chakinala, L. Lefferts, S. R. A. Kersten, K. Seshan, and D. W. F. Brilman, 'Hydrogen from ethylene glycol by supercritical water reforming using noble

and base metal catalysts', *Applied Catalysis B: Environmental*, vol. 111–112, pp. 536–544, Jan. 2012, doi: 10.1016/j.apcatb.2011.11.005.

[34] M. A. Salaev, A. A. Krejker, O. V. Magaev, V. S. Malkov, A. S. Knyazev, E. S. Borisova, V. M. Khanaev, O. V. Vodyankina, and L. N. Kurina, 'Ethylene glycol oxidation over supported catalyst in tubular reactor', *Chemical Engineering Journal*, vol. 172, no. 1, pp. 399–409, Aug. 2011, doi: 10.1016/j.cej.2011.05.079.

[35] O. Frazão, P. Caldas, J. L. Santos, P. V. S. Marques, C. Turck, D. J. Lougnot, and O. Soppera, 'Fabry-Perot refractometer based on an end-of-fiber polymer tip', *Opt. Lett.*, vol. 34, no. 16, p. 2474, Aug. 2009, doi: 10.1364/OL.34.002474.

[36] D. Zhang, H. Wei, H. Hu, and S. Krishnaswamy, 'Highly sensitive magnetic field microsensor based on direct laser writing of fiber-tip optofluidic Fabry–Pérot cavity', *APL Photonics*, vol. 5, no. 7, p. 076112, Jul. 2020, doi: 10.1063/5.0012988.

[37] H. J. Chen, P. Y. Lee, C. Y. Chen, S. L. Huang, B. W. Huang, F. J. Dai, C. F. Chau, C. S. Chen. and Y. S. Lin, 'Moisture retention of glycerin solutions with various concentrations: a comparative study', *Sci Rep*, vol. 12, no. 1, p. 10232, Jun. 2022, doi: 10.1038/s41598-022-13452-2.

Chapter 5

Fabry-Perot interferometer chemical sensor based on molecularly imprinted polymer

Abstract. Molecularly imprinted polymers (MIPs) are artificial receptor polymers, synthesized by polymerizing functional and cross-linking monomers in the presence of a specific molecular template. Afterwards, if the molecular template is removed from the MIP structure, the MIP then contains binding sites and is able to recognize chemical analytes that possess complementary shape, size, and functional groups as the removed template. In this chapter, we develop a polymer tip comprising a PETA core and a MIP shell which can be used as an FPI-based sensor for detecting Dansyl-L-phenylalanine (Dansyl-L-Phe). The p(PETA) tip is initially fabricated by a self-guiding polymerization and the MIP shell is then formed on the p(PETA) tip by photopolymerization using N-(carbobenzyloxy)-L-phenylalanine (Z-L-Phe) template. The FPI signal of the tip is observed to shift in its wavelength position when the MIP layer binds to Dansyl-L-phe. The limit of detection for Dansyl-L-phe is 75 μM. The shift of the FPI signal is attributed to the change in the refractive index of the MIP layer when its binding sites are occupied by analyte molecules. The fiber optic FPI based on the p(PETA)/MIP tip also exhibits a high selectivity, which is a crucial requirement for chemical sensors. Our findings demonstrate the great potential of the p(PETA)/MIP-based FPI as a chemical sensor with good affinity and selectivity.

Abbreviations:

Pentaerythritol triacrylate:	PETA
Dansyl-L-phenylalanine:	Dansyl-L-Phe
N-(carbobenzyloxy)-L-phenylalanine:	Z-L-Phe
N-(Carbobenzyloxy)-D-phenylalanine:	Z-D-Phe
Methyl methacrylate:	MAA
4-vinylpyridine:	4-VP
Ethylene glycol dimethacrylate:	EGDMA
Phenylbis(2,4,6-trimethylbenzoyl)phosphine oxide:	BAPO
4-cyano-4-((dodecylsulfanylthiocarbonyl)sulfanyl)pentanoic acid:	CDTPA

5.1. Introduction

Molecularly imprinted polymers (MIPs) are artificial polymeric receptors that can be synthesized by polymerizing functional and cross-linking monomers in the presence of a specific molecular target or its derivative as a template. When the molecular template is then removed from the MIP structure, the MIP contains binding sites which are able to rebind chemical analytes with similar shape, size, and functional groups to the template [1]. MIPs are chemically stable and easily integrated into industrial manufacturing. Moreover, they can be tailored to specific molecules of interest, making them comparable to natural receptors. Thanks to these advantages, MIPs have been used in various fields, including medical therapy and drug delivery [2], [3], cosmetics [4] and catalysis [5], [6]. They are particularly attractive for (bio)chemical sensor with a high affinity and selectivity [7]–[9].

The most common working principle of available MIP-based chemical sensors is based on the change in fluorescence intensity upon the binding of MIPs to specific targets. These MIP-based sensors are usually equipped with optical fibers that can maximize the excitation and collection of optical signals from the MIP, subsequently enhancing the performance and

convenience of the sensor. Numerous fiber optic MIP-based fluorescent sensors have been proposed for the detection of pesticides and insecticides [10], cocaine [11], Dansyl-L-Phenylalanine [12], herbicide 2,4-D [12], enrofloxacin [13], and ciprofloxacin [14]. These analytes exhibit a strong fluorescence. Upon excitation, the fluorescence emitted from the MIP structure is collected by a spectrometer or an epi-fluorescence microscope. The fluorescence intensity is observed to change upon the binding between the MIP and the analyte. These sensors demonstrate high sensitivity, affinity and fast response time.

Aside from the fluorescence-based sensors, Gupta's group [15]–[19] have developed a generation of MIP-based chemical sensors using surface plasmon resonance signal. The authors removed the jacket and cladding from the core of an optical fiber and then deposited a thin Ag layer on the fiber core by thermal evaporation. The pre-polymeric MIP solution was then applied to the Ag-coated core fiber by a dip coating process and thermally polymerized for 24 h. The surface plasmon resonance of the Ag layer depends on the refractive index of the surrounding dielectric medium, in this case the MIP layer. The change in the refractive index of the MIP layer during the binding process with analytes results in a change in the resonance wavelength of the Ag layer. Thus, this technique can be used to detect without labeling specific analytes such as vitamin B3 [15], erythromycin [17], atrazine [18], dopamine [19]. Zeni's group [20] also applied this method but using Au instead of Ag to create an fiber optic MIP-based sensor to detect nicotine. The pre-MIP film was coated on the Au layer by a spin coating method, followed by thermal polymerization for 16 h. These authors have also tried to directly disperse Au nanostars in a pre-MIP solution and then formed a layer of MIP/Au composite on a fiber core to develop a sensor for 2,4,6-trinitrotoluene [21]. Overall, the reported sensors exhibit good sensitivity and affinity to a specific analyte. The surface plasmon resonance technique can be used to label-free detect a wider range of analytes.

In this chapter, we propose a fiber optic MIP-based sensor for the detection of analytes using its FPI signal. The change in the refractive index of the MIP structure upon binding with analytes can lead to a shift in the FPI signal of the MIP tip. This type of MIP sensor is expected to be able to work for both fluorescent and non-fluorescent analytes. As already seen in chapter 1, Queirós et al. [22] reported a MIP-based sensor using its FPI signal for the detection of microcystin-LR. In their study, a MIP membrane was formulated by dip-coating an optical fiber into a sol-gel MIP solution. To the best of our knowledge, there has been no further

development of FPI sensors based on MIP. Our main objective is to explore a new configuration of the label-free FPI sensor based on MIP for the detection of different analytes. In the following sections, we first present our attempt to directly formulate a MIP tip on the facet of an optical fiber. However, this formulation is unsuccessful due to a poor attachment of the MIP tip to the fiber core. We then propose a formulation of a tip consisting of a p(PETA) core and a MIP shell layer. This tip takes advantage of the mechanically stable p(PETA) core which is then covered by a MIP shell layer. The chemical sensing performance of the p(PETA)/MIP tip is then characterized and discussed.

5.2. Materials

PETA and Dansyl-L-Phe (98%) were from ABCR. CDTPA (97%), Z-L-Phe (99%), MAA (99%), EGDMA (98%), BAPOs (97%), methanol (≥99.9%), absolute ethanol (≥99.8%), acetic acid (≥99%), acetonitrile (≥99.9%), 4-VP (95%) were from Sigma-Aldrich. 4-VP was freshly distilled under reduced pressure before use. Z-D-Phe was from Fluka Analytical.

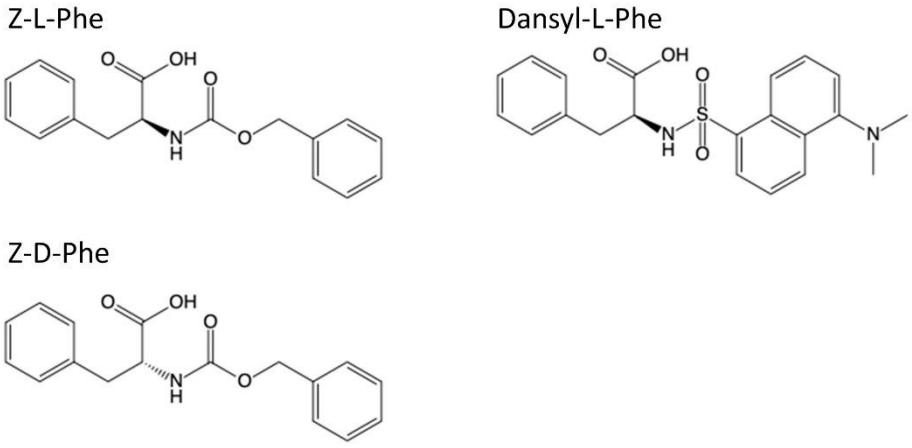

Figure 5. 1. Chemical structures of Z-L-Phe, Dansyl-L-Phe and Z-D-Phe used in this study.

5.3. Formation of a MIP tip on the facet of an optical fiber

The self-guiding polymerization technique appears to be a promising approach to make FPI-based polymer tip sensors. With this in mind, we have attempted to formulate a tip made of MIP on the facet of the optical fiber for the detection of amino acid Dansyl-L-Phe as a proof-of-concept.

The formulation is prepared according to previous research [23], using a template Z-L-Phe, functional monomer MAA and 4-VP, and crosslinker EGDMA. These materials were dissolved in acetonitrile following a molar ratio of 1/4/4/40. Phenylbis (2,4,6-trimethylbenzoyl)phosphine oxide (BAPO), acting as a photoinitiator, is then added into the mixture with an amount of 1 mol % relative to the molar number of the polymerizable groups present in the mixture. One end of the single mode optical fiber is connected to a 375-nm UV laser and the other end is dipped into the formulation.

Using an exposure dose of 10 µW x 1.0 min, we obtained a polymerized MIP tip attached to the fiber, as shown in the Figure 5.2(a). However, with the same conditions, we were unable to obtain a tip in other attempts, as shown in Figure 5.2(b). Despite a thoughtful optimization of the fabrication conditions by adjusting the laser power and the exposure across a wide range, the same problem persisted. We suspect that the adhesion between the polymerized MIP tip and the fiber facet is poor. In addition, the presence of O_2 may affect the polymerization process of MIP tip. Moreover, the use of photo-initiator based on free radical polymerization does not allow polymer chains to be well controlled in their length [1], [24]. It is therefore extremely challenging to directly create a MIP tip at the end of the fiber.

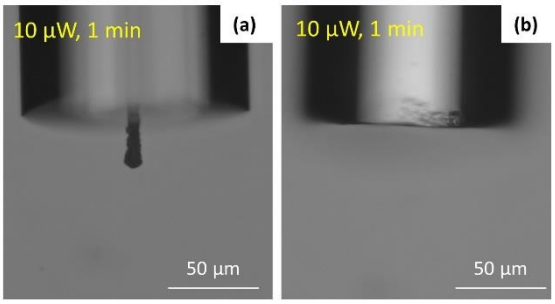

Figure 5. 2. Fabrication of a MIP tip is successful in (a) but unsuccessful in (b). The formulation conditions are the same in two cases.

In the attempt to fabricate feasible MIP-based sensors, Ton et al. [12] and Paruli et al. [25] have proposed to formulate MIP layers on supporting polymer structures. These studies inspire us to consider an alternative approach towards a MIP/polymer core-shell structure at the end of an optical fiber. The p(PETA) tip formulated at the end of the fiber by self-guiding polymerization is expected to be a mechanically stable support for a thin MIP layer to be grown on. In addition, instead of using free radical photo-initiator in the MIP formulation which does not allow to control the length of polymer chains, or fine-tuning the properties of polymer, we use photo-iniferters (which stands from initiator, transfer agent, and terminator) to have a better control of the MIP polymerization [24], [25]. Indeed, Garcia-Soto et al. [26] have used CDTPA photoiniferter for the synthesis of MIP particles, granting control over the size the polymer chains. In our experiment, we use CDTPA photoiniferter to functionalize the MIP layer surrounding the p(PETA) tip.

5.4. Formulation of a p(PETA)/MIP core-shell tip

The p(PETA) tip were fabricated by a self-guiding photo-polymerization method with an exposure dose of 1.0 µW x 1.0 s, as described in detail in Chapter 2. By trial and error, we observed that the formation of a MIP layer on a poorly polymerized PETA tip is much more effective than that on a fully-polymerized PETA tip. We believe that the larger number of residual double bonds in the p(PETA) tips without post-polymerization allow for sufficient anchoring CDTPA photoiniferter to surface-initiate polymerization of the MIP layer [25]. Thus, p(PETA) tips without post-polymerization were used in this study. The formulation procedure of a MIP layer on the p(PETA) tip is based on the original recipe suggested by K. Haupt's group at Université de Technologie de Compiègne - GEC Laboratory with modifications to suit the working conditions at IMS lab. A step-by-step procedure for formulating a shell layer of MIP surrounding the PETA tip is as follows:

(i) Coupling CDTPA photoinifeter to the p(PETA) surface. This step is to covalently graft CDTPA to the surface of the p(PETA) tip, see Figure 5.3(a). The CDTPA can then initiate a photo-polymerization of MIP on the p(PETA) tip surface in the subsequent step. 10 ml of CDTPA 10 mM solution is prepared by mixing 0.1 mmol of CDTPA in 10 ml of absolute ethanol in a vial. The vial is then sealed with parafilm. The p(PETA) tip attached to the end of the optical fiber

is threaded through a Pasteur pipette (standard 230 mm x 1000) to ensure a complete coverage. The pipette containing the fiber/tip system inside is inserted into the vial, see Figure 5.3(b). At this moment, the tip needs to be kept above the CDTPA solution and a flow of N_2 is gradually introduced to completely degas the solution for 1 h. The tip is then immerged into the CDTPA solution and the whole system is then exposed under a 520-nm LED light at 1.0 mW/cm^2 for 24 h. N_2 is constantly introduced into the solution to minimize the influence of O_2 on the coupling process. After 24 h, the tip covered by the pipette is removed from the solution. The tip is then removed from the pipette and rinsed in ethanol by three times, each lasting 10 min. The tip is finally allowed to dry in the air.

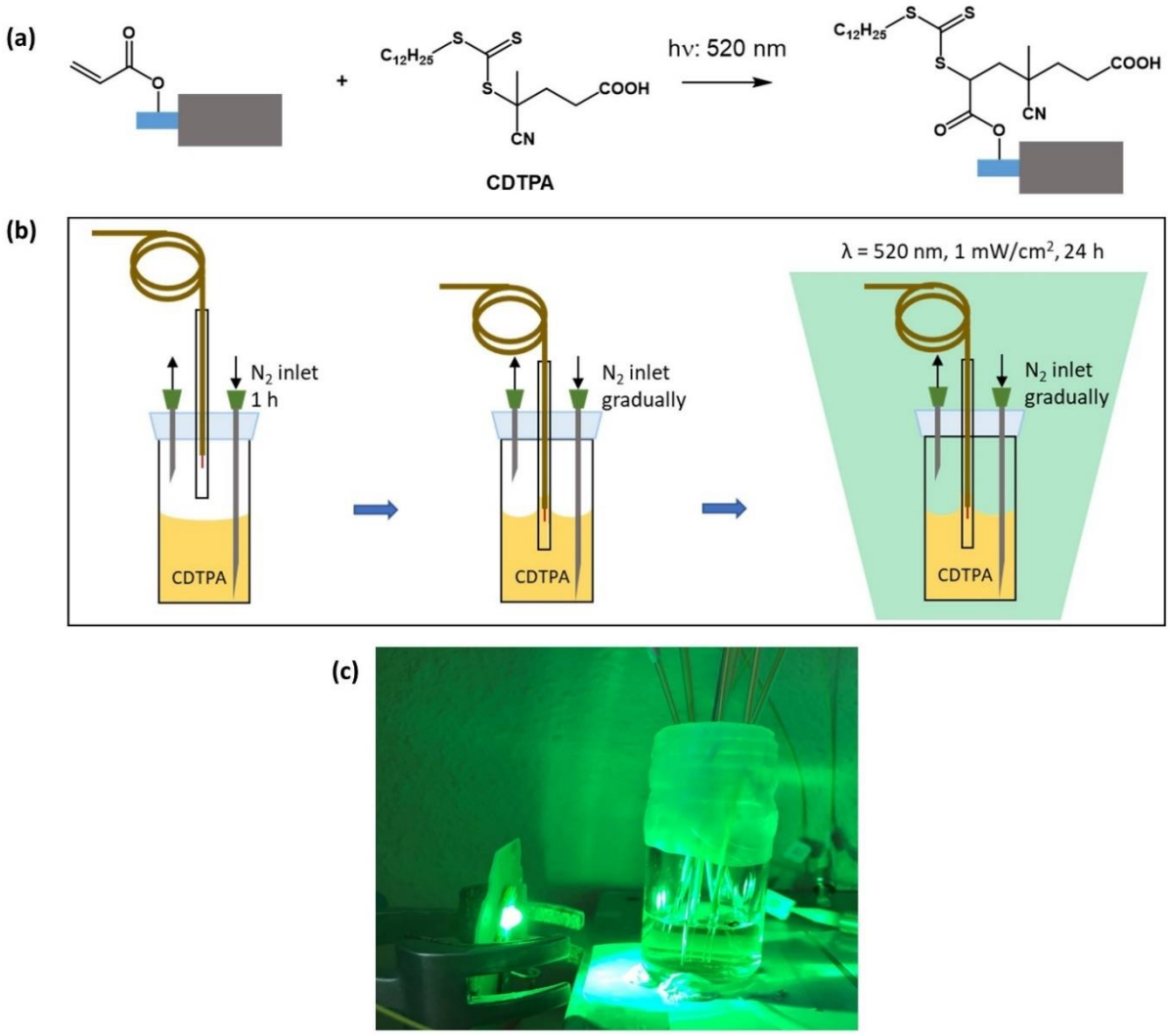

Figure 5. 3. (a) Schematic diagram of the reaction between CDTPA with a residual double-bond in the p(PETA) tip (created by Dr. Ernesto III Paruli - Université de Technologie de Compiègne - GEC Laboratory). (b) Schematic diagram of the experimental setup for coupling CDTPA to the p(PETA) tip. (c) Experimental setup for exposing p(PETA) tips in CDTPA solution to 520 nm LED light.

(ii) Growing a MIP shell. A MIP precursor solution is prepared based on the recipe in [23], [25]. Namely, a mixture of Dansyl-L-Phe (template), MAA and 4-VP (functional monomers) and EGDMA (crosslinker), at a molar ratio of 1/4/4/40 is prepared and then dissolved in acetonitrile to reach a [C=C] concentration of 1.8 M. The tip is covered by the Pasteur pipette again and then inserted into a vial containing the MIP precursor, see Figure 5.4. The tip is kept above the solution and the solution is degassed for 1 h. After that, the tip is fully immerged into the solution and the whole system is exposed to 455-nm LED light at a power of 1 mW/cm^2

for 5 h. Thanks to the CDTPA previously attached to the p(PETA) surface, the MIP is polymerized and forms a shell layer surrounding the p(PETA) tip. To mitigate the influence of O_2 on the photopolymerization of the MIP, N_2 is constantly introduced into the solution during the exposure. After the exposure, the tip is removed from the solution.

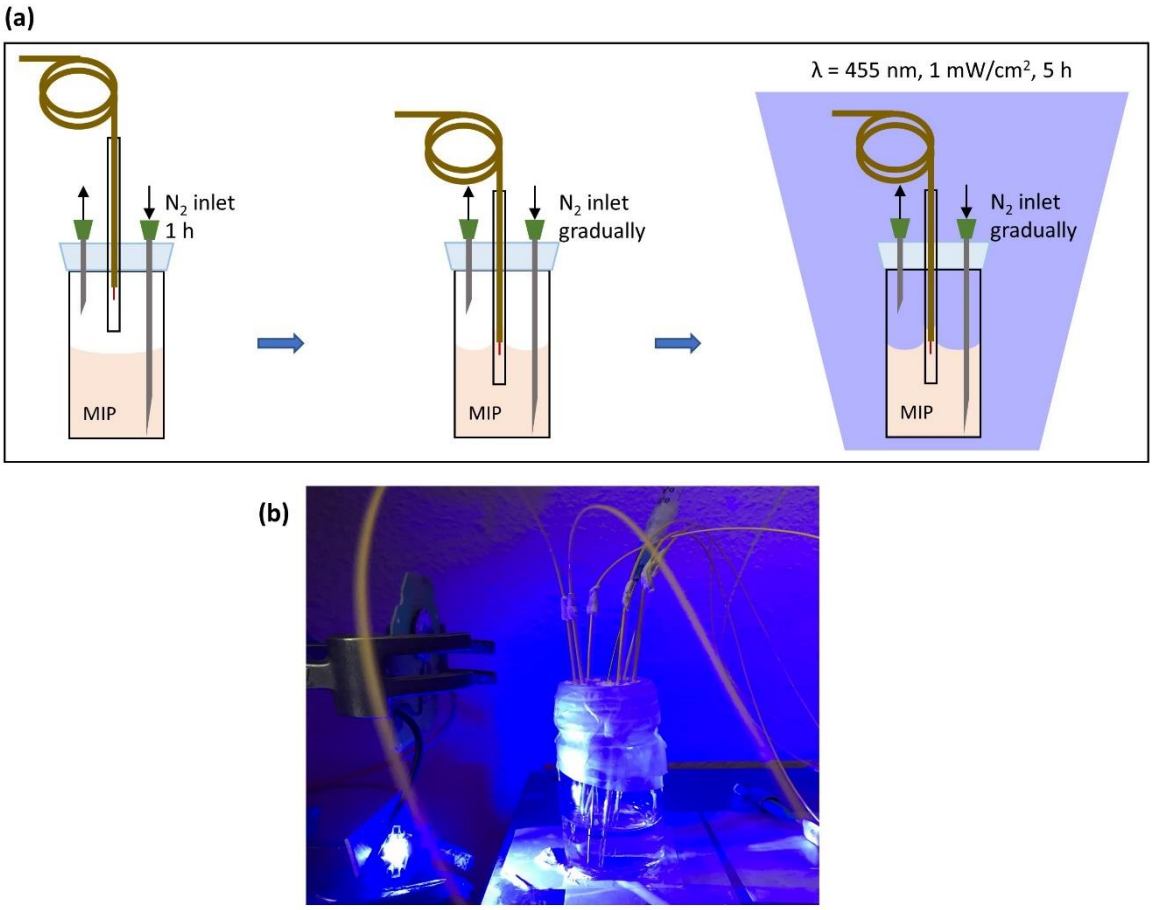

Figure 5. 4. (a) Schematic diagram of the experimental setup for growing MIP layer to the p(PETA) tip. (b) Experimental setup for exposing p(PETA) tips in MIP solution to 455 nm LED light.

In the experiment above, we selected Dansyl-L-Phe as the template for the formulation of the MIP. This is because Dansyl-L-Phe exhibits a strong fluorescent property, so we can use a fluorescence microscope (Leica DM6000B, with a A4 filter cube, excitation BP 360/40, emission BP 470/40) to prove the formation of a MIP layer surrounding the p(PETA) tip, see Figure 5.5. From bright-field microscopy images, one cannot observe any difference between p(PETA) tip and p(PETA)/MIP tip because the MIP shell is expected to be very thin as compared to the PETA core diameter. However, the fluorescence images show a clear difference

between them. The initial p(PETA) tip does not exhibit any fluorescence while the p(PETA)/MIP tip exhibits a strong fluorescence. This indicates that a layer of MIP is successfully formed surrounding the p(PETA) core. An observation by a high-resolution electron scanning microscope would be helpful to precisely determine the thickness of the MIP layer.

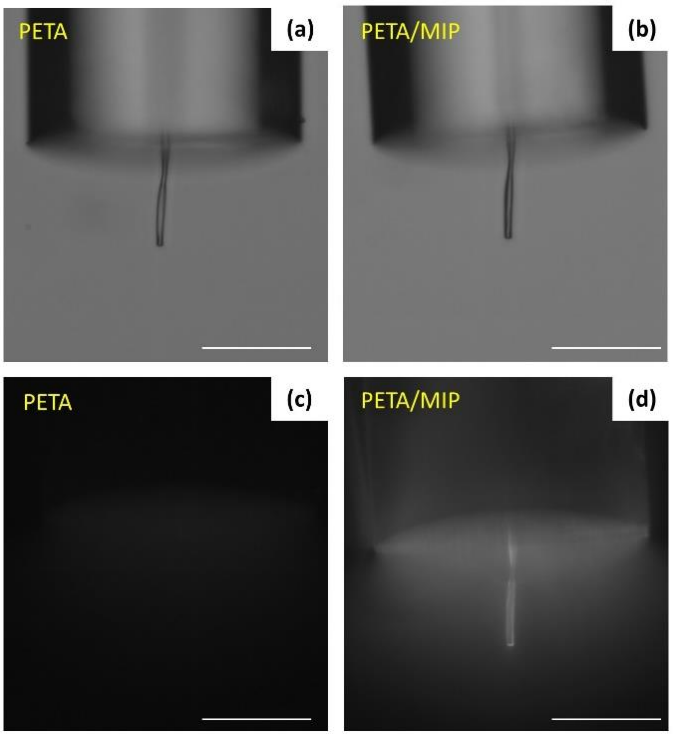

Figure 5. 5. Brightfield (a) and fluorescence microscopy images (c) of p(PETA) tip. Brightfield (b) and fluorescence microscope image (d) of tip consisting of p(PETA) core-MIP shell with Dansyl-L-Phe as template. Scale bar = 50 µm.

We apply the steps above to form a p(PETA)/MIP tip with the MIP shell layer contains Z-L-Phe template. The Z-L-Phe has an analogous structure with the Dansyl-L-Phe but it is a non-fluorescent material. We therefore believe that a MIP layer using Z-L-Phe template is also successfully synthesized, even though we are unable to experimentally observe it by the fluorescent microscope. The use of Z-L-Phe template will help us to evaluate the sensing performance of the MIP for fluorescent analytes, as presented later in this chapter. The p(PETA)/MIP tip in the following sections is formulated with the Z-L-Phe template.

(iii) Extracting the template: The p(PETA)/MIP tip after the step (ii) is washed in methanol/acetic acid (vol. ratio = 8/2) for 2 h, followed in ethanol for 1 h and finally in

methanol for 30 min to remove the Z-L-Phe template. The p(PETA)/MIP tip now possesses binding sites that can detect analytes which have a similar structure and functional groups to Z-L-Phe. We record the FPI signal of the tip before and after the template exaction, see Figure 5.6. It is seen that the FPI signal of a 57.3-µm long p(PETA)/MIP tip shifts towards shorter wavelength by 3.07 nm after the template extraction.

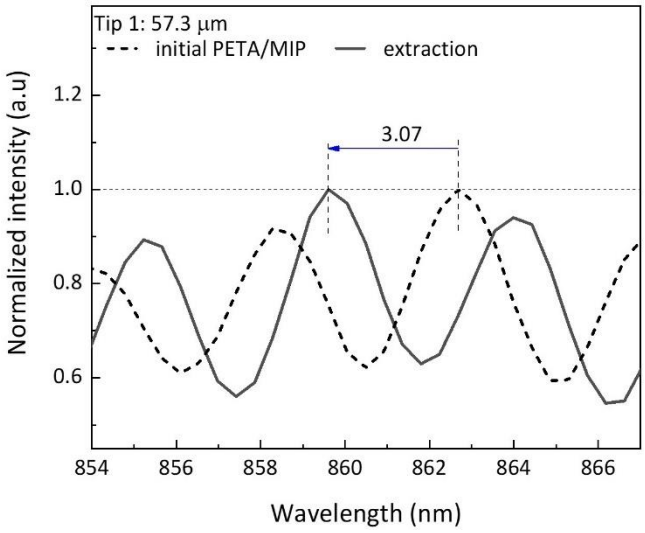

Figure 5. 6. FPI spectra of 57.3 µm-long tip before and after extraction of the template Z-L-Phe.

5.5. Application of the p(PETA)/MIP tip for detecting Dansyl-L-Phe

The p(PETA)/MIP tip with Z-L-Phe template removed from the MIP layer is now used for detecting Dansyl-L-Phe in liquid media. The Dansyl-L-Phe analyte has been chosen to enable a comparison between FPI measurements and fluorescence measurements. A stock solution of Dansyl-L-Phe 1 mM is prepared in acetonitrile solvent. Lower concentrated solutions can be then obtained by adding an appropriate amount of acetonitrile to the stock solution. The FPI signal of the tip is firstly recorded in the air by the setup which was already described in previous chapters. The tip is then immersed in the Dansyl-L-Phe solution for 2 h and then dried in the air for another 2 h. The FPI signal of the tip is recorded and compared with the one measured before binding, see Figure 5.7. The relative humidity in the air is constantly maintained at 40 % to prevent the influence of humidity on the FPI signal of the tip.

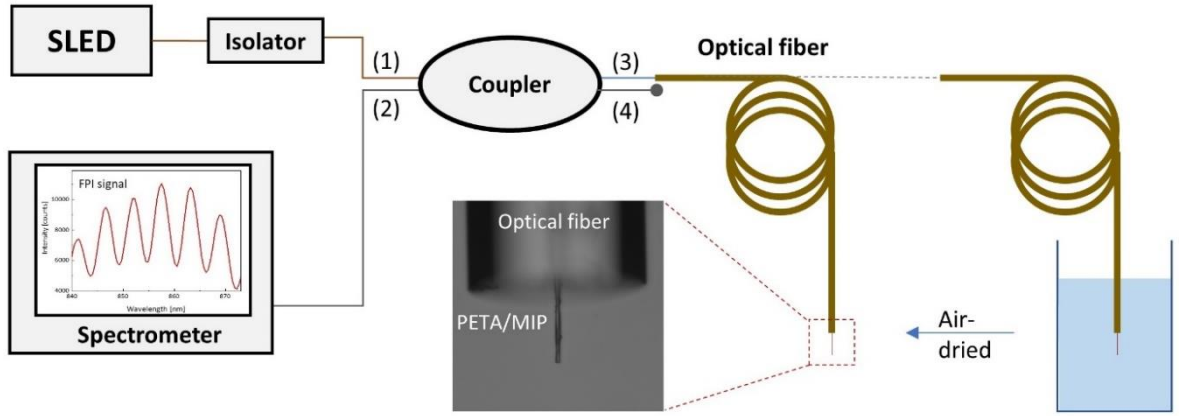

Figure 5. 7. Schematic diagram of the experimental setup for measuring FPI signal of polymer tips in liquid environments.

In addition to tracking the FPI signal of the tip upon binding with analytes, we also characterized the fluorescence of the tip by the fluorescence microscope with a similar power light source and integration time for all the measurements. The intensity of fluorescence on the tip is quantified by processing the microscopy images through ImageJ software. Then, the calculated fluorescence intensity is corrected for background noise using the following formula:

$$CTCF = integrated\ density - (selected\ area \times mean\ fluorescence\ of\ background)$$

where CTCF represents the background-corrected fluorescence intensity. The CTCF is considered as the response of the p(PETA)/MIP tip to the Dansyl-L-Phe target.

5.6. Result and discussions

5.6.1. FPI response of p(PETA)/MIP tips upon binding to Dansyl-L-Phe

The p(PETA)/MIP tip, after removing the template, is dipped into solutions of various Dansyl-L-Phe concentrations. After the binding between MIP and Dansyl-L-Phe, the tip is dried and its FPI signals are recorded, see Figure 5.8. It is seen that the FPI signal of the 57.3 μm-long tip after binding in the 50 μM solution remains unchanged compared to its state before binding. When the concentration of Dansyl-L-Phe increases to 75 μM, the FPI signal of the tip shifts slightly towards longer wavelength. Further increases in Dansyl-L-Phe concentration leads to a continuous red shift in the FPI signal of the tip. A total shift of 1.75 nm is obtained after immersing the p(PETA)/MIP tip in the Dansyl-L-Phe 1000 μM solution, see Figure 5.8(a). These observations are consistent across other tips with different lengths, see Figure 5.8(b-d). The minimum concentration of Dansyl-L-Phe for an observable FPI shift is 75 μM, which is considered as the limit of detection of the p(PETA)/MIP tip. It is also noted that the red shift resulted from the analyte binding is consistently smaller than the blue shift resulted from the template extraction.

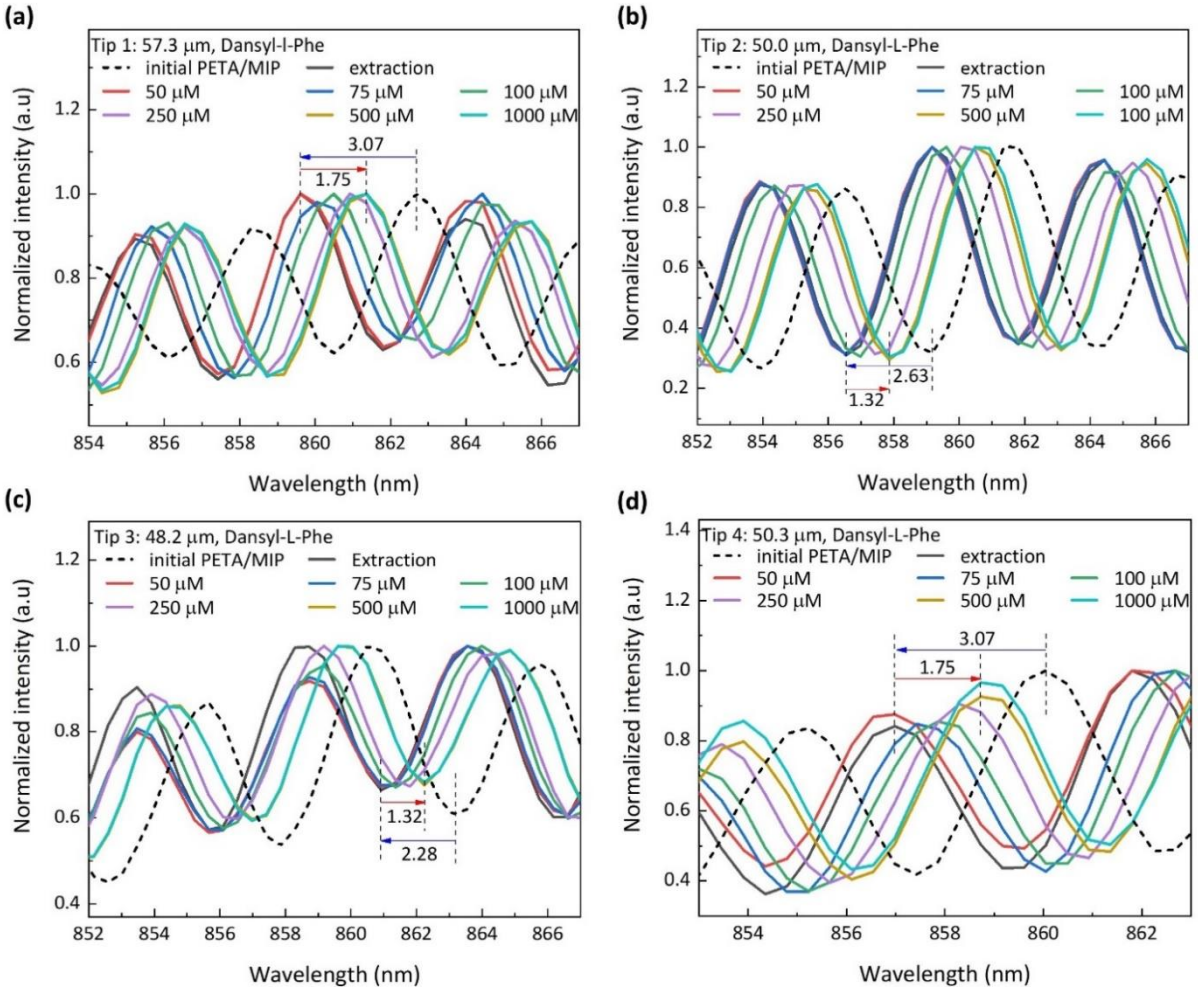

Figure 5. 8. FPI spectra of the p(PETA)/MIP tips with a length of (a) 57.3 µm, (b) 50 µm, (c) 48.2 µm and (d) 50.3 µm after binding process with different Dansyl-L-Phe solutions.

The FPI wavelength shift as a function of the Dansyl-L-Phe concentration is shown in Figure 5.9. It is seen that the FPI shift follows a non-linear dependence on analyte concentration. The data are fitted to a simple single-site Langmuir adsorption isotherm [27]. Indeed, the interaction between the analyte and the free binding sites within the MIP layer can be expressed as follows:

$$A + S \underset{k_d}{\overset{k_a}{\longleftrightarrow}} AS \tag{5.1}$$

where A denotes the analyte, S denotes the free binding sites within the MIP layer, AS denotes the complex formed by the binding between the analyte and site, k_a and k_d refer to the first-order rate constant for the absorption (association) and desorption (dissociation)

process, respectively. The corresponding overall rate of the binding process can be then described as follows:

$$\frac{d[AS]}{dt} = k_a[A][S] - k_d[AS] \tag{5.2}$$

where square-brackets indicate the concentration value. The concentration of the complex $[AS]$ can be substituted with the uptake B which indicates the measured wavelength shift of the FPI signal of polymer tip as immersing in the analyte solution with concentration $[A]$ in our case. Additionally, the concentration of free sites $[S]$ can be substituted with the difference between the maximum equilibrium adsorption capacity B_{max} and the uptake B. Here B_{max} indicates the largest obtainable wavelength shift. Therefore, the equation (5.2) becomes:

$$\frac{dB}{dt} = k_a[A](B_{max} - B) - k_d B \tag{5.3}$$

$$\Leftrightarrow \frac{dB}{dt} = k_a[A]B_{max} - (k_a[A] + k_d)B \tag{5.4}$$

When the interaction between the analyte and free sites in the MIP reaches the equilibrium, $\frac{dB}{dt} = 0$, resulting:

$$B = \frac{B_{max}k_a[A]}{k_d + k_a[A]} = \frac{B_{max}[A]}{K_d + [A]} \tag{5.5}$$

where $K_d = \frac{k_d}{k_a}$ is the equilibrium dissociation constant.

Therefore, the experimental data are fitted by a Langmuir adsorption isotherm represented by the equation (5.5). From the Langmuir isotherm fitting, the 57.3-µm long polymer tip has a dissociation constant of 243 µM and a maximum theoretically achievable wavelength shift of 2.36 nm, see Table 5.1. It is seen that although similar trends are observed among different tips, the extent of FPI shifts varies, indicating that each tip has its own sensing potential with diverse maximum binding capacities and dissociation coefficients.

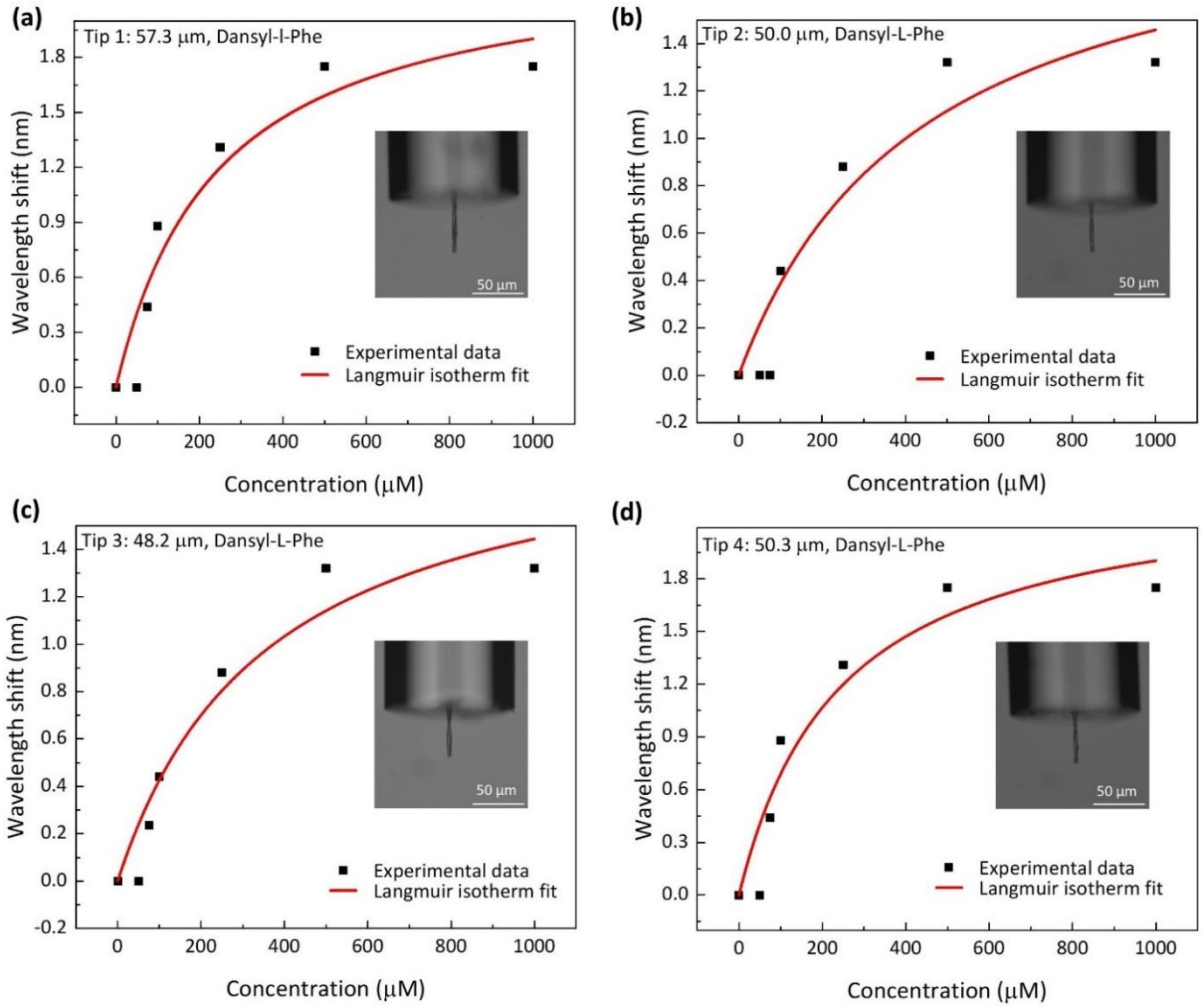

Figure 5. 9. The dependence of FPI wavelength position of different polymer tips with a length of (a) 57.3 µm, (b) 50 µm, (c) 48.2 µm and (d) 50.3 µm on Dansyl-L-Phe concentration.

Table 5. 1. Langmuir adsorption isotherm model calculated for FPI signals of different tips

Sensor	Length (µm)	Maximum binding capacity B_{max} (nm)	Equilibrium dissociation coefficient K_d (µM)	Coefficient of determination (R^2)
Tip 1	57.3	2.36	243	0.92
Tip 2	50.0	2.10	443	0.90
Tip 3	48.2	1.97	362	0.94
Tip 4	50.3	2.36	243	0.92

The wavelength shifts in the FPI signal observed above are attributed to the changes of the refractive index of the MIP layer upon template extraction or analyte binding process. The core-shell structured p(PETA)/MIP tip forms two optical cavities in series, made up of three parallel reflecting surfaces: the fiber-core/p(PETA) interface, p(PETA)/MIP interface, and MIP/air interface. Upon the template extraction or analyte binding, the length and refractive index of the p(PETA) tip core are believed to remain unchanged. It is expected that only the refractive index of the MIP layer experiences a considerable change upon these processes. In particularly, upon the extraction of the Z-L-Phe template, the MIP matrix becomes less dense because of available binding sites, its refractive index therefore decreases, resulting in a blue shift of FPI signal, as observed in Figure 5.6 and Figure 5.8. When the tip is incubated in the Dansyl-L-Phe solution, the analyte fills in the empty binding sites of the MIP matrix, thus increasing the refractive index of the MIP layer, leading to a red shift in the FPI signal of the tip, as shown in Figure 5.8. If the analyte concentration is too low, the binding is insignificant and the change of the refractive index is insufficient to cause an observable FPI signal shift. As the analyte concentration increases, the binding between the MIP and analyte is significant, resulting in a considerable change in the polymer refractive index and an observable FPI red shift. It should be noted that the FPI signal is measured when the tip is in the air with a constant humidity of 40 %, so the impact of humidity is eliminated.

Although the tips exhibit a consistent red shift in the FPI signal upon binding to target analyte solutions, the extent of the shift is clearly different from tip to tip. This result might be originated from several reasons. First, the properties of the p(PETA) cores are not well controlled because the photopolymerization of p(PETA) takes place in the ambient with O_2 presence and the tips are not accompanied by a post-polymerization. Second, the growth of the MIP on different p(PETA) tips may significantly vary between experiment to experiment, although we attempt to do it in an O_2-free environment. However, our data still show that MIP-based FPI sensors are promising for label-free detecting Dansyl-L-Phe.

5.6.2. Fluorescence of p(PETA)/MIP tips upon binding to Dansyl-L-Phe

The p(PETA)/MIP tip, using a Z-L-Phe template, does not exhibit fluorescence whereas Dansyl-L-Phe target exhibits strong fluorescence. Hence, the binding of the MIP layer with Dansyl-L-

Phe can be analyzed based on the tip fluorescence intensity. Figure 5.10 shows the fluorescence microscopy images of the tips taken before and after binding with various Dansyl-L-Phe solutions. As expected, the tips before binding tests exhibit no fluorescence. After being exposed to the 50-μM Dansyl-L-Phe solution, the tips do not exhibit fluorescence. However, they exhibit strong fluorescence after being exposed to the solutions with Dansyl-L-Phe concentration of 75 μM and above. The fluorescence intensity increases with increasing concentration of Dansyl-L-Phe in the solution. These observations are consistent across all tips.

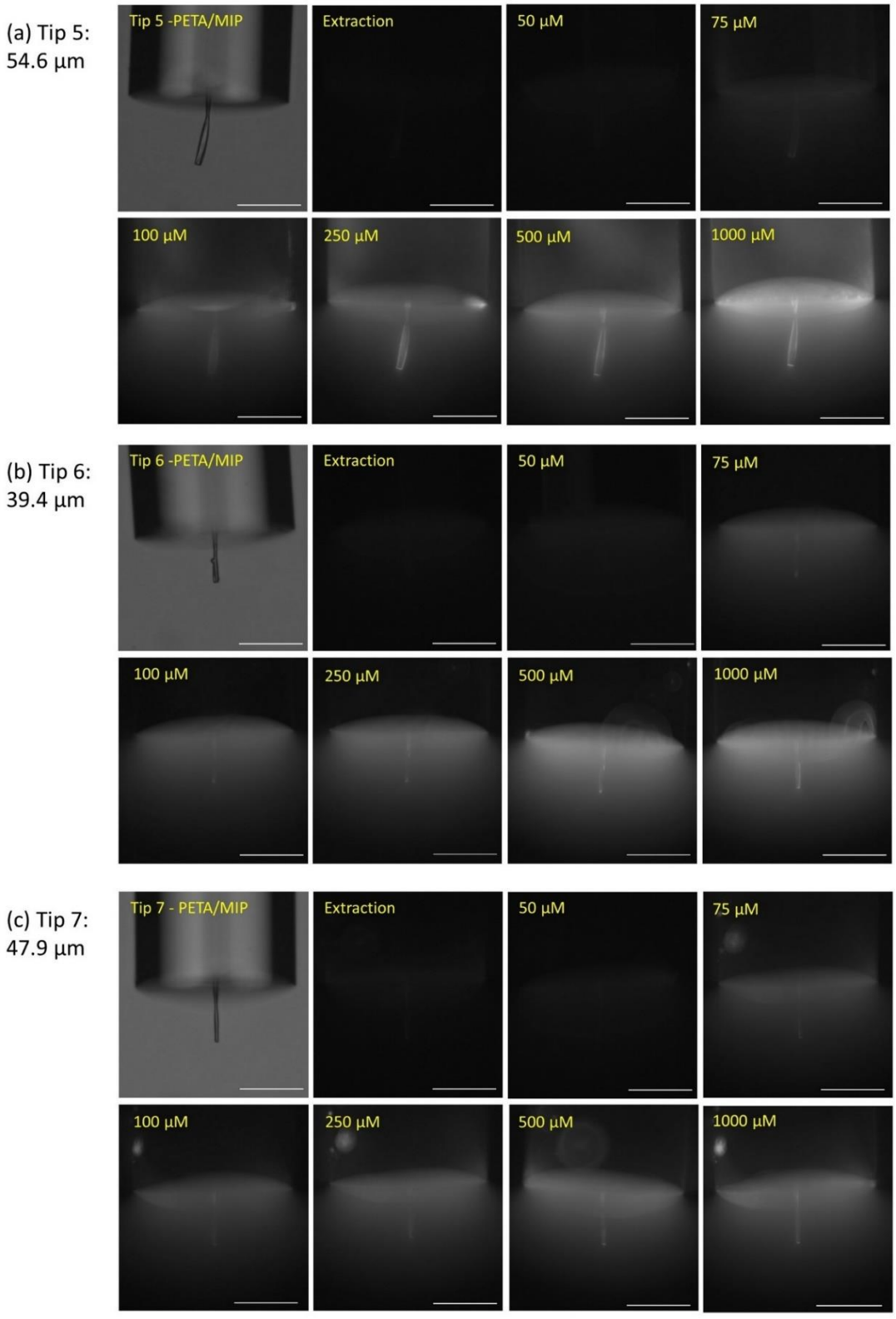

Figure 5. 10. Brightfield image at initial state, and fluorescence images after extraction process and after rebinding process with various Dansyl-L-Phe concentrations of a tip with a length of (a) 54.6 µm, (b) 39.4 µm and (c) 47.9 µm. The scale bar is 50 µm.

The background-corrected fluorescence intensities of the tips after binding to various Dansyl-L-Phe solutions are calculated using the ImageJ software and shown in Figure 5.11. The quantitative data confirm that the fluorescence intensity of the tip increases with increasing Dansyl-L-Phe concentration. Moreover, one can fit the fluorescence of the tip following the Langmuir isotherm model. A 54.6 µm long tip exhibits a theoretically maximum fluorescence intensity of about 39000 a.u. with a dissociation coefficient of 444 µM. All the tips displayed a similar response tendency to various analyte concentrations; however, maximum binding capacities and dissociation coefficients are found differently between them, see Table 5.2.

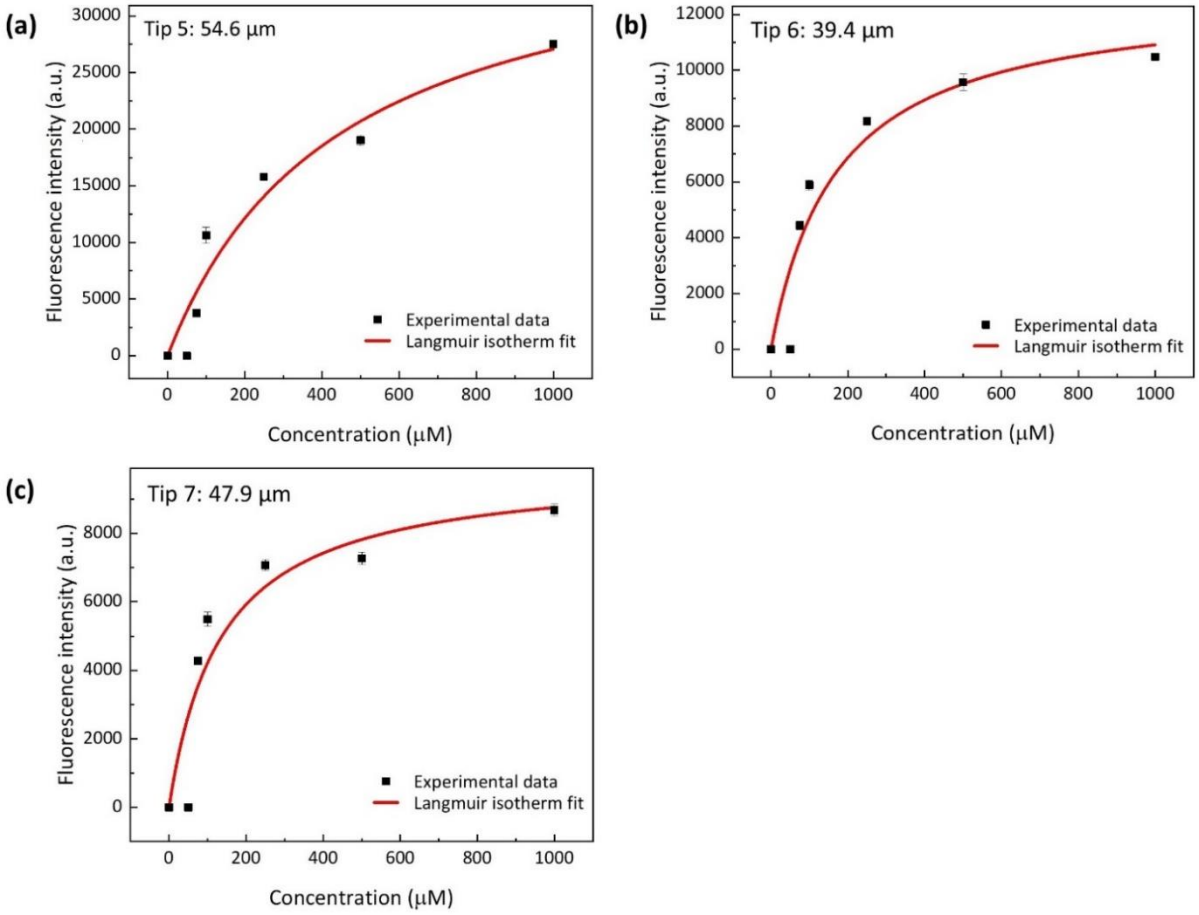

Figure 5. 11. The dependence of background-corrected fluorescence intensity of a (a) 54.6-µm-long tip, (b) 39.4-µm-long tip and (c) 47.9-µm-long tip on Dansyl-L-Phe concentration.

Table 5. 2. Langmuir adsorption isotherm model calculated for fluorescence intensity emitted from different tips

Sensor	Length (µm)	Maximum binding capacity B_{max} (a.u.)	Equilibrium dissociation coefficient K_d (µM)	Coefficient of determination (R^2)
Tip 5	54.6	39087	444	0.94
Tip 6	39.4	12790	173	0.90
Tip 7	47.9	9943	136	0.86

In a nutshell, we also can examine the detection of Dansyl-L-Phe by study the fluorescence of the p(PETA)/MIP tip. The tip exhibits no fluorescence when being incubated in a Dansyl-L-Phe solution of 50 µM, but starts to show fluorescence when being incubated in a solution of 75 µM. The fluorescence then increases with further increasing Dansyl-L-Phe concentration. This behavior is consistent with the observations from the FPI signal presented above. However, different tips also show different fluorescent intensity for a given Dansyl-L-Phe concentration. This again implies that the quality of our p(PETA)/MIP tips are not well controlled. The change of the fluorescence with the Dansyl-L-Phe concentration fits well with the Langmuir isotherm model. Based on the fluorescence properties of the tip, we estimate the limit of detection of our sensor at 75 µM. This result is consistent with the result obtained from the FPI response, as previously shown in section 5.6.1. By the way, it shows the good sensitivity of the label-free FPI sensor as the limit of detection is the same as for fluorescence spectroscopy.

5.6.3. Binding selectivity of p(PETA)/MIP tip

In the previous sections, we demonstrated that the p(PETA)/MIP tip, using Z-L-Phe template, can work as an FPI sensor for Dansyl-L-Phe, which shares a similar structure with Z-L-Phe. It is well known that MIPs only bind to target analytes with a structure similar to their formulation template, thus revealing a strong selectivity of MIP-based sensors. Here, we investigate whether the strong selectivity of the p(PETA)/MIP tip sensor can be indicated by its FPI signal.

We test the p(PETA)/MIP tip with solutions of Z-D-Phe, an analyte with a structure different from that of Z-L-Phe. The MIP layer does not bind to Z-D-Phe, so we expect that the FPI signal of the tip is unchanged upon the testing. The experiment procedure is similar to that for Dansyl-L-Phe, the tip is immersed in the Z-D-Phe solution for 2 h and then dried in the air for 2 h. Their FPI signal is then taken and shown in Figure 5.12. One can see clearly that the FPI signal of the tip is almost constant in the wavelength position even after the tip is exposed to the solution of 1000 μM Z-D-Phe. The observation is consistent across all tips. The dependence of FPI wavelength position of different polymer tips on Z-D-Phe concentration is shown in Figure 5.13(a). Compared to the detection of Dansyl-L-Phe shown in Figure 5.13(b), we can conclude that our fiber optic FPI chemical sensor based on a p(PETA)/MIP tip exhibit a high selectivity. Furthermore, this experiment also confirms that in the sensing test of MIPs for template-analogous analyte solutions (such as Dansyl-L-Phe), the analyte molecules fill in the binding sites within the MIP matrix rather than graft non-specifically on the MIP surface.

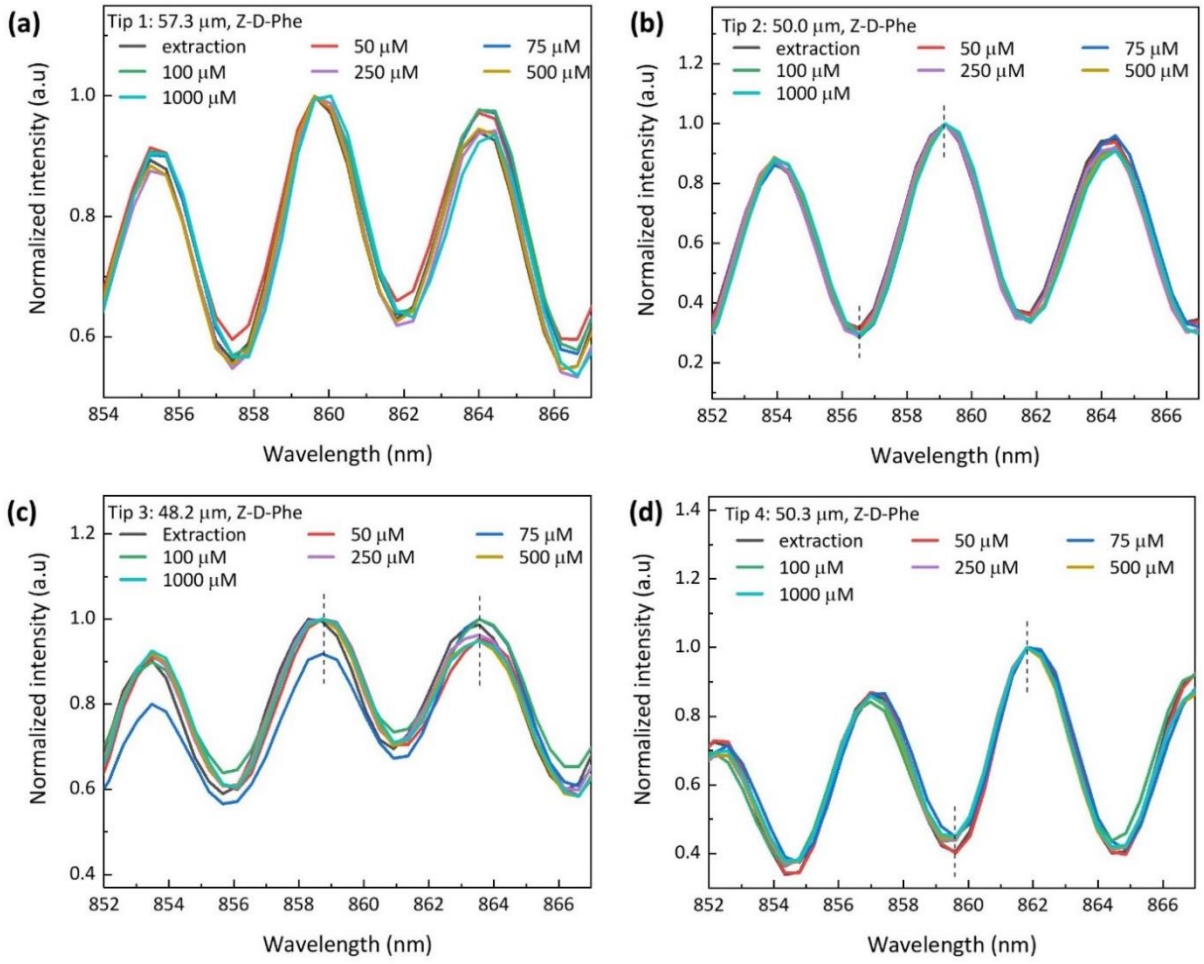

Figure 5. 12. FPI spectra of polymer tips with a length of (a) 57.3 µm, (b) 50 µm, (c) 48.2 µm and (d) 50.3 µm after binding process with Z-D-Phe.

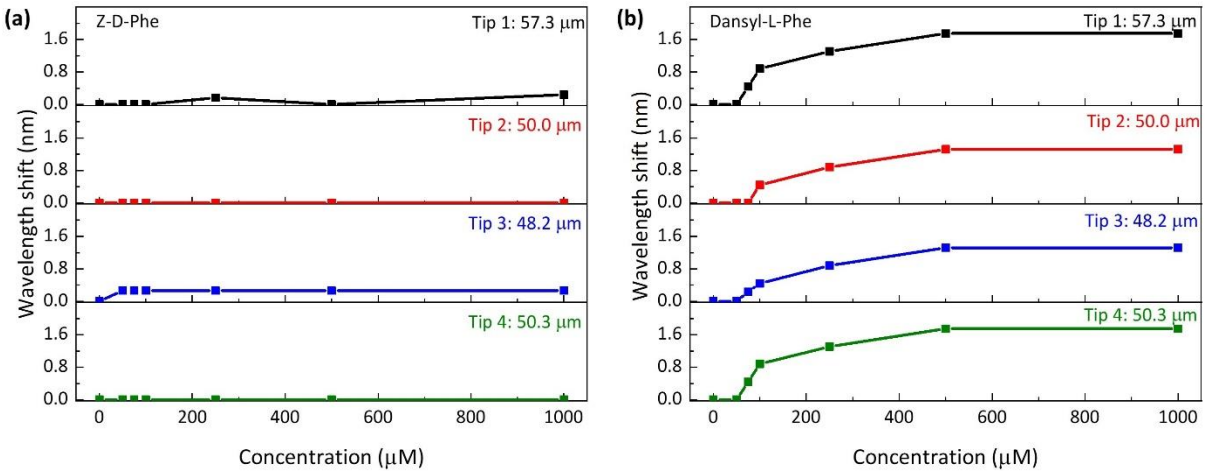

Figure 5. 13. The dependence of FPI wavelength position of different polymer tips on (a) Z-D-Phe concentration and (b) Dansyl-L-Phe concentration.

5.7. Conclusion

In this chapter, we have presented the development of a fiber optic FPI sensor based on MIP for detecting Dansyl-L-Phe amino acid. The sensor comprises a MIP layer coated on a p(PETA) core tip which is attached to the end of an optical fiber. The p(PETA) tip is initially fabricated by self-guiding polymerization without a post-polymerization process. The MIP layer, using a Z-L-Phe template, is then formed on the surface of the p(PETA) tip by photopolymerization. The final p(PETA)/MIP core-shell structure exhibits a clear FPI signal that is sensitive to binding between the MIP layer and Dansyl-L-Phe. The sensing response based on the FPI method is consistent with that based on the fluorescence method. The use of FPI signal appears to be more straightforward compared to the use of fluorescence. The limit of detection for Dansyl-L-Phe by the p(PETA)/MIP tip is 75 µM. Moreover, the FPI response remains almost constant in the wavelength position when the tip is tested in analytes that possess a non-analogous structure to the Z-L-Phe template. This implies that the p(PETA)/MIP sensor based on the FPI method also displays a high selectivity. All of these findings suggest that our MIP-based fiber optic FPI is a promising sensor for various analytes, irrespective of their fluorescence.

References

[1] K. Haupt, A.V. Linares, M. Bompart, and B. Tse Sum Bui, 'Molecularly Imprinted Polymers', Top. Curr. Chem., vol. 325, pp. 1–28, 2012, doi: 10.1007/128_2011_307.

[2] K. Haupt, P. X. Medina Rangel, and B. Tse Sum Bui, 'Molecularly imprinted polymers: Antibody mimics for bioimaging and therapy', Chem. Rev., vol. 120, pp. 9554–9582, Sep. 2020, doi: 10.1021/acs.chemrev.0c00428.

[3] P. Luliński, 'Molecularly imprinted polymers based drug delivery devices: a way to application in modern pharmacotherapy. A review', *Materials Science and Engineering: C*, vol. 76, pp. 1344–1353, Jul. 2017, doi: 10.1016/j.msec.2017.02.138.

[4] S. Nestora, F. Merlier, S. Beyazit, E. Prost, L. Duma, B. Beril. A. Greaves, K. Haupt, and B. Tse Sum Bui, 'Plastic Antibodies for Cosmetics: Molecularly Imprinted Polymers Scavenge

Precursors of Malodors', *Angew Chem Int Ed*, vol. 55, no. 21, pp. 6252–6256, May 2016, doi: 10.1002/anie.201602076.

[5] S. Mohamed, S. Balieu, E. Petit, L. Galas, D. Schapman, J. Hardouin, R. Baati, and F. Estour, 'A versatile and recyclable molecularly imprinted polymer as an oxidative catalyst of sulfur derivatives: a new possible method for mustard gas and V nerve agent decontamination', *Chem. Commun.*, vol. 55, no. 88, pp. 13243–13246, 2019, doi: 10.1039/C9CC04928B.

[6] D. Mathew, B. Thomas, and K. S. Devaky, 'Design, synthesis and characterization of enzyme-analogue-built polymer catalysts as artificial hydrolases', *Artificial Cells, Nanomedicine, and Biotechnology*, vol. 47, no. 1, pp. 1149–1172, Dec. 2019, doi: 10.1080/21691401.2019.1576703.

[7] L. Uzun and P. F. T. Anthony, 'Molecularly-imprinted polymer sensors: realising their potential', *Biosensors and Bioelectronics*, vol. 76, pp. 131–144, 2016, doi: 10.1016/j.bios.2015.07.013.

[8] N. Leibl, K. Haupt, C. Gonzato, and L. Duma, 'Molecularly Imprinted Polymers for Chemical Sensing: A Tutorial Review', *Chemosensors*, vol. 9, no. 6, p. 123, May 2021, doi: 10.3390/chemosensors9060123.

[9] M. Loyez, M. C. DeRosa, C. Caucheteur, and R. Wattiez, 'Overview and emerging trends in optical fiber aptasensing', *Biosensors and Bioelectronics*, vol. 196, p. 113694, Jan. 2022, doi: 10.1016/j.bios.2021.113694.

[10] A. L. Jenkins, R. Yin, and J. L. Jensen, 'Molecularly imprinted polymer sensors for pesticide and insecticide detection in water', *Analyst*, vol. 126, no. 6, pp. 798–802, 2001, doi: 10.1039/b008853f.

[11] T. H. Nguyen, S. A. Hardwick, T. Sun, and K. T. V. Grattan, 'Intrinsic Fluorescence-Based Optical Fiber Sensor for Cocaine Using a Molecularly Imprinted Polymer as the Recognition Element', *IEEE Sensors J.*, vol. 12, no. 1, pp. 255–260, Jan. 2012, doi: 10.1109/JSEN.2011.2158537.

[12] X. Ton, B. Tse Sum Bui, M. Resmini, P. Bonomi, I. Dika, O. Soppera, and K. Haupt, 'A Versatile Fiber-Optic Fluorescence Sensor Based on Molecularly Imprinted Microstructures Polymerized in Situ', *Angewandte Chemie*, vol. 125, no. 32, pp. 8475–8479, Aug. 2013, doi: 10.1002/ange.201301045.

[13] S. Carrasco, E. Benito-Peña, D. R. Walt, and M. C. Moreno-Bondi, 'Fiber-optic array using molecularly imprinted microspheres for antibiotic analysis', *Chem. Sci.*, vol. 6, no. 5, pp. 3139–3147, 2015, doi: 10.1039/C5SC00115C.

[14] Q.-D. Huang, C.-H. Lv, X.-L. Yuan, M. He, J.-P. Lai, and H. Sun, 'A novel fluorescent optical fiber sensor for highly selective detection of antibiotic ciprofloxacin based on replaceable molecularly imprinted nanoparticles composite hydrogel detector', *Sensors and Actuators B: Chemical*, vol. 328, p. 129000, Feb. 2021, doi: 10.1016/j.snb.2020.129000.

[15] R. Verma and B. D. Gupta, 'Fiber optic SPR sensor for the detection of 3-pyridinecarboxamide (vitamin B3) using molecularly imprinted hydrogel', *Sensors and Actuators B: Chemical*, vol. 177, pp. 279–285, Feb. 2013, doi: 10.1016/j.snb.2012.10.135.

[16] A. M. Shrivastav, S. K. Mishra, and B. D. Gupta, 'Fiber optic SPR sensor for the detection of melamine using molecular imprinting', *Sensors and Actuators B: Chemical*, vol. 212, pp. 404–410, Jun. 2015, doi: 10.1016/j.snb.2015.02.028.

[17] A. M. Shrivastav, S. P. Usha, and B. D. Gupta, 'Highly sensitive and selective erythromycin nanosensor employing fiber optic SPR/ERY imprinted nanostructure: Application in milk and honey', *Biosensors and Bioelectronics*, vol. 90, pp. 516–524, Apr. 2017, doi: 10.1016/j.bios.2016.10.041.

[18] H. Agrawal, A. M. Shrivastav, and B. D. Gupta, 'Surface plasmon resonance based optical fiber sensor for atrazine detection using molecular imprinting technique', *Sensors and Actuators B: Chemical*, vol. 227, pp. 204–211, May 2016, doi: 10.1016/j.snb.2015.12.047.

[19] A. Pathak and B. D. Gupta, 'Ultra-selective fiber optic SPR platform for the sensing of dopamine in synthetic cerebrospinal fluid incorporating permselective nafion membrane and surface imprinted MWCNTs-PPy matrix', *Biosensors and Bioelectronics*, vol. 133, pp. 205–214, May 2019, doi: 10.1016/j.bios.2019.03.023.

[20] N. Cennamo, G. D'Agostino, M. Pesavento, and L. Zeni, 'High selectivity and sensitivity sensor based on MIP and SPR in tapered plastic optical fibers for the detection of l-nicotine', *Sensors and Actuators B: Chemical*, vol. 191, pp. 529–536, Feb. 2014, doi: 10.1016/j.snb.2013.10.067.

[21] N. Cennamo, A. Donà, P. Pallavicini, G. D'Agostino, G. Dacarro, L. Zeni, and K. Pesavento, 'Sensitive detection of 2,4,6-trinitrotoluene by tridimensional monitoring of molecularly imprinted polymer with optical fiber and five-branched gold nanostars', *Sensors and Actuators B: Chemical*, vol. 208, pp. 291–298, Mar. 2015, doi: 10.1016/j.snb.2014.10.079.

[22] R. B. Queirós, S. O. Silva, J. P. Noronha, O. Frazão, P. Jorge, G. Aguilar, P. V. S. Marques, and M. G. F. Sales, 'Microcystin-LR detection in water by the Fabry–Pérot interferometer using an optical fibre coated with a sol–gel imprinted sensing membrane', *Biosensors and Bioelectronics*, vol. 26, no. 9, pp. 3932–3937, May 2011, doi: 10.1016/j.bios.2011.03.015.

[23] Y. Fuchs, A. V. Linares, A. G. Mayes, K. Haupt, and O. Soppera, 'Ultrathin Selective Molecularly Imprinted Polymer Microdots Obtained by Evanescent Wave Photopolymerization', *Chem. Mater.*, vol. 23, no. 16, pp. 3645–3651, Aug. 2011, doi: 10.1021/cm2009829.

[24] E. I. Paruli, O. Soppera, K. Haupt, and C. Gonzato, 'Photopolymerization and Photostructuring of Molecularly Imprinted Polymers', *ACS Appl. Polym. Mater.*, vol. 3, no. 10, pp. 4769–4790, Oct. 2021, doi: 10.1021/acsapm.1c00661.

[25] E. I. Paruli, V. Montagna, M. García-Soto, K. Haupt, and C. Gonzato, 'A general photoiniferter approach to the surface functionalization of acrylic and methacrylic structures written by two-photon stereolithography', *Nanoscale*, vol. 15, no. 6, pp. 2860–2870, 2023, doi: 10.1039/D2NR06627K.

[26] M. J. Garcia-Soto, K. Haupt, and C. Gonzato, 'Synthesis of molecularly imprinted polymers by photo-iniferter polymerization under visible light', *Polym. Chem.*, vol. 8, no. 33, pp. 4830–4834, 2017, doi: 10.1039/C7PY01113J.

[27] X. Li, and S. M. Husson, 'Adsorption of dansylated amino acids on molecularly imprinted surfaces: A surface plasmon resonance study', *Biosensors and Bioelectronics*, vol. 22, no. 3, pp. 336–348, Sep. 2006, doi: 10.1016/j.bios.2006.04.016.

Chapter 6

Conclusions and perspectives

6.1. Conclusions

Fabry−Perot interferometers (FPI) comprise of an optical cavity with two separate parallel surfaces which reflect incident light, resulting in an optical interferometric signal. The FPI signal depends on the distance between the reflecting surfaces and the refractive index of the cavity medium. These characteristics of the FPI can be changed by variations of environmental conditions such as humidity, temperature, pressure, and material concentration. Based on this principle, FPI can function as a sensor for the detection of various physical and chemical parameters. FPI are commonly attached to optical fibers to form compact fiber optic FPI-based sensors in which the optical fiber works as a waveguide for both incident and reflected signals. The fiber optic FPI-based sensors have a small size and display high efficiency as well as electromagnetic immunity. There have been already various designs and configurations of fiber optic FPI-based sensors in the literature. However, the available configurations are sometimes rather complicated to process, require specific skill and expensive equipment. Moreover, the potential of fiber optic FPI for the detection of chemical products in liquid media has not been statistically exploited in previous studies. This thesis therefore aims to design a simple fiber optic FPI sensor by formulating a polymer tip located at the end of an optical fiber and exploit its application as a sensor for multiple chemical products including humidity, water, and chemical targets.

Firstly, we have formulated a micro-length polymer tip made of pentaerythritol triacrylate (PETA) on the facet of an optical fiber by a self-guiding photopolymerization. One end of the optical fiber is placed inside a PETA droplet and the other end is connected to a 375-nm laser. When the laser is injected into the optical fiber, the PETA becomes polymerized by a self-guiding effect, forming a polymer tip at the end of the fiber. The optimal conditions for obtaining a straight and mechanically stable p(PETA) tip are 1.0 μW laser injected power and 1.0 s exposure time. However, the polymerization of the p(PETA) chains within the optimal tip are incomplete during this rapid fabrication, resulting in an unstable dynamic resonant frequency of the tip. Therefore, we proposed to post-polymerize the tip by exposing it to a 365-nm UV lamp for at least 3 h. The final tip exhibits a stable dynamic characteristic, which is applicable for further sensing applications.

We then have demonstrated the p(PETA) tip as an effective FPI-based sensor for the detection of humidity in the air. The fiber-core/p(PETA) and p(PETA)/environment interface can reflect the incident light, enabling the p(PETA) tip to function as a FPI with a clear maximum and minimum interferometric signal. The FPI signal of the tip is observed to be highly sensitive to humidity in the air. This is due to hydroxyl groups within the p(PETA) structure, which strongly absorb water molecules in the humid air and significantly swell the tip. The length and/or the refractive index of the tip are therefore changed, resulting in a wavelength shift in the FPI signal. Within the humidity range from 30 to 80 %, the tips exhibit a consistent sensitivity of 90 pm/%RH, regardless of the tip length. This value is equivalent to a relative sensitivity of 104 ppm/%RH, which is well in comparison with the results of other reported FPI humidity sensors. The sensing signal of the p(PETA) tip is highly stable and reproducible. In addition, cross effect of the temperature on the humidity sensing is negligible as the FPI signal is insensitive to variations of temperature. All of the results indicate that p(PETA) tips can be practically potential for humidity sensing devices.

Next, we have proposed a novel method for the detection of water content in hygroscopic liquids using water-saturated fiber optic p(PETA) tips. The experiments were carried out on glycerol-water mixtures and ethylene glycol-water mixtures as model tests. The p(PETA) tip was firstly dipped in water so that the p(PETA) chains can fully absorb the water and then dipped inside the glycerol or ethylene glycol solutions with at a specific water contaminated content. These steps are repeated for each time of detecting water in a

solution. The FPI of the tip inside the pure hygroscopic liquid is taken as the reference signal. Compared to this reference signal, the FPI signal of the p(PETA) tip inside the solution shifts towards longer wavelengths as the water contaminated content increases. The FPI shift follows a nonlinearly dependence on the water content changing from 0 to 100 wt.%, with a significant shift in the low water range and less shift in the higher water range. If water contamination is below 10 wt.%, the FPI shift is reasonably linear to the water content and we obtained a sensitivity of 394 pm/wt.% and 226 pm/wt.% for glycerol and ethylene glycol solutions, respectively. The shift in the FPI signal is due to the absorption of the water within the p(PETA) structure by the hygroscopic solutions, causing the length of the tip to vary. Besides a good sensitivity, the tip exhibits excellent repeatability and stability performance and the response signal is independent of the tip length. All the findings highlight the practical application of the fiber optic p(PETA) tips for sensing water in hygroscopic liquids.

Finally, we have developed a tip with a core of p(PETA) and a shell of molecularly imprinted polymers (MIPs) for the detection of Dansyl-L-phenylalanine. The p(PETA) tip was fabricated using the self-guiding polymerization but without a post-polymerization step. The remaining C=C bonds on its surface allow for the anchoring of photoiniferter CDTPA under green light irradiation. The surface attached CDTPA can then initiate a photo-polymerization of the MIP layer surrounding the p(PETA) tip in the subsequent step under blue light irradiation. Upon binding with Dansyl-L-phenylalanine which has an analogous structure with the template of MIPs, the refractive index of the MIP layer changes, leading to a change in the FPI signal of the whole p(PETA)/MIP tip. This result makes the p(PETA)/MIP potential for sensing Dansyl-L-phenylalanine in liquid media. The sensing is very selective as the FPI signal of the tip inside Z-D-Phe, D-enantiomer of the template, is unchanged. This affordable method offers novel possibilities for creating fiber optic FPI-based MIP sensors for the detection of different analytes with a high selectivity.

6.2. Perspectives

The fiber optic p(PETA) tip has proven as a potential sensor for humidity, water, and chemical analytes. Although the sensing performance is attractive, there are some drawbacks of the fiber optic FPI sensor based on p(PETA) tip. We highlight below these drawbacks and the

possible perspective solutions to improve the quality of the sensors and to bring them closer to real-world devices.

The major problem of the p(PETA) tip-based FPI sensor is the mechanical durability of the tip. Under strong mechanical impact, the p(PETA) tip can break and be removed from the optical fiber. The sensor tip must therefore be handled with great care. An analogue configuration can be proposed by developing a hemispherical p(PETA) film on the facet of the fiber. This can be done by polymerizing a PETA droplet attached to the fiber end. This configuration is much better than the tip in terms of mechanical durability. However, with a large lateral size of the p(PETA) hemisphere, the response time of this device is expected to be longer than that of the tip-based device.

For humidity sensing application, to achieve a better sensitivity, one can formulate polymer tips made of a UV-curable material which is more hydrophilic than p(PETA). Some possible materials can be NOA 63 (from Norland Optics), poly (hydroxyethyl acrylate) or UV-cured composite film of carbon nanotubes, acrylated epoxidized soybean oil, and poly (ethylene glycol) methyl ether acrylate.

For the water sensing application, it is necessary to carry out a detailed study on the sensitivity of the p(PETA) tip for different hygroscopic liquids. This work would allow one to deduce a correlation between the sensitivity of the sensor and the hydrophilicity of the testing liquid. The sensitivity of the p(PETA) tip is expected to be higher for the liquid which is more hydrophilic.

For FPI-based MIPs sensor, it is still a high demand for creating a MIPs tip directly on the facet of the fiber. This process, if successful, will be more straightforward than the p(PETA)/MIP core/shell tip presented in this thesis. To achieve a MIP tip, the MIPs precursor solution should have a high viscosity, so that the photo-polymerized MIP chains can be better attached to the fiber facet. The formulation also needs to be conducted in a free-oxygen environment, ensuring a proper polymerization of MIP.

The experiments in this thesis employ single mode optical fibers (SMF) Thorlabs 780HP working at wavelengths ranging from 780 to 970 nm. Other used optical components also function within this wavelength range. That makes the experimental setup for recording the FPI sensor signal more affordable for our team. However, telecommunication single-mode

fibers working in a wavelength range from 1300 to 1500 nm are more commonly used in practice due to their extremely low attenuation. We therefore propose to conduct further study on PETA-based FPI sensors using this telecommunication SMF. This study also needs an expensive optical spectrum analyzer with a high resolution in the pm scale.

Last but not least, there is a great need to build an experimental setup with a specific mechanical design that allows simultaneous formulation of multiple fiber optic FPI-based polymer tips.